# INFORMATION TO USERS

This manuscript has been reproduced from the microfilm master. UMI films the text directly from the original or copy submitted. Thus, some thesis and dissertation copies are in typewriter face, while others may be from any type of computer printer.

**The quality of this reproduction is dependent upon the quality of the copy submitted.** Broken or indistinct print, colored or poor quality illustrations and photographs, print bleedthrough, substandard margins, and improper alignment can adversely affect reproduction.

In the unlikely event that the author did not send UMI a complete manuscript and there are missing pages, these will be noted. Also, if unauthorized copyright material had to be removed, a note will indicate the deletion.

Oversize materials (e.g., maps, drawings, charts) are reproduced by sectioning the original, beginning at the upper left-hand corner and continuing from left to right in equal sections with small overlaps. Each original is also photographed in one exposure and is included in reduced form at the back of the book.

Photographs included in the original manuscript have been reproduced xerographically in this copy. Higher quality 6" x 9" black and white photographic prints are available for any photographs or illustrations appearing in this copy for an additional charge. Contact UMI directly to order.

U·M·I

University Microfilms International
A Bell & Howell Information Company
300 North Zeeb Road, Ann Arbor, MI 48106-1346 USA
313/761-4700 800/521-0600

Order Number 9405508

# Analysis and reduced simulations of laminar/turbulent wake flows

Cao, Nian-Zheng, Ph.D.

City University of New York, 1993

U·M·I
300 N. Zeeb Rd.
Ann Arbor, MI 48106

# ANALYSIS AND REDUCED SIMULATIONS OF LAMINAR/TURBULENT WAKE FLOWS

by

NIAN-ZHENG CAO

A dissertation submitted to the Graduate Faculty in
Engineering in partial fulfillment of the
requirements for the degree of Doctor of Philosophy,
The City University of New York

1993

This manuscript has been read and accepted by the Graduate Faculty in Engineering in satisfaction of the dissertation requirement for the degree of Doctor of Philosophy.

9/27/93
Date

Nadine Aubry
Chair of Examining Committee

9/27/93
Date

Gerard L. Cohen
Executive Officer

Professor Andreas Acrivos
Professor Yiannis Andreopoulos
Professor Nadine Aubry
Professor George Karniadakis
Professor George Triantafyllou
Supervisory Committee

The City University of New York

# Abstract

## ANALYSIS AND REDUCED SIMULATIONS OF LAMINAR/TURBULENT WAKE FLOWS

by

Nian-Zheng Cao

Advisor: Professor Nadine Aubry

Laminar and turbulent wakes behind bluff bodies are simulated by reduced systems and analyzed through Biorthogonal and Proper Orthogonal Decomposition techniques.

First, a reduced direct numerical simulation is proposed to integrate the Navier-Stokes equations and simulate laminar wake flows, using a spectral expansion based on basis functions satisfying the boundary conditions. More specifically, by removing the body from the computational domain and imposing the spatial mean velocity profile, we derive a reduced representation which successfully reproduces a stable two-dimensional vortex street at Reynolds number $Re = 56$ (based on the diameter of the cylinder and the speed of the fluid at infinity) and its three-dimensional secondary instability at Reynolds number $Re = 230$. These results are similar to those obtained at a significantly higher computational effort by direct numerical simulations of the original system including the cylinder.

Second, the spatio-temporal structure of laminar and turbulent wake flows is investigated through a biorthogonal decomposition analysis, particularly in terms of spatio-temporal symmetries. We show for example how the spatio-temporal translation symmetry characterizing traveling waves is broken in a two-dimensional wake

flow behind a half-cylinder. As far as turbulence is concerned, if the flow is assumed to satisfy the scaling invariance of the Navier-Stokes equations, then biorthogonal energy spectra should decay exponentially fast. This is indeed observed in the analysis of experimental data in a turbulent wake. We then construct a low-dimensional dynamical system for a laminar wake flow past a half cylinder based on the biorthogonal decomposition. The efficiency of the truncation in the biorthogonal decomposition technique is demonstrated by a successful numerical reproduction of the Karman vortex street.

Third, the structure of a turbulent far-wake behind a circular cylinder (at a downstream distance of 100 cylinder diameters) experimentally measured by Guezennec and Gieseke (1991) is studied via the proper orthogonal decomposition, assuming the homogeneity of the flow in the spanwise and streamwise directions. We show that the first proper orthogonal mode presents the main features of typical coherent patterns which have been discovered by other researchers, including the double-roller structure and spanwise/ streamwise vortices. Finally, a low-dimensional dynamical system based on the first proper orthogonal modes and derived from the Navier-Stokes equations predicts turbulence statistics of approximately the right shape.

To my family.

# Acknowledgements

I am deeply grateful to my mentor Professor Nadine Aubry for her guidance and support. I would never have been able to accomplish this work without her assistance, stimulation and trust. The encouragements of Professor Andreas Acrivos, the director of the Levich Institute where this research was performed, as well as those of Professor Sheldon Weinbaum, gave me the strength to stay in research and overcome all kinds of difficulties. I would also like to thank Dr. Ricardo Lima, Professor George Triantafyllou, Professor George Karniadakis and Professor Yiannis Andreopoulos who offered insightful comments and suggestions.

I am especially indebted to my wife, Yu Zeng, for her understanding patience, constant enthusiastic support and contributions in all aspects.

Finally, I want to thank Mary and Tammy for the wonderful working conditions and assistance they provided. I am also grateful to my friends Anurag, Bir, Dimas, Fan, Fernando, Jana, Jeff, Kai, Lian, Nikolaos, Pawel, Said, Sanjeev and Wang for the nice time (and a lot of fun) we had together.

This work was supported by a grant from the U.S. Office of Naval Research, Fluid Dynamics Program (Code 1132F).

# Contents

**List of Figures** ix

**1 Introduction** 1
- 1.1 Numerical Simulation of Laminar Wake Flows . . . . . 3
- 1.2 Spatio-temporal Analysis of Wake flows . . . . . 7
- 1.3 Turbulent Structures in the Wake behind a Circular Cylinder . . . . . 10

**2 Numerical Simulation of a Laminar Wake Flow via a Reduced System** 15
- 2.1 Numerical Method . . . . . 16
- 2.2 Shear Layer Flow . . . . . 21
- 2.3 Two-Dimensional Wake Flow . . . . . 26
- 2.4 Three-Dimensional Wake Flow . . . . . 33
- 2.5 The Karman Street as a Solution of Forced Navier-Stokes Equations in Simple Geometry . . . . . 39
  - 2.5.1 Formulation of the Reduced System with External Forcing . . 40
  - 2.5.2 The External Forcing Term . . . . . 41
  - 2.5.3 Numerical Results and Discussions . . . . . 43
- 2.6 Conclusions . . . . . 44

**3 Spatio-temporal Analysis of Wake flows** 53
- 3.1 A Tool for Space-time Analysis: Biorthogonal Decompositions . . . . 54
- 3.2 Some Space-time Symmetries in Wake Flows . . . . . 56
  - 3.2.1 Translation Symmetries . . . . . 58
  - 3.2.2 Statistical Reflection Symmetry . . . . . 59
  - 3.2.3 Instantaneous Reflection Symmetry . . . . . 66
  - 3.2.4 Space-time $Z_2$ Symmetry . . . . . 66
- 3.3 Appearance of Spatio-temporal Symmetries through the Primary Instability . . . . . 68
- 3.4 Breaking of the Previous Space-time Symmetries: A First Step Toward 'Complexity' . . . . . 69
- 3.5 Space-time Symmetries of Turbulent Wake Flows . . . . . 79

3.5.1 Dilation Symmetries of the Navier-Stokes Equations and Biorthogonal Decomposition . . . . . 79
3.5.2 Analysis for Turbulent Wake Flow behind a Circular Cylinder 82
3.6 A Low Dimensional Dynamical System . . . . . 93
3.6.1 The Derivation of Ordinary Differential Equations . . . . . 94
3.6.2 Numerical Results . . . . . 96
3.7 Conclusions . . . . . 98

**4 Turbulent Wake Flow Studied by the Proper Orthogonal Decomposition Method 102**
4.1 Flow System and Experimental Measurements . . . . . 103
4.2 The Proper Orthogonal Decomposition . . . . . 104
4.3 Energy Spectrum and Large Eddy Structure . . . . . 106
4.4 Low-dimensional Dynamical System . . . . . 115
4.4.1 Mean Velocity Model . . . . . 115
4.4.2 Derivation of the Sets of ODEs . . . . . 117
4.4.3 Numerical Results and Discussion . . . . . 119
4.5 Conclusions . . . . . 125

**5 Summary and Discussion 126**

**A Coefficient Matrices $G_{\pm}$, $G_{11}$ and $G_{22}$ 129**

**B The Ordinary Differential Equations of the Dynamical System For Turbulent Wake Flows 131**

**Bibliography 133**

# List of Figures


1.1 The sketch of the flow past a half cylinder. . . . . 8
1.2 Double-roller structure from Grant (1956). . . . . 12
1.3 Double-roller structure from Payne and Lumley (1967). . . . . 12

2.1 Result from a computation of the shear layer flow. Time evolution of the energy $E_{10}$ for a two-dimensional disturbance with $A_{11} = 0$ and $A_{10} = 0.01, 0.125$. The Reynolds number is $Re = 400$, the wavenumber $\alpha_1 = 0.4$, and the resolution $8 \times 32 \times 1$. The solid lines represent the results from our computation. The dashed lines show the growth rate from the linear instability analysis. . . . . 22
2.2 Result from our computation of the shear layer flow. Instantaneous spanwise vorticity contour at times (a) $t = 8$ (Contour interval is 0.07) and (b) $t = 32$ (Contour interval is 0.06) at Reynolds number $Re = 83$ for a two-dimensional disturbance defined by $A_{11} = 0$, $A_{10} = 0.2$. Peak contour value is (a) $-1.05$, (b) $-0.96$. . . . . 23
2.3 Result from our computation of the shear layer flow. Three-dimensional iso-surface of the sum of the absolute values of all three vorticity components $|\omega_1| + |\omega_2| + |\omega_3|$ at Reynolds number $Re = 56$ for a resolution of $32 \times 32 \times 32$, for a three-dimensional disturbance defined by $A_{11} = 0.003$, $A_{10} = 0.22$ and $\alpha_1(\phi - \theta) = \pi/2$. . . . . 25
2.4 Time history of the velocity at the spatial location $x_1 = 1.125, x_2 = 0$ at Reynolds number $Re = 56$ from a two-dimensional simulation of the reduced system A for wake flow: a) $x_1$-component; b) $x_2$-component. 27
2.5 Instantaneous iso-vorticity contour lines at Reynolds number $Re = 56$ from a two-dimensional simulation of the reduced system A for wake flow. . . . . 29
2.6 Time evolution of the velocity at $x_1 = 1.125, x_2 = 0$ at $Re = 230$ from a two-dimensional simulation of the reduced system A for wake flow: a) $x_1$-component; b) $x_2$-component. . . . . 30
2.7 Instantaneous iso-vorticity contours at Reynolds number $Re = 230$ from a two-dimensional simulation of the reduced system A for wake flow. . . . . 31

2.8 Time evolution of the velocity at $x_1 = 1.125, x_2 = 0$ at $Re = 230$ from a two-dimensional simulation of the reduced system for wake flow with $32 \times 32$ modes: a) $x_1$-component; b) $x_2$-component. . . . . 32
2.9 Time evolution of the velocity at the location $x_1 = 1.125$, $x_2 = 0.098$, $x_3 = 0$ at Reynolds number $Re = 175$ from a three-dimensional simulation of the reduced system A for wake flow, showing that the three-dimensional perturbation vanishes: a) $x_1$-component; b) $x_2$-component; c) $x_3$-component. . . . . 35
2.10 Time evolution of the velocity at the location $x_1 = 1.125$, $x_2 = 0.089$, $x_3 = 0$ at Reynolds number $Re = 230$ from a three-dimensional simulation of the reduced system A for wake flow, showing a three-dimensional periodic flow: a) $x_1$- component; b) $x_2$-component; c) $x_3$-component. . . . . 36
2.11 Temporal mean velocity distribution $U_t$ versus $x_3$ at $x_2 = 0.098$ from the three-dimensional simulation of the reduced system A for wake flow at Reynolds number $Re = 230$. . . . . 37
2.12 Three-dimensional view of an iso-surface of the sum of all three vorticity components $|\omega_1| + |\omega_2| + |\omega_3|$ at $Re = 230$ from a three-dimensional simulation of the reduced system A for wake flow. . . . . 38
2.13 Wake flow simulation via the reduced system B. Time series of the velocity at the location $x_1 = 1.35$ on the centerline ($x_2 = 0$) numerically obtained by integrating our reduced system (2.38) and (2.39) at Reynolds number ($Re = 56$, with a zero forcing term, i.e. $\mathbf{F} = 0.$): a) the streamwise velocity component $u_1$, b) the normal velocity component $u_2$. . . . . 45
2.14 Wake flow simulation via the reduced system B. Time series of the velocity at the location $x_1 = 1.35$ on the centerline ($x_2 = 0$) numerically obtained by integrating our reduced system (2.38) and (2.39) at Reynolds number $Re = 56$, with the linear forcing term (2.45): a) the streamwise velocity component $u_1$, b) the normal velocity component $u_2$. . . . . 46
2.15 Wake flow simulation via the reduced system B. Iso-vorticity contours of the same flow as in Figure 2.14. . . . . 47
2.16 Wake flow simulation via the reduced system B. Comparison between the temporal mean velocity profile of the same flow as in Figure 2.14 (solid line) and the basic flow, namely the experimentally obtained (temporal) mean velocity (dashed line). . . . . 48
2.17 Wake flow simulation via the reduced system B. Time series of the velocity at the location $x_1 = 1.35$ on the centerline ($x_2 = 0$) numerically obtained by integrating our reduced system (2.38) and (2.39) at Reynolds number $Re = 56$, with the nonlinear forcing term (2.44): a) the streamwise velocity component $u_1$, b) the normal velocity component $u_2$. . . . . 49

2.18 Wake flow simulation via the reduced system B. Iso-vorticity contours of the same flow as in Figure 2.17. . . . . 50
2.19 Wake flow simulation via the reduced system B. Comparison between the temporal mean velocity profile of the same flow as in Figure 2.17 (solid line) and the basic flow, namely the experimentally obtained (temporal) mean velocity (dashed line), showing the superposition of the two curves. . . . . 51

3.1 BOD analysis of numerical data of a flow past a half cylinder. Normalized energy spectrum $p_n = \lambda_n / \sum_k \lambda_k$ with $\lambda_n = A_n^2$. (a) $Re = 100$; (b) $Re = 200$. . . . . 70
3.2 BOD analysis of numerical data of a flow past a half cylinder. The $x_1$-component of the topo $\phi_1^{(n)}$ (n appears below the corresponding curve) at $x_2 = 1.0$ as a function of $x_1$, $Re = 100$. . . . . 71
3.3 BOD analysis of numerical data of a flow past a half cylinder. Chrono $\psi^{(n)}$(t) at Reynolds number $Re = 100$. (a) $n = 1$; (b) $n = 2, 3$; (c) $n = 4, 5$; (d) $n = 6, 7$. . . . . 72
3.4 BOD analysis of numerical data of a flow past a half cylinder. The $x_1$-component of the topo $\phi_1^{(n)}$ at $x_1 = 7.0$ as a function of normal position $x_2$ at Reynolds number $Re = 100$. . . . . 73
3.5 BOD analysis of numerical data of a flow past a half cylinder. The $x_2$-component of the topo $\phi_2^{(n)}$ at $x_1 = 7.0$ as a function of normal position $x_2$ at Reynolds number $Re = 100$. . . . . 74
3.6 BOD analysis of numerical data of a flow past a half cylinder. Chrono $\psi^{(n)}$(t) at $Re = 200$: (a) $n = 1$; (b) $n = 2, 3$; (c) $n = 4, 5$; (d) $n = 6, 7$. 76
3.7 BOD analysis of numerical data of a flow past a half cylinder. The $x_1$-component of topo $\phi_1^{(n)}$ at the normal location $x_2 = 1.0$ as a function of streamwise variable $x_1$, Reynolds number is $Re = 200$. . . . . 77
3.8 BOD analysis of numerical data of a flow past a half cylinder. The $x_1$-component of the velocity as a function of $x_1$ at Reynolds number $Re = 200$. Horizontal axis is $x_1$, different curves represent the velocity at successive times, time increases from bottom to top. . . . . 78
3.9 POD analysis of the experimental data in a turbulent far wake flow. Energy spectrum $\ln \lambda^{(lkn)}$ as a function of the POD index $n$ at a fixed Fourier wavenumber $(l, k)$. . . . . 83
3.10 POD analysis of the experimental data in a turbulent far wake flow. One-dimensional spectrum $\lambda^{(n)}$ on a logarithmic scale versus the mode index $n$. . . . . 85
3.11 POD analysis of the experimental data in a turbulent far wake flow. Spectrum $\lambda^{(n)}$ of a series of self-similar modes $(n_l = 3, 6, 10, 13)$. . . . 87
3.12 POD analysis of the experimental data in a turbulent far wake flow. Series of self-similar modes $\phi_i^{(n_l)}$, $- \; i = 1$, $- \cdot - \; i = 2$, $- \cdot \cdot - \; i = 3$ $(n_l = 3, 6, 10, 13)$ whose spectrum is displayed in Figure 3.11. . . . . 88

3.13 POD analysis of the experimental data in a turbulent far wake flow. Spectrum $\lambda^{(n)}$ of a series of self-similar modes ($n_l = 4, 8, 14$). . . . . 89
3.14 POD analysis of the experimental data in a turbulent far wake flow. Series of self-similar modes $\phi_i^{(n_l)}$, $-$ $i = 1$, $-\cdot-$ $i = 2$, $-\cdot\cdot-$ $i = 3$ ($n_l = 4, 8, 14$) whose spectrum is displayed in Figure 3.13. . . . . 90
3.15 POD analysis of the experimental data in a turbulent far wake flow. Spectrum $\lambda^{(n)}$ of a series of self-similar modes ($n_l = 1, 7, 12$). . . . . 91
3.16 POD analysis of the experimental data in a turbulent far wake flow. Series of self-similar modes $\phi_i^{(n_l)}$, $-$ $i = 1$, $-\cdot-$ $i = 2$, $-\cdot\cdot-$ $i = 3$ ($n_l = 1, 7, 12$) whose spectrum is displayed in Figure 3.15. . . . . 92
3.17 Computation of the flow past a half-cylinder. Temporal eigenfunctions $\psi_n(t)$ versus $t$ obtained from the low dimensional dynamical system. Bottom: solid line $n = 1$; $-\cdot-$ $n = 2$; $-\cdot\cdot-$ $n = 3$. Top: solid line $n = 4$; $-\cdot-$ $n = 5$. . . . . 97
3.18 Computation of the flow past a half-cylinder. Same as in Figure 3.17, except that the influence of $c_j(t)$ is suppressed. . . . . 99
3.19 Computation of the flow past a half-cylinder. Same as in Figure 3.17, except that a constant first chrono $\psi_1(t) = constant$ is imposed. . . . 100

4.1 POD analysis of experimental data of a far-wake turbulent flow. The cumulated energy percentage $e_n$ as a function of POD index $n$ after summation over all Fourier modes . . . . . 107
4.2 POD analysis of experimental data of a far-wake turbulent flow. Reynolds stresses as functions of normal distance $x_2$ (for zero separation) reconstructed from the POD truncated expansion into the first $N$ POD modes (including all Fourier modes). Solid line: with all POD modes; $-\cdot-$ : $N = 3$; $-\cdot\cdot-$ : $N = 2$; $-\cdot\cdot\cdot-$ : $N = 1$. (a) $R_{12}$; (b) $R_{11}$; (c) $R_{22}$ ; (d) $R_{33}$. . . . . 108
4.3 POD analysis of experimental data of a far-wake turbulent flow. Streamline pattern of mode (1,1,1). . . . . 110
4.4 POD analysis of experimental data of a far-wake turbulent flow. Streamline pattern of mode (1,1,2). . . . . 111
4.5 POD analysis of experimental data of a far-wake turbulent flow. Streamline pattern of mode (1,0,1). . . . . 112
4.6 POD analysis of experimental data of a far-wake turbulent flow. Streamline pattern of mode (1,0,3). . . . . 113
4.7 Integration of a low dimensional dynamical system simulating a turbulent far-wake. Time series of selected time dependent coefficients $a^{(lkn)}(t)$, with specific values of $(l, k, n)$ appearing on the left-hand side of each curve. . . . . 120
4.8 Integration of a low dimensional dynamical system simulating a turbulent far-wake. Time series of the norm of the vorticity at the location $x = y = 3.6d$, $z = 0$, where $d$ is the diameter of the cylinder. . . . . 122

4.9 Integration of a low dimensional dynamical system simulating a turbulent far-wake. Reynolds stresses as functions of normal distance $x_2$: (a) $R_{12}$; (b) $R_{11}$; (c) $R_{22}$ ; (d) $R_{33}$. The solid line and dash line represent respectively those computed from the low-dimensional dynamical system and those reconstructed directly from the POD eigenfunctions and eigenvalues with the same truncation of modes. . . . . 123
4.10 Integration of a low dimensional dynamical system simulating a turbulent far-wake. Three-dimensional representation of an iso-surface of the norm of the vorticity. . . . . 124

# Chapter 1

# Introduction

Wakes behind bluff bodies furnish classical and important examples of flows having numerous geophysical and industrial applications. Their theoretical significance in fluid dynamics has been revealed by the understanding of the Karman street formation and the persistence of coherent structures at higher Reynolds numbers. Still nowadays, wake flows play a central role in fluid mechanics research.

Much work has been performed in the last twenty years to study the mechanisms controlling the wake formation and the near-wake evolution behind bluff bodies. Recent theoretical work has shown that the primary instability from a steady flow to a large-scale periodic motion is due to an absolute instability mechanism. From this viewpoint, it is very different from other flows with large-scale motions such as boundary and mixing layers which are convectively unstable. In wake flows, the importance of the formation of large-scale motions manifests itself, for instance, through the strong feed back the flow has on the body itself, resulting in a large amplitude unsteady lift and drag acting on the body with a possible strong aeroelastic or hydroelastic coupling. Furthermore, the large scale motions also create a strong noise field both directly and through the elastic coupling with the body. Therefore, it is very important to control the wake formation and the roll-up into an organized vor-

tex structure to reduce both steady and unsteady forces on the body and decrease or alter the noise signature.

Bluff body wakes provide many basic flow phenomena whose fundamental mechanisms are still not clearly understood, partially due to the lack of detailed analyses and measurements, the difficulty lying in the complexity of the system beyond low Reynolds numbers at which the flow is two-dimensional and periodic in space and time. Although it is formally possible to numerically solve the Navier-Stokes equations, it is difficult in practice due to the large computer memory and time units required for a reliable integration. When the flow becomes turbulent, the situation is even worse, involving an enormous amount of information carried by the fluctuating field evolving in both space and time: a complete numerical description of the flow is still not available, so that the following questions still remain open issues. What is the detailed structure of the large-scale motions? What is the structure of small scales? Is it possible to describe a wake flow by a reduced system? These questions have obviously important implications for understanding the mechanisms and controlling wake flows.

This thesis is an attempt to answer these questions, from different approaches, as we outline below.

## 1.1 Numerical Simulation of Laminar Wake Flows

Numerical simulations which play an important role in predicting and analyzing laminar, transitional and turbulent flows, are still limited to simple flow geometries and relatively low Reynolds numbers. Although numerical schemes differ from one another in their detailed procedure, they all involve a discretization process in which infinite dimensional (continuum) models are projected onto finite dimensional, discrete forms. The minimal number of degrees of freedom required in flow computations increases with both Reynolds number and the complexity of the flow geometry and depends on the particular discrete modes used. Efforts to adapt the modes to the spatial geometry and the dynamics of the flow have been made (Aubry et al., 1988, Sanghi and Aubry, 1992, Cao and Aubry, 1992, Deane et al., 1991). Significant progress in numerical simulations of turbulence should be possible by using renormalized well-adapted basis functions, as given by the scaling symmetry of the Navier-Stokes equations (Aubry et al., 1992(a), Lian and Aubry, 1993) and investigated in turbulent wake flows (Aubry and Cao, 1993, Cao and Aubry, 1992). The present approach, valid for statistically steady flows, concentrates on reducing the order of the system by replacing the complex geometry of the flow by a simple one (consisting of periodic boundary conditions) in which the spatial mean velocity is imposed and maintained time independent. The information concerning the latter is assumed to be known from experimental measurements, for instance. The question is then whether such a reduced representation can reproduce the fundamental dynamics of the original system, such as the primary and secondary instabilities. We test our ideas on a wake flow behind a cylinder where such a method has an obvious practical advantage. Indeed, the presence of the body generates a thin boundary layer near its surface which requires high resolution in full numerical simulations. It is also of high theoretical interest to compare the original system with the reduced one and investigate the role of the mean flow/fluctuation interaction. The idea of removing

the object in wake flows is not novel and can be found in Abernathy and Kronauer (1962) who simulated the instability of two parallel spatially periodic vortex sheets and obtained a vortex street whose spatial and temporal periodicities are different from that experimentally observed. More recently, Triantafyllou and Karniadakis (1990) simulated a vortex street of the right frequency by initially imposing an inflow equal to the temporal average flow taken at a location where it is the most linearly unstable. Although both studies reproduce a stable Karman street, they do not address the development of the three-dimensional secondary instability as Reynolds number increases.

The basic numerical techniques used to simulate fluid flow behavior can be classified into four categories: finite differences, finite elements, boundary elements and spectral methods. In fundamental investigations of laminar, transitional and turbulent flows in simple geometries, spectral methods (Gottlieb and Orszag 1977) have been mostly used, due to their high accuracy and efficiency. Since the development of spectral Galerkin methods by Orszag (1969) and Eliasen et al. (1970), many useful and efficient versions of this kind of methods have emerged. The basic concept is as follows: Looking for solutions of a partial differential equation, we expand the dependent variable into a truncated series of spatial orthogonal basis functions and convert the partial differential equation into a set of ordinary differential equations via a Galerkin procedure. Different types of basis functions have been proposed such as Fourier modes, Chebyshev and Legendre polynomials, etc., depending on the flow boundary conditions. Periodic boundary conditions lead to Fourier series expansions which are accurate and efficient. For finite domains with physical boundary conditions such as no-slip, polynomial basis functions are usually used (Rogallo and Moin 1984). In case of infinite domains, domain transformations have been used to recover finite situations. Metcalfe et al. (1987) used algebraic and exponential mappings to simulate the mixing layer flow with Fourier expansions in two periodic directions and

Chebyshev polynomials in the infinite direction. Spalart et al. (1991) designed a spectral method for both a half-infinite domain and a full infinite domain combining an exponential mapping with a Chebyshev polynomial expansion. Here, we propose a Fourier series expansion in the infinite normal direction in terms of a tangent function mapping, so that the quiescent boundary conditions are satisfied a priori. In the two other directions classical periodic boundary conditions are applied, allowing the use of Fourier modes. Consequently, the computation can be performed with accuracy and efficiency due to Fourier expansions satisfying all boundary conditions.

The vortex wake of a two-dimensional circular cylinder has been extensively investigated both computationally and experimentally. At small Reynolds numbers, the flow is steady, two-dimensional and invariant under reflection about the center plane. As Reynolds number increases above 40, a Hopf bifurcation to a laminar, two-dimensional periodic state of a Karman street occurs. This primary instability, observed in a number of experimental investigations and reproduced by numerical simulations (Gresho et al., 1984, Karniadakis et al., 1985 and Braza et al., 1986), has been theoretically explained by the linear stability theory by Triantafyllou et al. (1986). While experiments clearly show that transition to turbulence occurs at a Reynolds number between 200 and 400, two-dimensional numerical simulations still predict laminar flows for Reynolds numbers as high as 500 (Karniadakis and Triantafyllou, 1989). The details of this transition, whose computation is CPU time consuming, need further investigations, in contrast to the primary instability now well-understood. Recently, the three-dimensional direct numerical simulation of Karniadakis and Triantafyllou (1992), a mixed spectral and spectral element method, performed on a Cray-Y/PM, used a mesh of 34 elements in the transverse plane and 16 Fourier modes in the spanwise direction. It shows that a secondary instability to a three-dimensional periodic solution occurs when Reynolds number reaches 200, followed by a period doubling bifurcation at about $Re = 333$ leading to a turbulent

flow as the Reynolds number is increased further.

We present in Chapter 2 a numerical simulation of a wake flow by a spectral method (see also Cao and Aubry 1993). Instead of considering no-slip boundary conditions on the surface of the body (here, a cylinder), we remove the latter from the computational domain and decompose the flow into the fluctuation and the spatial mean. We then impose the latter and maintain it constant as time evolves. This permits the application of simple boundary conditions for the fluctuation, which are periodic in the spanwise and streamwise directions and quiescent otherwise. We then use a Fourier mode expansion in all directions, making the code particularly efficient. We show that our method can reproduce a Karman street and we compare our results with those obtained experimentally (Kovasznay, 1949) and by instability theory (Triantafyllou et al., 1986). As the Reynolds number increases, the secondary instability to a three-dimensional state is obtained, as in the numerical simulation of the original problem by Karniadakis and Triantafyllou (1992).

It is interesting to note that the reduced systems derived in the works mentioned above are shear flows characterized by simple (usually rectangular) geometries and a main shear velocity profile. However, we have to keep in mind that although periodic boundary conditions in the streamwise direction are the simplest computationally, they constrain the flow to be parallel, in which case the latter tends to a uniform state under the action of the viscous dissipation, which is, of course, an unrealistic asymptotic state. In order to keep the periodicity of the flow, we then have to compensate this (artificial) effect. The most natural way for achieving this goal seems to either maintain the spatial mean shear velocity profile independent of time, thus feeding continuously the perturbation and preventing the uniform state to settle, or impose a forcing compensating viscous diffusion. We then apply the latter idea to a wake flow behind a circular cylinder to obtain another reduced numerical simulation, and find satisfying results.

## 1.2 Spatio-temporal Analysis of Wake flows

Biorthogonal decomposition (BOD) methods proposed by Aubry et al. (1991, 1992(b)) have the advantage of offering a space-time dynamical system theory tool which convergences optimally fast in a space-time sense. They also define a framework in which spatio-temporal symmetries can be introduced in a natural manner. More precisely, they consist in decomposing a space-time function $u(x,t)$ into spatial orthogonal modes and temporal orthogonal modes, the two sets of modes being related by an isomorphism (a one-to-one correspondence). Spatio-temporal bifurcations and chaos in one-dimensional systems such as numerically obtained solutions of the Kuramoto-Sivashinsky equations and experimentally measured dispersive chaos in binary-fluid convection (Aubry and Lian, 1993, Slimani et al., 1992) have been quantitatively investigated using such tools.

The derivation of a low-dimensional dynamical system using the appropriate modes is an attractive approach to fluid mechanics since it has the potential of describing complex physical phenomena in a low-dimensional space, which would require a huge number of degrees of freedom, particularly at high Reynolds number, by conventional approaches such as direct numerical simulations. As we will discuss in the following section, a few low-dimensional dynamical systems have been proposed to analyze different flow problems. In particular for laminar wake flows, Deane et al. (1991) applied the POD method in two-dimensions to obtain a low-dimensional dynamical system by prescribing the mean velocity of the flow. They neglected the influence of the pressure term, supposing that their computational domain was large enough to assume zero pressure at the outflow boundary and periodic conditions in the cross-flow direction. Although decomposing the flow into a mean and a fluctuation (via a Reynolds decomposition) and treating the mean flow separately has been proven to be a successful method (Aubry et al. 1988, Cao and Aubry 1992), it is not necessarily the most efficient approach in case of an inhomogeneous flow (Aubry,

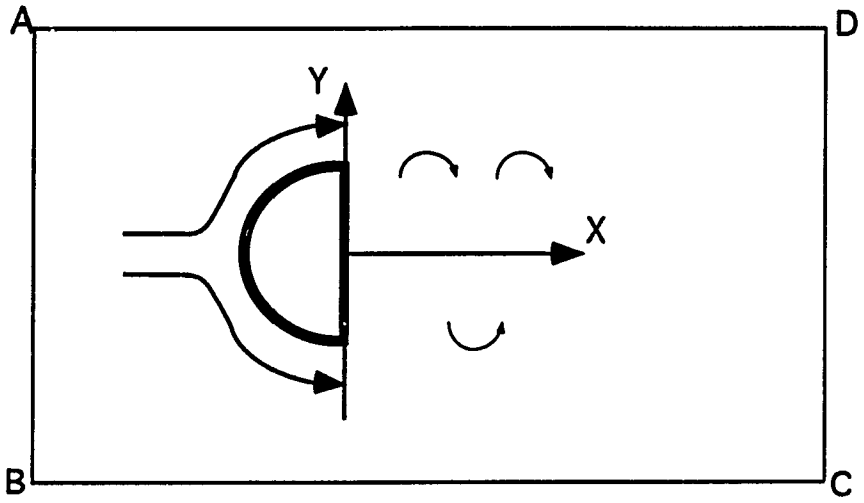


Figure 1.1: The sketch of the flow past a half cylinder.

1991, Aubry et al., 1991). For this reason, in the following, we do not extract the mean velocity from the flow systematically and therefore, we release any constraint concerning the mean flow.

In Chapter 3, attempts are made to analyze the spatio-temporal symmetries of wake flows. First, we consider the laminar wake flow behind a half-cylinder sketched in Figure 1.1. Flow patterns developing behind a full cylinder at different Reynolds numbers have been investigated in computational and experimental studies. We recall that at small Reynolds numbers, the flow is steady, two-dimensional and symmetric about the center plane. When the Reynolds number increases above 40, a Hopf bifurcation to a two-dimensional laminar periodic state of a Karman street takes place. This vortex pattern persists until the Reynolds number reaches 200-400, when the flow becomes three-dimensional. However, by confining the flow to a two-dimensional state in a two-dimensional computation, the periodic Karman street is found to persist (Karniadakis and Triantafyllou, 1989). Although the transitions to three-dimensionality and turbulence are correctly predicted by the three-

dimensional direct numerical simulation (Karniadakis and Triantafyllou, 1992), the two-dimensional numerical simulation reveals very different characteristics for a half-cylinder wake flow. Karniadakis and Tomboulides (1992(a)) found that such a wake flow undergoes a period doubling bifurcation associated with a vortex merging process. Although this finding was robust to a finer resolution, it disappeared when three-dimensionality effects were accounted for in the calculation. Moreover, period doubling could not be experimentally identified by Brown (1992). Although such a phenomenon may be a mere two-dimensional artifact in this particular flow, it remains a robust and generic feature of the transition process in other flows such as mixing layers. For this reason, we feel that the nature of the merging process is worth investigating, particularly its impact on the spatio-temporal structure of the flow. It is certainly a possible mechanism through which the flow becomes more complex in space and time, as we show below. We should, however, keep in mind that it is certainly *one* scenario for the route to turbulence, but it is not the only one.

We concentrate our spatio-temporal study of wake flows on the breaking and creation of space-time symmetries, as the main features of various instabilities through the transition process. For low Reynolds numbers, we show that classical spatial symmetries, such as the streamwise translation and the reflection about the mid-plane, are present statistically, or equivalently in a space-time sense. In these simple cases, the configuration of the temporal component of the symmetry is easy to determine. As Reynolds number increases, particular spatio-temporal symmetries break while the statistical symmetry is maintained. The latter is responsible, as we prove in this thesis, for the spatial structure of the flow in terms of sinuous and varicose modes. At high Reynolds numbers, in the turbulence regime, it is likely that the flow satisfies the space-time scaling symmetry of the Navier-Stokes equations. Our findings concerning turbulent wake flows tend to indicate that this is indeed the case. This has important consequences on the spectrum decay law and the spatio-temporal

structure of the flow.

Based on the BOD expansion, we derive a low-dimensional dynamical system at low Reynolds number which reproduces the Karman street. It is found that without prescribing the mean velocity it is necessary to include the pressure term to keep the amplitude of the oscillation from decaying to zero.

## 1.3 Turbulent Structures in the Wake behind a Circular Cylinder

The identification of coherent structures in turbulent flows has attracted a great deal of attention among turbulence researchers. It is found that despite their randomness, most turbulent flows reveal certain types of organized, large scale motions. Progress in the observation of these large structures has been achieved both experimentally and computationally in various flows such as boundary layers, mixing layers and wakes. However, researchers seem to have recently concentrated their efforts in the study of the boundary layer and the mixing layer, wake flows being more neglected, perhaps because a direct numerical simulation of a turbulent wake has not yet been performed due to its relative complex geometry.

Coherent, large eddy structures in fully developed wake flows have been detected experimentally since Grant (1958), who first suggested the existence of the double-roller structure (see Figure 1.2) and that of spanwise vortices from the observation of the correlations. Later, Payne and Lumley (1967) applying the proper orthogonal decomposition technique to analyze the correlations measured by Grant(1958), obtained a "conceptual picture" of the double-roller structure shown in Figure 1.3. While there is some similarities between Grant's structures and those of Payne and Lumley, the main difference lies in their orientation (see Figures 1.2 and 1.3). In Payne and Lumey's sketch, the roller axes are almost perpendicular to the wake

centerplane, while the flow circulation is inclined to the $(x, z)$-plane (except at the center-plane). In Grant's sketch, the roller axes are inclined to the $(x, z)$-plane, while the flow circulation is in the $(x, z)$ plane. Grant notices that such eddies cannot gain energy through stretching by the mean shear and concludes that these eddies have probably been formed in the near-wake region and should be decaying in time. We note that the same is valid for Payne and Lumley's eddies. Later, double-roller eddy structures and spanwise vortices were observed in the far-wake region by Keffer (1965), Townsend (1979) and Mumford (1983). Bisset et al. (1990) supported Grant's suggestion, confirming that the roller axis in the far-wake is aligned in the principal direction of the mean strain by analyzing the probability density distribution function of the inclination of the vorticity vector. Ferré and Giralt (1989) also identified the double-roller structure in the far-wake through a pattern-recognition analysis. In spite of these discoveries, the theoretical and experimental investigations concerning the large eddy structures in turbulent wake flows are far from being complete. Clearly, there is a need for a better understanding of their configuration (e.g. the orientation of their axis and their plane of circulation) and their (decaying or self-sustained) dynamics.

In the near-wake region, experimentalists have concentrated their efforts on measurements in spanwise or normal cross-sections. Conditional averaging methods have been used to study the topology of the structures by Cantwell and Coles (1983), Perry et al. (1982) and Hayakawa and Hussain (1989). They all conclude that large-scale motions in the near-wake mostly consist of Karman street like vortices (Ferré and Giralt 1989). While the investigation of coherent structures in the near-wake is interesting by itself, it has also the potential of providing explanations for the formation of coherent structures and the origin of far-wake flow patterns.

Coherent structures in turbulent shear flows were first visualized by Kline et al. (1967) in a turbulent boundary layer and by Brown and Roshko (1974) in a

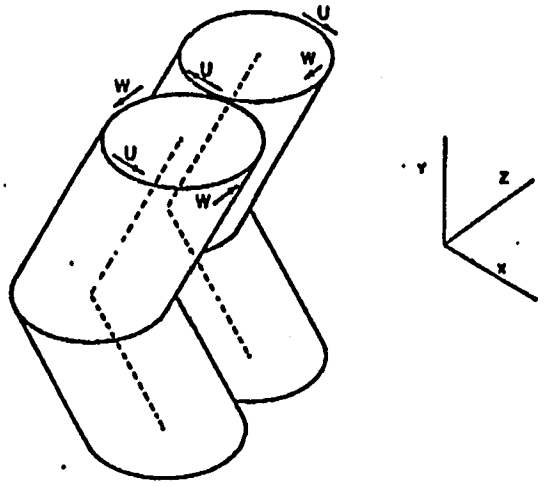


Figure 1.2: Double-roller structure from Grant (1956).

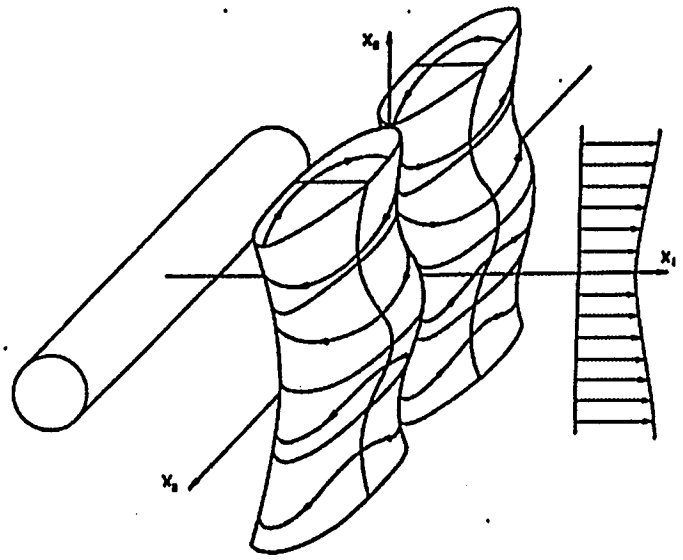


Figure 1.3: Double-roller structure from Payne and Lumley (1967).

turbulent mixing layer. Conditional averaging methods then became the main tool for identifying coherent structures from experimental data. The variable interval time average (VITA) was perhaps the most popular one, used by Blackwelder and Kaplan (1976) and Chen and Blackwelder (1978) for analyzing both the velocity and the temperature in turbulent boundary layer flows. The VITA technique is successful in separating random fluctuations from coherent motions by averaging the signal in terms of an indicator function, a priori chosen, sensitive to the occurrence of a coherent motion. Unfortunately, the VITA technique cannot serve as a general detection tool for organized motions in turbulence because the success of the detection relies upon an energy criteria which may differ from one type of organized pattern to another one. The proper orthogonal decomposition (POD) method, proposed by Lumley (1965) to extract coherent structures from turbulent flows, has proven to be an efficient and objective method in studying boundary layer flows (Bakewell and Lumley 1988, Herzog, 1986), jet flows (Glauser at el. 1990) and wake flows (Payne and Lumley 1967). The POD consists in decomposing the two-point correlation of a random, say spatial, function into a set of deterministic spatial orthogonal eigenfunctions. The original signal can then be expanded in terms of these eigenfunctions, with a priori unknown random coefficients. Despite the efficiency of such a technique, one of the main difficulties of the method is due to the loss of the phase information. The expansion converges optimally fast in quadratic mean (i.e. in terms of the kinetic energy). A review of the application of the POD to turbulence can be found in Sirovich (1987), Aubry (1991) and Berkooz et al. (1993).

From a theoretical viewpoint, advances in dynamical systems theory suggest that it may be possible to describe turbulence through the strange attractor concept, although the connection is not yet clear, the latter concerning low-dimensional dynamical systems in contrast with the high-dimensional, extremely complex turbulence process (Guckenheimer, 1986). Since the early discovery by Lorenz (1963) of the presence

of a strange attractor in a three-dimensional dynamical system, a severely truncated model of the Boussinesq equations, low-dimensional dynamical models of turbulence have been derived for closed flow systems such as Reyleigh-Bénard and Taylor-Couette flows (Rand and Young (1981), Swinney and Gollub (1981) and Campbell and Rose (1983)). More recently, attempts to describe open flow systems such as boundary layers and jet flows have been made by Aubry et al. (1988), Glauser et al. (1990) and Sanghi and Aubry (1992). In these works, the technique is similar and was first developed by Aubry et al. (1988). It consists in projecting the Navier-Stokes equations onto a low dimensional space spanned by the first POD eigenfunctions, modeling the action of small scales by an eddy-viscosity model.

In Chapter 4, we investigate the presence of coherent structures in a turbulent wake behind a circular cylinder. We then derive a low dimensional dynamical system to study the dynamics of these structures. The results of the integration are exploited and compared with experimental results. To achieve this goal, we first decompose the two-point correlation tensor experimentally measured by Guezennec and Gieseke (1991) via the POD. The spatial resolution of these correlations is much higher than those of Grant used by Payne and Lumley (1967). Moreover, our definition of coherent structures is different from that used by the latter authors, allowing us to visualize, in the first eigenmode, a relatively complex pattern consisting of both the double-roller structure and spanwise vortices. Contrarily to previous authors' findings, our double-roller can sustain itself, which is indeed confirmed by the low-dimensional dynamical system results. The latter is derived in a similar way as that of Aubry et al. (1988), with, however, a different mean velocity profile representation. The form of the turbulent Reynolds stresses is successfully recovered through this low dimensional dynamical system, but their amplitudes are too low (as expected).

# Chapter 2

# Numerical Simulation of a Laminar Wake Flow via a Reduced System

In this chapter, we propose reduced numerical simulations for integrating the Navier-Stokes equations and simulating the laminar wake flows. By removing the body from the computational domain and imposing the spatial mean velocity profile, we derive a reduced system which is then solved by a spectral expansion based on basis functions satisfying specific boundary conditions and reproduces successfully the dynamics of laminar wake flows.

The whole chapter is divided into three parts. In the first section, we formulate the problem and describe the numerical method used. In the second section, we test our numerical method and code by solving mixing layer flows. In the third, fourth and fifth sections, we present the numerical results obtained, namely the Karman street and its three-dimensional secondary instability. The conclusions are given in the sixth section.

## 2.1 Numerical Method

The incompressible Navier-Stokes equations are solved in the form

$$\frac{\partial \mathbf{v}}{\partial t} = \mathbf{v} \times \omega - \nabla \Pi + \nu \nabla^2 \mathbf{v} \tag{2.1}$$

$$\nabla \cdot \mathbf{v} = 0 \tag{2.2}$$

where $\omega = \nabla \times \mathbf{v}$ is the vorticity, $\Pi = p + \frac{1}{2}|\mathbf{v}|^2$ is the pressure head and $\mathbf{v}$ is decomposed into the spatial (i.e. streamwise and spanwise) mean and the fluctuation:

$$\mathbf{v} = \mathbf{U} + \mathbf{u} \tag{2.3}$$

where $\mathbf{U}$ is supposed to be known and time independent. We define the Strouhal number $St = fd/U_\infty$ and the Reynolds number $Re = U_\infty d/\nu$, where $d$ is the diameter of the cylinder, $U_\infty$ the free stream velocity at infinity, $\nu$ the kinematic viscosity and $f$ the frequency of the oscillations when a (temporally) periodic solution is obtained.

Periodic boundary conditions are applied in the streamwise ( x or $x_1$) and spanwise (z or $x_3$) directions for the fluctuation, i.e.

$$\mathbf{u}(x_1 + \frac{2\pi}{\alpha_1}, x_2, x_3, t) = \mathbf{u}(x_1, x_2, x_3, t) \tag{2.4}$$

$$\mathbf{u}(x_1, x_2, x_3 + \frac{2\pi}{\alpha_3}, t) = \mathbf{u}(x_1, x_2, x_3, t) \tag{2.5}$$

where $\alpha_1$ and $\alpha_3$ are the smallest streamwise and spanwise wavenumbers. The fluctuating flow can be assumed to be quiescent as $x_2 \to \pm\infty$, namely

$$\lim_{x_2 \to \pm\infty} \mathbf{u} = 0 \tag{2.6}$$

In the $x_2$- or y-direction, the infinite domain is transformed into a finite one through a coordinate transformation $x_2 = Y(\eta)$ as in Metcalfe et al. (1987) and Cain and Ferziger (1984). However, the specific form of $Y(\eta)$ we use, different from theirs, is

$$x_2 = L \tan \eta \quad (|x_2| < \infty, |\eta| < \pi/2), \tag{2.7}$$

so that $|\eta|$ tends to $\pi/2$ as $|x_2|$ becomes infinite. After the coordinate transformation, the mesh of the domain is non-uniformly distributed in the $x_2$-direction, leading to a high resolution at low $x_2$-values, namely near the center-plane where non-uniformities of the flow are concentrated.

We use a spectral method with Fourier modes to solve equations (2.1),(2.2) and (2.3) subject to the boundary conditions (2.4), (2.5) and (2.6). The time integration is performed by a fractional-step method similar to that used by Kim and Moin (1985). The time advance of the momentum equations is performed by an implicit second-order Crank-Nicholson scheme for the viscous terms and by an explicit second-order Adams-Bashforth technique for the advection terms. The fractional-step method is used to decouple the momentum and continuity equations, the fraction procedure consisting of two steps. In the first one, all terms except the pressure term are used to calculate an intermediate velocity field $\mathbf{v}^*$; in the second one, the pressure gradient term alone is considered to determine a corrected velocity field satisfying the continuity equation. The temporally discretized equations are

$$\frac{v_j^* - v_j^n}{\Delta t} = \frac{3}{2}h_j^n - \frac{1}{2}h_j^{n-1} + \frac{1}{2Re}(\nabla^2 v_j^* + \nabla^2 v_j^n) \tag{2.8}$$

$$\frac{v_j^{n+1} - v_j^*}{\Delta t} = -\frac{\partial \varphi^{n+1}}{\partial x_j} \tag{2.9}$$

$$\nabla^2 \varphi^{n+1} = \frac{1}{\Delta t}\frac{\partial u_j^*}{\partial x_j} \tag{2.10}$$

where

$$\mathbf{h} = \mathbf{v} \times \omega. \tag{2.11}$$

We recall that $\mathbf{v} = \mathbf{U} + \mathbf{u}$, $\mathbf{U}$ denoting the (imposed) average spatial velocity and $\mathbf{u}$ the fluctuation. The pressure $p$ can be obtained from the intermediate function $\varphi$ from the following equation

$$p^{n+1} = \varphi^{n+1} + \frac{\Delta t}{2Re}\nabla^2 \varphi^{n+1}. \tag{2.12}$$

The spectral expansion based on Fourier modes in the streamwise and spanwise directions, consistent with the periodic boundary conditions (2.4) and (2.5), can be expressed as

$$f(x_1,x_2,x_3,t) = \sum_{|k_1|\le\frac{1}{2}N_1} \sum_{|k_3|\le\frac{1}{2}N_3} \hat{f}(k_1,x_2,k_3,t) \exp i(k_1\alpha_1 x_1 + k_3\alpha_3 x_3) \qquad (2.13)$$

where $f$ represents any physical quantity and $\hat{f}$ its Fourier Transform in the streamwise and spanwise directions.

The expansion in the $x_2$-direction, satisfying the zero boundary conditions at infinity, is proposed as follows:

$$\hat{f}(k_1,\eta,k_3,t) = \sum_{n=1}^{N_2} \hat{f}_-(n)\sin 2n\eta + \hat{f}_+(n)\cos(2n-1)\eta \qquad (2.14)$$

where "$_+$" (resp. "$_-$") thus characterizes the coefficients of even (resp. odd) modes in the variable $\eta$. We can write the spectral expansion in the matricial form

$$\begin{aligned} \hat{f} = \quad & (\sin 2\eta, \sin 4\eta, \ldots, \sin 2N_2\eta)\cdot \hat{\mathbf{f}}_-^T + \\ & (\cos\eta, \cos 3\eta, \ldots, \cos(2N_2-1)\eta)\cdot \hat{\mathbf{f}}_+^T \end{aligned} \qquad (2.15)$$

where

$$\hat{\mathbf{f}}_\pm = (\hat{f}_\pm(1), \hat{f}_\pm(2), \ldots \hat{f}_\pm(N_2)). \qquad (2.16)$$

$$\hat{f}_\pm(n) = \hat{f}_\pm(k_1,n,k_3,t) \quad \text{where } (n = 1,2,\ldots,N_2) \qquad (2.17)$$

The differentiation with respect to $x_2$ can then be written under the form

$$\begin{aligned} \frac{\partial \hat{f}}{\partial x_2} = \quad & (\sin 2\eta, \sin 4\eta, \ldots, \sin 2N_2\eta)\mathbf{G}_-\hat{\mathbf{f}}_-^{\mathbf{T}} + \\ & (\cos\eta, \cos 3\eta, \ldots, \cos(2N_2-1)\eta)\mathbf{G}_+\hat{\mathbf{f}}_+^{\mathbf{T}} \end{aligned} \qquad (2.18)$$

$$\begin{aligned} \frac{\partial^2 \hat{f}}{\partial x_2^2} = \quad & (\sin 2\eta, \sin 4\eta, \ldots, \sin 2N_2\eta, \\ & \cos\eta, \cos 3\eta, \ldots, \cos(2N_2-1)\eta)\mathbf{G}(\hat{\mathbf{f}}_-, \hat{\mathbf{f}}_+)^T \end{aligned} \qquad (2.19)$$

where $\mathbf{G}$ is a band matrix in the form of

$$\mathbf{G} = \begin{pmatrix} \mathbf{G_{11}} & 0 \\ 0 & \mathbf{G_{22}} \end{pmatrix} \tag{2.20}$$

$\mathbf{G_{\pm}}$, $\mathbf{G_{11}}$ and $\mathbf{G_{22}}$, which are all band coefficient matrices independent of time, will be given in Appendix A.

Taking the spanwise and streamwise Fourier transform of equations (2.8), (2.9) and (2.10), we obtain

$$\Omega_2^2\hat{v}_j^* + (\Omega_1^2 + \Omega_3^2 - \frac{2Re}{\Delta t})\hat{v}_j^* = -\Omega_2^2\hat{v}_j^n - (\Omega_1^2 + \Omega_3^2 + \frac{2Re}{\Delta t})\hat{v}_j^n + Re(3\hat{h}_j^n - \hat{h}_j^{n-1}) \tag{2.21}$$

$$\Omega_2^2\hat{\varphi}^* + (\Omega_1^2 + \Omega_3^2)\hat{\varphi}^{n+1} = \frac{1}{\Delta t}(\Omega_2\hat{v}_2^* + \Omega_1\hat{v}_1^* + \Omega_3\hat{v}_3^*) \tag{2.22}$$

$$\hat{v}_j^{n+1} = \hat{v}_j^* - \Omega_j\hat{\varphi}^{n+1}\Delta t \tag{2.23}$$

where $\Omega_i$ is defined as

$$\Omega_i = \begin{cases} ik_j & \text{if } j = 1,3 \\ \dfrac{\partial}{\partial x_2} & \text{if } j = 2. \end{cases}$$

By substitution of the spectral expansions (2.15), (2.18) and (2.19) of the fluctuating velocity $\mathbf{u}$ and the intermediate function $\varphi$ (and their derivatives), we obtain the final discretized equations in spectral space in the following form

$$\mathbf{G}_v(\hat{\mathbf{v}}_{-j}^*, \hat{\mathbf{v}}_{+j}^*) = -\mathbf{G}_v(\hat{\mathbf{v}}_{-j}^n, \hat{\mathbf{v}}_{+j}^n) + \mathbf{b}_j^T \quad \text{for } j = 1,2,3 \tag{2.24}$$

$$\mathbf{G}_\varphi(\hat{\varphi}_-^{n+1}, \hat{\varphi}_+^{n+1})^T = \mathbf{c}^T \tag{2.25}$$

and

$$(\hat{\mathbf{v}}_{-i}^{n+1}, \hat{\mathbf{v}}_{+i}^{n+1})^T = (\hat{\mathbf{v}}_{-i}^*, \hat{\mathbf{v}}_{+i}^*)^T - \mathbf{d}_i^T \tag{2.26}$$

corresponding to (2.21), (2.22) and (2.23) accordingly, where

$$\mathbf{G}_v = \mathbf{G} - (\Omega_1^2 + \Omega_2^2 + 2\frac{Re}{\Delta t})\mathbf{I} \tag{2.27}$$

$$\mathbf{G}_\varphi = \mathbf{G} + 2\frac{Re}{\Delta t}\mathbf{I} \tag{2.28}$$

$$\mathbf{b}_j^T = -\frac{Re}{2}(3\hat{\mathbf{h}}_{-j}^n - \hat{\mathbf{h}}_{-j}^{n-1}, 3\hat{\mathbf{h}}_{+j}^n - \hat{\mathbf{h}}_{+j}^{n-1})^T - 4\frac{Re}{\Delta t}(\hat{\mathbf{v}}_{-j}^n, \hat{\mathbf{v}}_{+j}^n) \tag{2.29}$$

$$\mathbf{c}^T = \frac{1}{\Delta t}\begin{pmatrix} \mathbf{G}_1\hat{\mathbf{v}}_{+2}^{*T} + \Omega_1\hat{\mathbf{v}}_{-2}^{*T} + \Omega_3\hat{\mathbf{v}}_{-3}^{*T} \\ \mathbf{G}_2\hat{\mathbf{v}}_{-2}^{*T} + \Omega_1\hat{\mathbf{v}}_{+2}^{*T} + \Omega_3\hat{\mathbf{v}}_{+3}^{*T} \end{pmatrix} \tag{2.30}$$

$$\mathbf{d}^T = \begin{cases} -\Omega_1\Delta t(\hat{\boldsymbol{\varphi}}_-^{n+1}, \hat{\boldsymbol{\varphi}}_+^{n+1})^T & j = 1 \\ -\Omega_3\Delta t(\hat{\boldsymbol{\varphi}}_-^{n+1}, \hat{\boldsymbol{\varphi}}_+^{n+1})^T & j = 3 \\ -\Delta t(\hat{\boldsymbol{\varphi}}_+^{n+1}\mathbf{G}_+^T\,,\ \hat{\boldsymbol{\varphi}}_-^{n+1}\mathbf{G}_-^T)^T & j = 2. \end{cases} \tag{2.31}$$

in which $\mathbf{I}$ is a unit matrix.

Assuming that the velocity field at the $n-1$ and $n$ time levels are known, we summarize the solving procedure for the velocity at the $n+1$ time level as follows.

1. Compute the Fourier Transform of the nonlinear term $\mathbf{h}$ by using a "pseudo spectral" technique, i.e. first evaluate it at collocation points in physical space, then transform it into spectral space. Then obtain $\mathbf{b}^T$ for the left hand side of (2.24).

2. Solve $\hat{\mathbf{v}}_{\pm j}^*$ from (2.24).

3. Evaluate $\mathbf{c}^T$ for the left hand side of (2.25). Then solve $(\hat{\boldsymbol{\varphi}}_-^{n+1}, \hat{\boldsymbol{\varphi}}_+^{n+1})^T$ from (2.25).

4. Substitute the results found in the previous steps into (2.26) to compute $\hat{\mathbf{v}}_{\pm j}^{n+1}$.

We should mention that the computation performed for the inversion of the linear algebraic equations in the second and fourth steps is efficient and accurate since the coefficient matrices involved are band-matrices and time-independent.

In the next section, we test our code on the primary and secondary instabilities of a mixing layer (without the decomposition (2.3)) before concentrating on wake flow simulations.

## 2.2 Shear Layer Flow

In order to check the stability, accuracy and convergence of our numerical algorithm and code, we compute the instability of a temporally growing shear layer and compare our results with those of Metcalfe et al.'s (1987) direct numerical simulation. We choose this problem as a test example for its similarity to the wake problem which we propose to solve. For the temporal instability of a shear layer, periodicity in the streamwise direction can be assumed. Similarly to the wake flow, the shear layer is homogeneous in the spanwise direction, and spanwise periodicity seems to be a reasonable assumption. The temporal instability is thereby simulated by numerically integrating the Navier-Stokes equations. The velocity field can be decomposed as follows

$$\mathbf{v}(x_1, x_2, x_3, t) = U_0(x_2)\mathbf{e}_1 + \mathbf{u}(x_1, x_2, x_3, t) \tag{2.32}$$

where $U_0$ is the laminar mean flow profile assumed to be $U_0(x_2) = U_0 \tanh x_2/\delta_i$. Here $\delta_i$ is the initial mean vorticity thickness. The boundary condition for $\mathbf{u}$ is assumed to be $\mathbf{u} \to 0$ as $x_2 \to \pm\infty$, i.e. the disturbance is quiescent at infinity. We then use the numerical method proposed in the previous section (without imposing the mean flow) to find the time-dependent solution, starting with the following initial condition

$$\mathbf{v}(x_1, x_2, x_3, 0) = A_{10}\mathbf{u}_0(x_2)\cos\alpha_1(x_1 + \theta) + A_{11}\mathbf{u}_0(x_2)\cos\alpha_1(x_1 + \phi)\sin\alpha_3 x_3 \tag{2.33}$$

Time is non-dimensionalized by $U_0/\delta_i$ and the Reynolds number is defined by $Re = U_0\delta_i/\nu$.

The two-dimensional instability is simulated with $A_{11} = 0$. Without initially disturbing the subharmonic mode, pairing does not occur. As found by Metcalfe et al. (1987), in this case, the flow evolves toward a quasi-steady state. Figure 2.1 shows the time evolution of the energy of the two-dimensional disturbance, $E_{10}$, for different initial amplitudes $A_{10}$. The value of $\alpha_1$ is chosen to be 0.4446, which is the wavenumber corresponding to the largest growth rate determined by linear stability

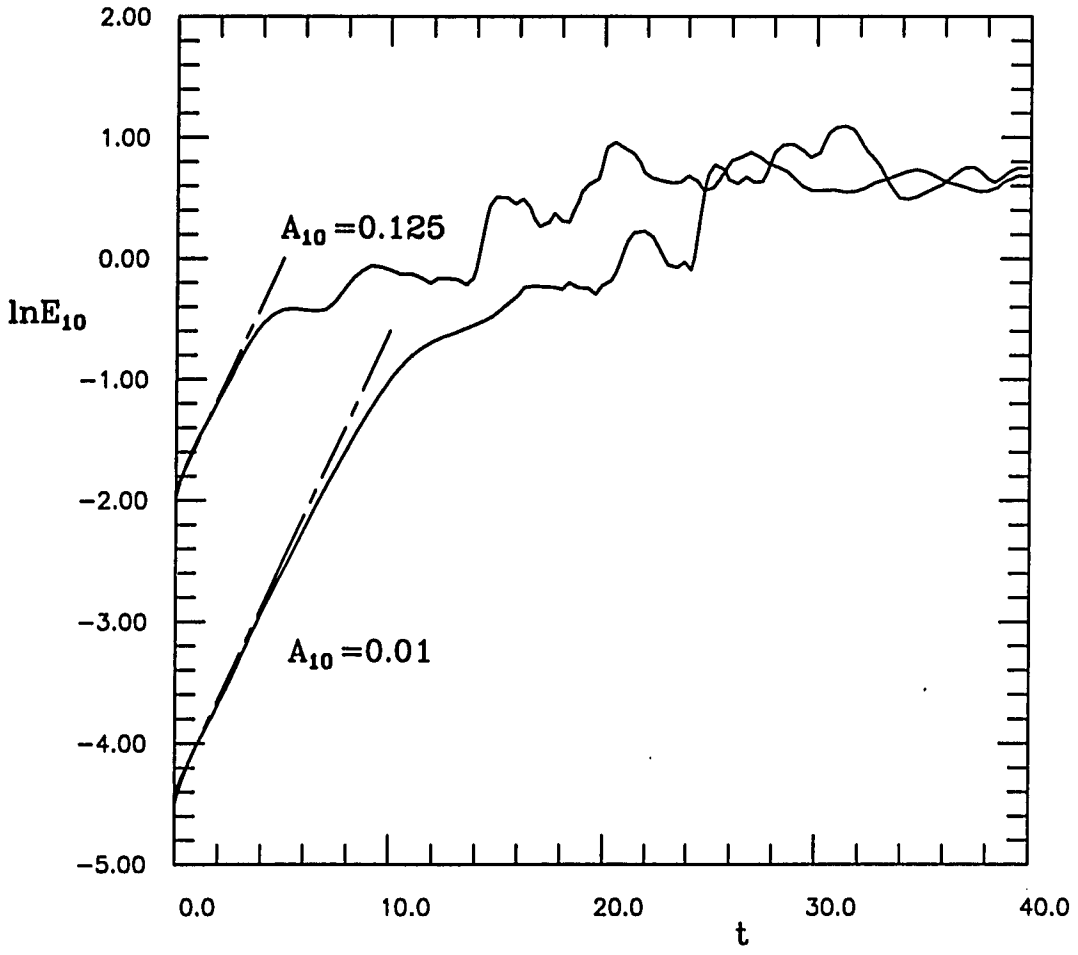


Figure 2.1: Result from a computation of the shear layer flow. Time evolution of the energy $E_{10}$ for a two-dimensional disturbance with $A_{11} = 0$ and $A_{10} = 0.01, 0.125$. The Reynolds number is $Re = 400$, the wavenumber $\alpha_1 = 0.4$, and the resolution $8 \times 32 \times 1$. The solid lines represent the results from our computation. The dashed lines show the growth rate from the linear instability analysis.

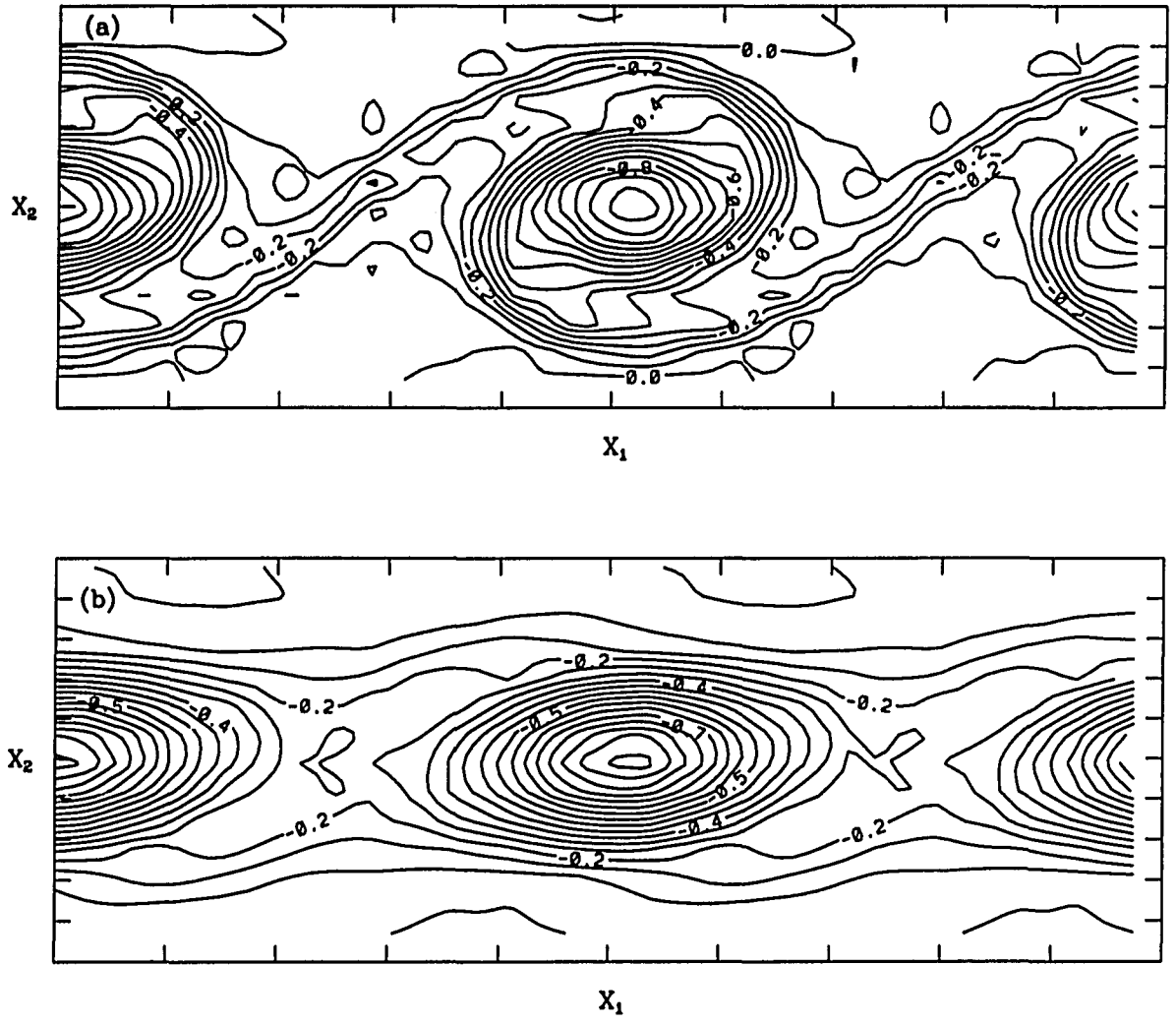


Figure 2.2: Result from our computation of the shear layer flow. Instantaneous spanwise vorticity contour at times (a) $t = 8$ (Contour interval is 0.07) and (b) $t = 32$ (Contour interval is 0.06) at Reynolds number $Re = 83$ for a two-dimensional disturbance defined by $A_{11} = 0$, $A_{10} = 0.2$. Peak contour value is (a) $-1.05$, (b) $-0.96$.

theory (Michalke, 1964). The energy $E_{10}$ is defined as

$$E_{10}(t) = \sum_{k_2=1}^{N_2} |\hat{u}_-(1,k_2,0,t)|^2 + |\hat{u}_+(1,k_2,0,t)|^2 \tag{2.34}$$

and the growth rate as

$$\sigma = \frac{dE_{10}/dt}{2E_{10}} \tag{2.35}$$

The wavenumber of the most unstable mode predicted by linear stability theory (Michalke 1964) is, by construction, our first non-zero streamwise wavenumber. Its growth rate has been theoretically determined: $\sigma = 0.19$. Figure 2.1 shows that our numerically obtained growth rate is approximately the same.

Figure 2.2 displays the instantaneous spanwise vorticity contours at two different times, from our calculation. It is consistent with Metcalfe et al.'s (1987) corresponding result (see their figure 2): in particular, we check that the maximal values are in very good agreement (Peak values are $-1.12$ at $t = 8$ and $-0.96$ at $t = 32$ in Matcalfe et al. (1987)).

At Reynolds number Re = 56, a three-dimensional instability takes place when the saturated two-dimensional flow is disturbed by a three-dimensional perturbation. We first compute the two-dimensional flow obtained from an initial disturbance with the amplitude $A_{10} = 0.22$ until saturation. Then, we superpose a three-dimensional disturbance of amplitude $A_{11} = 0.003$ to this two-dimensional state. Similarly to Metcalfe et al.'s (1987) finding, the flow consists of spanwise vorticity cores connected by smaller quasi-streamwise counter-rotating vortices, often called ribs, as shown in Figure 2.3. These streamwise rib-like structures have been observed experimentally by Breidenthal (1981) and Bernal (1981) and modeled by Lin and Corcos (1984).

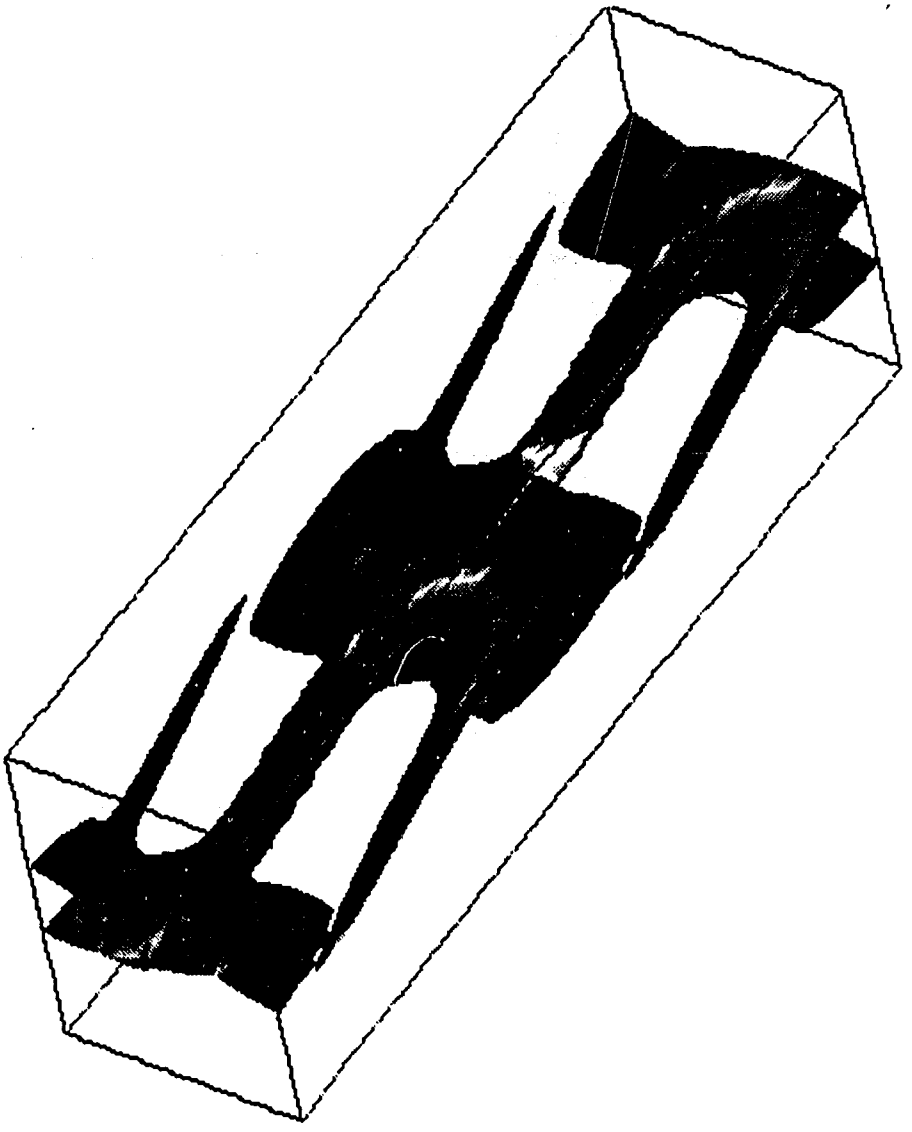

Figure 2.3: Result from our computation of the shear layer flow. Three-dimensional iso-surface of the sum of the absolute values of all three vorticity components $|\omega_1| + |\omega_2| + |\omega_3|$ at Reynolds number $Re = 56$ for a resolution of $32 \times 32 \times 32$, for a three-dimensional disturbance defined by $A_{11} = 0.003$, $A_{10} = 0.22$ and $\alpha_1(\phi - \theta) = \pi/2$.

## 2.3 Two-Dimensional Wake Flow

As we recall in the introduction, the wake flow behind a cylinder undergoes a Hopf bifurcation through which it loses its steadiness and becomes periodic in space and time. The resulting state is a traveling wave consisting of a vortex street (Karman Street) where the vorticity is spanwise only and the flow two-dimensional, depending strictly on $x$ and $y$. An important feature for our method to be valid is that the flow should reach a statistically steady state, more specifically the spatial (streamwise and spanwise) mean velocity profile should be time independent. Physically, this corresponds to a classical concept in turbulence: the mean flow continuously supplies energy to the fluctuation. Such an assumption is satisfied for statistically steady turbulent flows and traveling wave type flows. In the latter, the average in the direction of propagation (usually streamwise) can be replaced by the time average. Although wake flows decay downstream, the traveling wave approximation there is still accurate (except of course in the near-wake region), especially if one is interested in the instability processes and the local study of individual vortices. Our calculations include $16 \times 32$ normal and streamwise modes, although tests with $32 \times 32$ modes were also performed, leading to the same results. In the following, we refer to this reduced system as the reduced system A.

Our first numerical simulation of the wake flow behind a cylinder is performed at Reynolds number $Re = 56$. The mean velocity profile is taken as

$$U_0(x_2) = -A + A \tanh a(x_2^2 - b) \tag{2.36}$$

where A = 0.56, a = 1.60 and b = 0.50 (see Triantafyllou et al. (1986) who curve fitted Kovasnay's (1949) experimental data). Here we choose our lowest nonzero streamwise wavenumber to correspond to the most unstable mode predicted by Triantafyllou et al. (1986), namely $\alpha_1 = 4.33$, and restrict our computation to two dimensions, namely $\alpha_3 = 0$.

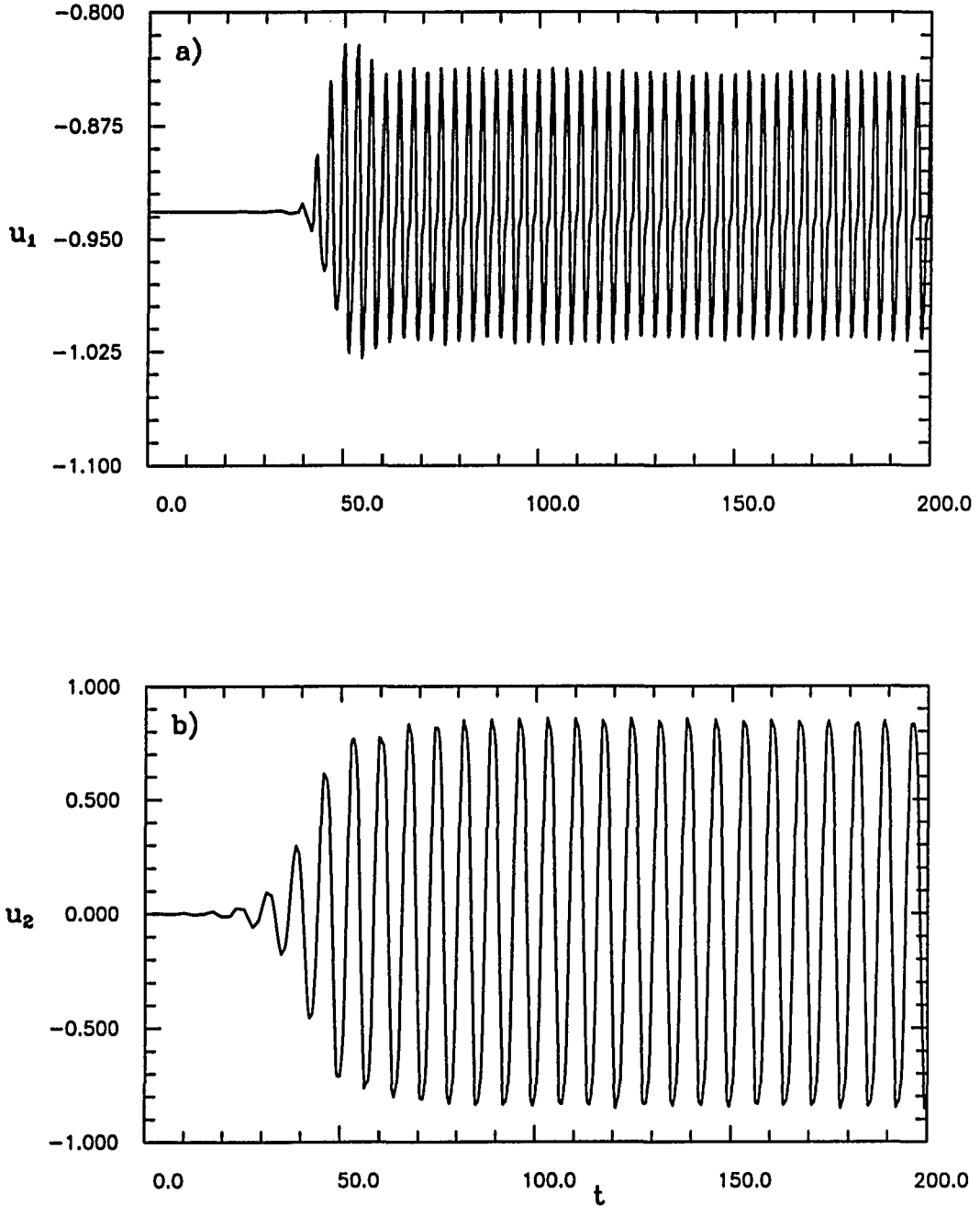


Figure 2.4: Time history of the velocity at the spatial location $x_1 = 1.125, x_2 = 0$ at Reynolds number $Re = 56$ from a two-dimensional simulation of the reduced system A for wake flow: a) $x_1$-component; b) $x_2$-component.

Figure 2.4 shows the time evolution of the two velocity components $u_1$ and $u_2$ at a specific $(x_1, x_2)$ location where we observe that the flow reaches a periodic state after a short transient. The Strouhal number computed is $St = 0.139$, which is in good agreement with the instability theory result (Triantafyllou et al., 1986) and Kovasznay's (1949) experimental finding ($St = 0.13$). The periodic flow consists of a vortex street traveling downstream. Figure 2.5 displays instantaneous iso-vorticity contours of the flow.

As in the direct numerical simulation of the original problem by Karniadakis and Triantafyllou (1989, 1992), in our reduced representation, we find that the two-dimensional periodic vortex street is a stable solution as Reynolds number is increased to $Re = 230$ and beyond. The (spatial) mean velocity we input here is that extracted from data obtained by three-dimensional direct numerical simulation of the full system (Karniadakis and Tomboulides, 1992(b)) at $Re = 333$, whose details will be discussed in the next section. As shown below by our three-dimensional computations, the exact form of the mean velocity profile, which can be taken at a slightly different Reynolds number since its Reynolds number dependence is slow (compared to that of the fluctuation), is not crucial here. The times series and structure of the Karman street thus obtained at Reynolds number $Re = 230$ is shown in Figures 2.6 and 2.7. Such obvious disagreements between computational and experimental studies (see the introduction) indicate that, as Reynolds number increases, three-dimensional effects develop and three-dimensional calculations, in the full system as in the reduced one, are unavoidable if one wants to reproduce both the Karman Street's instability and the route to turbulence. The resolution which has been used in the previous computation consists of $16 \times 32$ modes in the $x_1$-and $x_2$-directions. The solution thus obtained is very close to that computed with a finer mesh (using $32 \times 32$ modes), as shown in Figure 2.8.

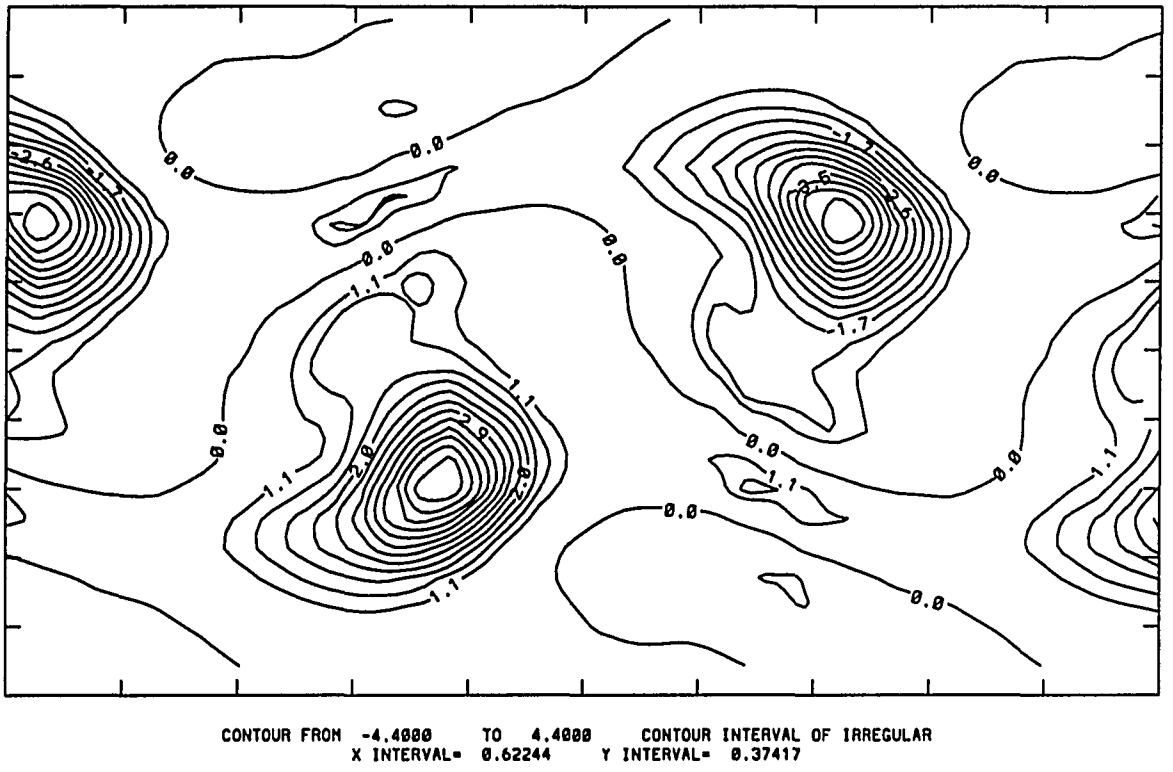


Figure 2.5: Instantaneous iso-vorticity contour lines at Reynolds number $Re = 56$ from a two-dimensional simulation of the reduced system A for wake flow.

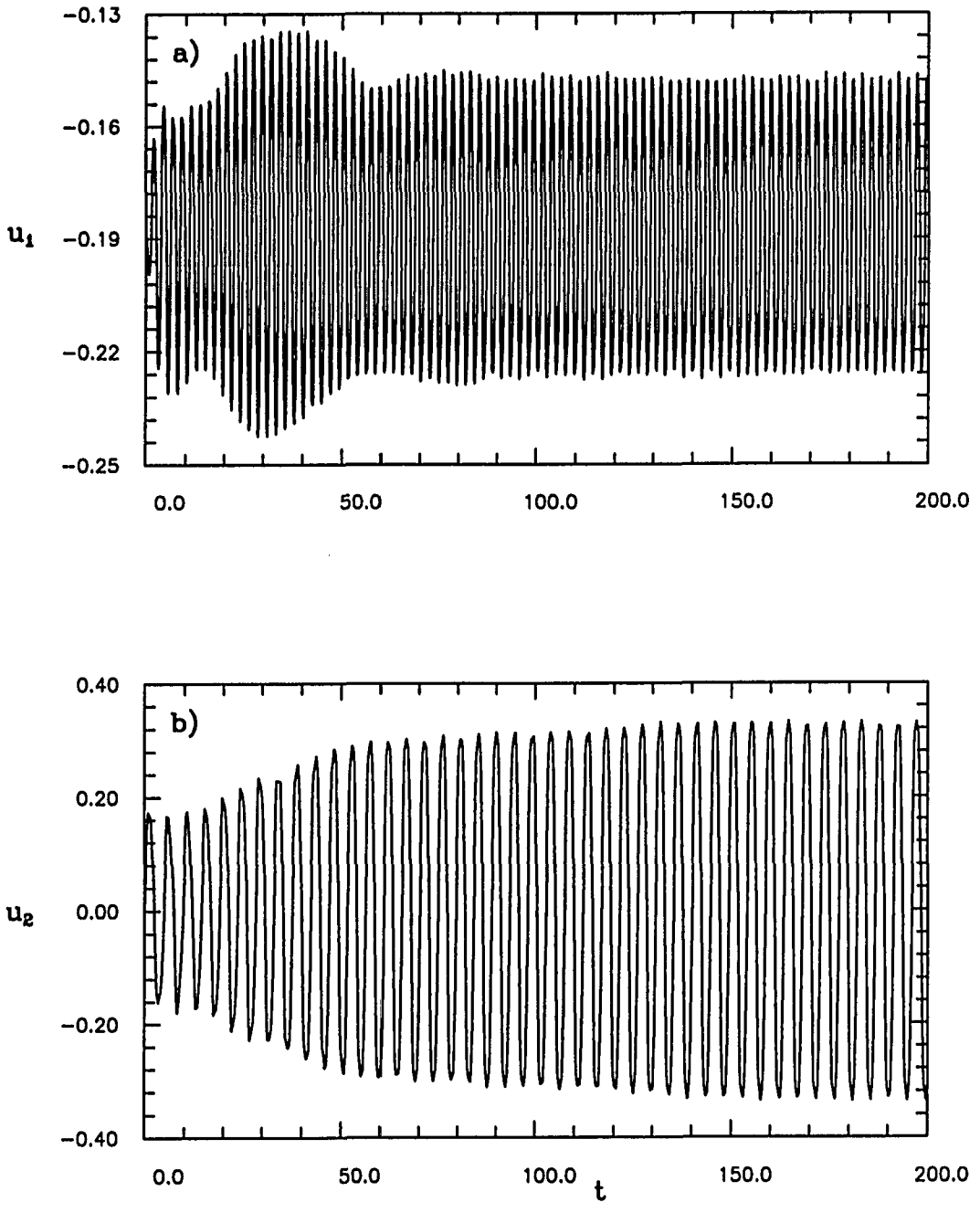


Figure 2.6: Time evolution of the velocity at $x_1 = 1.125, x_2 = 0$ at $Re = 230$ from a two-dimensional simulation of the reduced system A for wake flow: a) $x_1$-component; b) $x_2$-component.

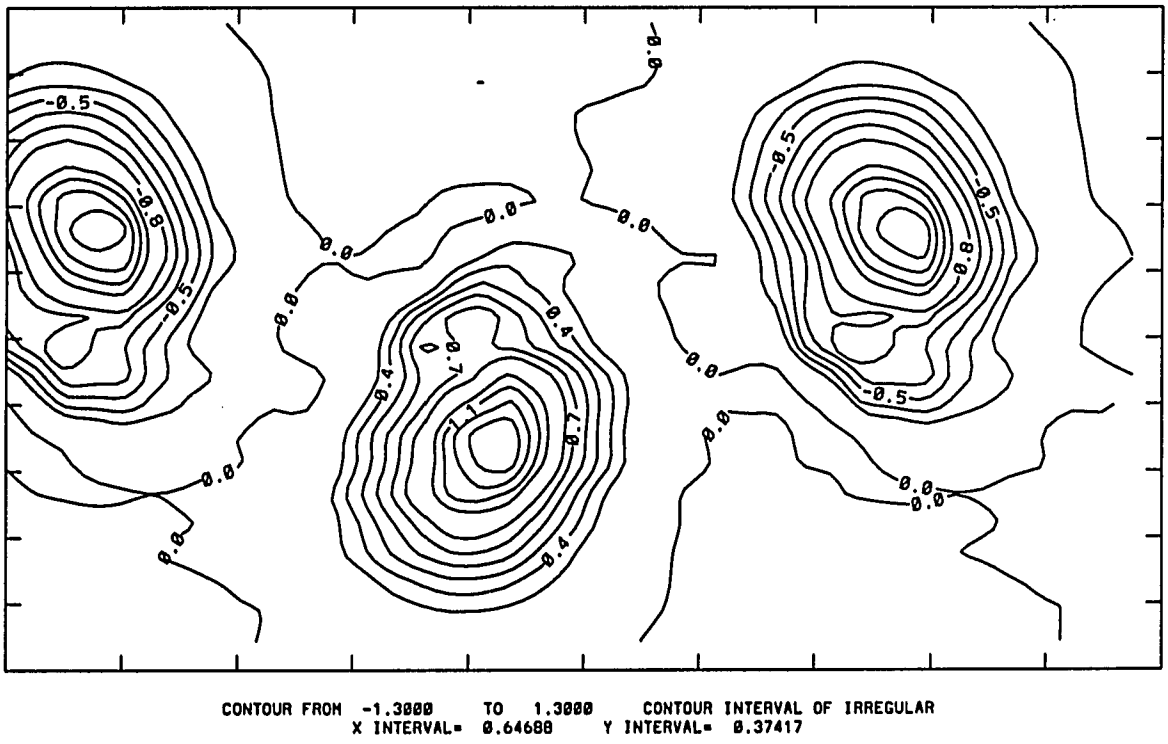


Figure 2.7: Instantaneous iso-vorticity contours at Reynolds number $Re = 230$ from a two-dimensional simulation of the reduced system A for wake flow.

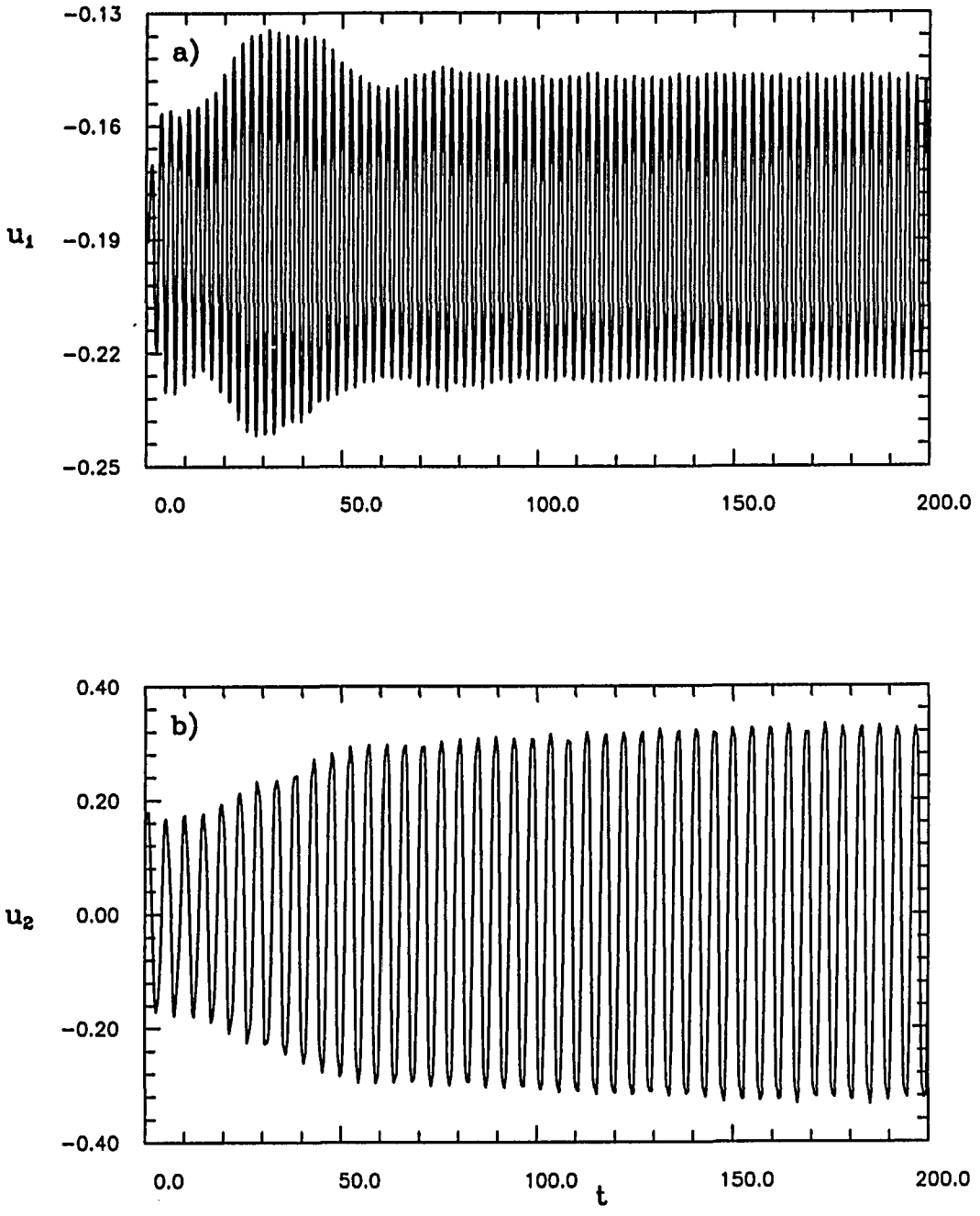


Figure 2.8: Time evolution of the velocity at $x_1 = 1.125, x_2 = 0$ at $Re = 230$ from a two-dimensional simulation of the reduced system for wake flow with $32 \times 32$ modes: a) $x_1$-component; b) $x_2$-component.

## 2.4 Three-Dimensional Wake Flow

While the parallel wake flow is more unstable to two-dimensional than to three-dimensional disturbances, the vortex street is subject to a three-dimensional secondary instability at a sufficiently high Reynolds number, as shown in experimental works (Williamson, 1988). In this section, we show that our reduced system A is capable of reproducing such an instability.

Again, assuming that the spatial mean of the flow is time independent, we impose it in our numerical simulation and maintain it constant as time evolves. Note that when the flow becomes three-dimensional, the temporal mean velocity profile depends on both $x_2$ and $x_3$ while the spatial mean, by definition, still depends on $x_2$ only. The latter can then be approximately identified with the zero Fourier component of the temporal mean. For example, Karniadakis and Triantafyllou (1992) approximate the temporal average velocity $U_t$ close to the secondary instability onset by

$$U_t(x_2, x_3) = U_0(x_2) + U_1(x_2)\cos\alpha_3 x_3, \tag{2.37}$$

so that we take the spatial mean velocity U to be $U_0$, which is equivalent to imposing only the first term in (2.37), the remaining part being computed. Note that this requires the spanwise length of our periodic box to be a multiple of $1/\alpha_3$. The specific profile of $U_0$ we use is extracted from data obtained by the direct numerical simulation of the original system at Reynolds number $Re = 333$ (Karniadakis and Tomboulides, 1992(b)). Due to the fact that this profile remains similar within the range of Reynolds numbers of interest here, we use it in our simulations of the reduced system for Reynolds numbers varying from 175 to 230. The number of Fourier modes used in our simulations is $16 \times 32 \times 16$ while tests including $32 \times 32 \times 32$ modes were also performed.

The three-dimensional instability of the flow is studied for various Reynolds numbers. For each run, we obtain the saturated two-dimensional periodic solution

to which we superpose a three-dimensional disturbance. The resulting flow is then taken as the initial condition of the three-dimensional calculation. At $Re = 175$, the three-dimensional disturbance vanishes after a short transient time making the two-dimensional flow stable again, as shown in Figure 2.9. As Reynolds number is increased to $Re = 230$, the three-dimensional disturbance grows, leading to a three-dimensional periodic flow displayed in Figure 2.10. These results suggest that there is a value of Reynolds number between 175 and 230 at which the flow bifurcates from a two-dimensional state to a three-dimensional one. The latter is compared to that obtained from a direct simulation of the full system.

Figure 2.11 shows the temporal mean velocity profile we obtain as a function of spanwise coordinate at Reynolds number $Re = 230$. Only one frequency is observed, indicating that (2.37) is indeed a good approximation. The particular wavenumber value is also identical to that obtained by direct numerical simulation of the full system (Karniadakis and Tomboulides, 1992(b)). Figure 2.12 shows a three-dimensional iso-surface of the sum of the absolute value of all three vorticity components, revealing the spanwise modulation of a vortex pair.

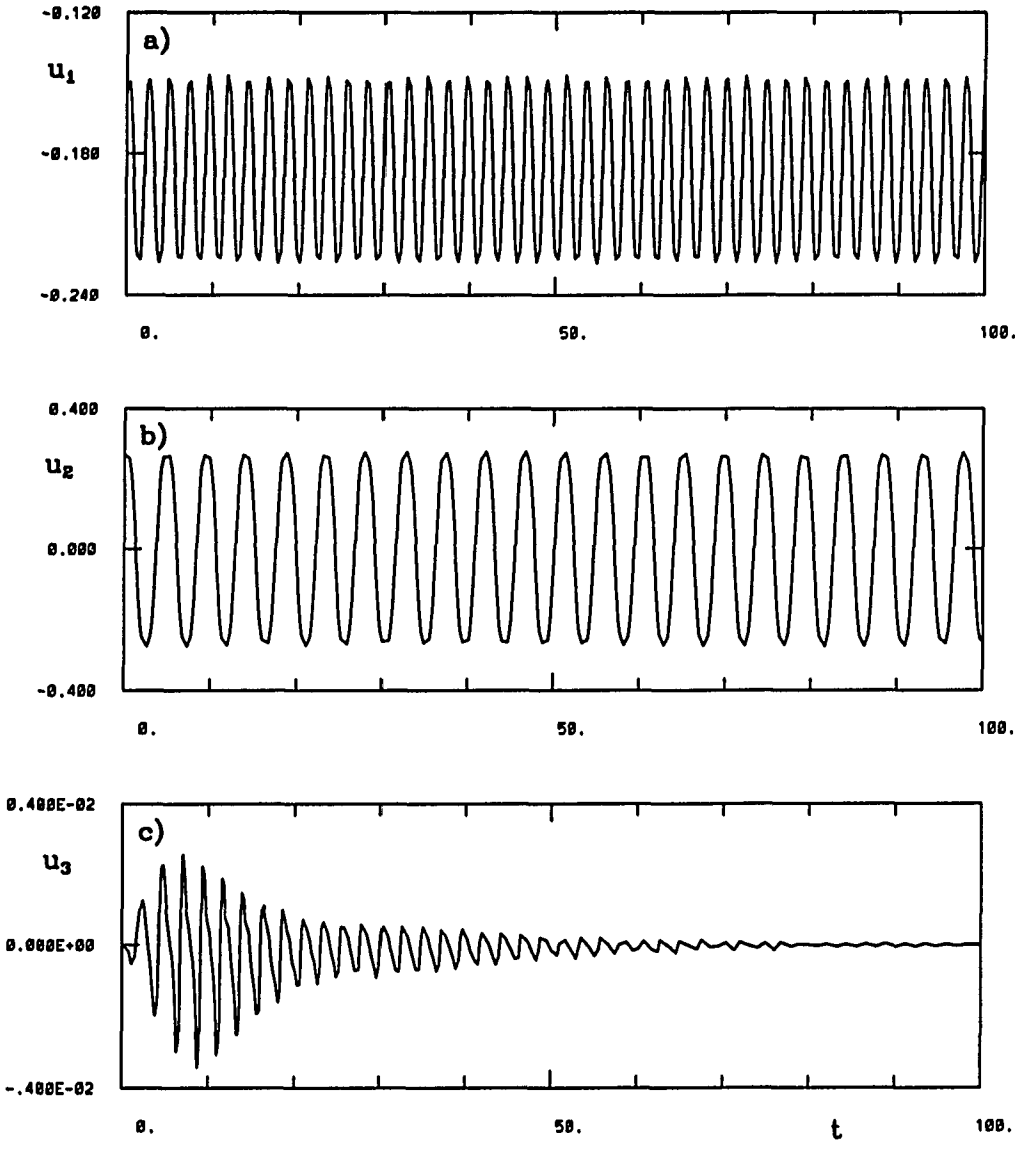


Figure 2.9: Time evolution of the velocity at the location $x_1 = 1.125$, $x_2 = 0.098$, $x_3 = 0$ at Reynolds number $Re = 175$ from a three-dimensional simulation of the reduced system A for wake flow, showing that the three-dimensional perturbation vanishes: a) $x_1$-component; b) $x_2$-component; c) $x_3$-component.

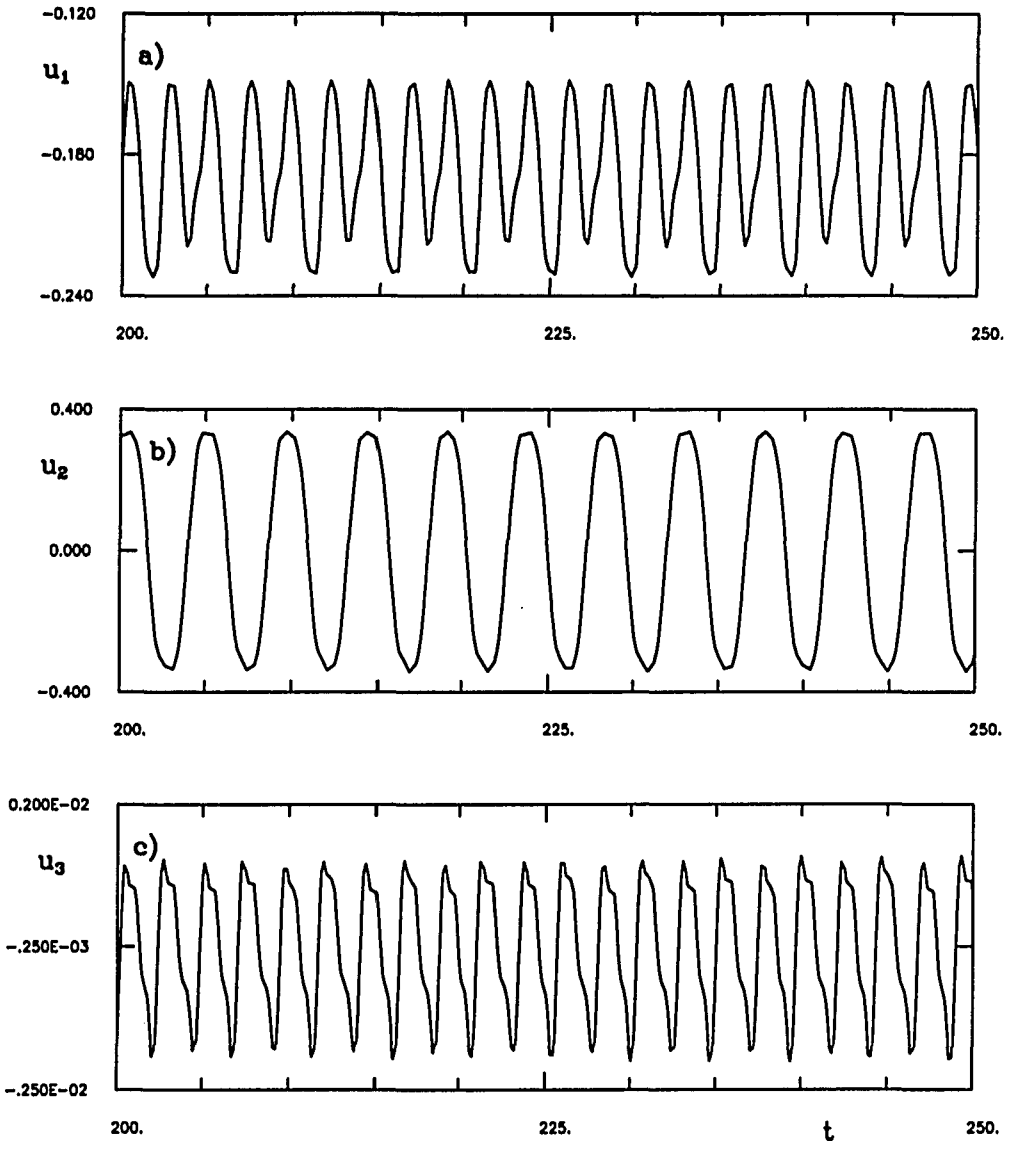


Figure 2.10: Time evolution of the velocity at the location $x_1 = 1.125$, $x_2 = 0.089$, $x_3 = 0$ at Reynolds number $Re = 230$ from a three-dimensional simulation of the reduced system A for wake flow, showing a three-dimensional periodic flow: a) $x_1$-component; b) $x_2$-component; c) $x_3$-component.

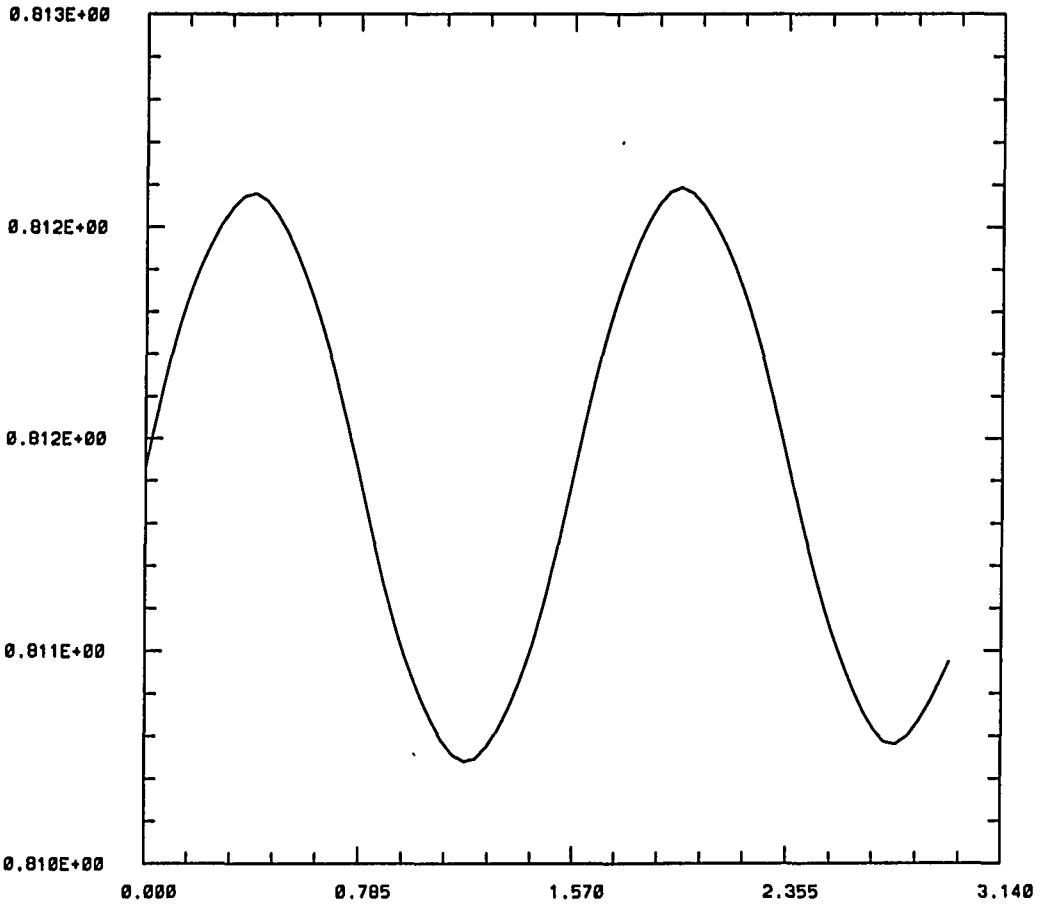


Figure 2.11: Temporal mean velocity distribution $U_t$ versus $x_3$ at $x_2 = 0.098$ from the three-dimensional simulation of the reduced system A for wake flow at Reynolds number $Re = 230$.

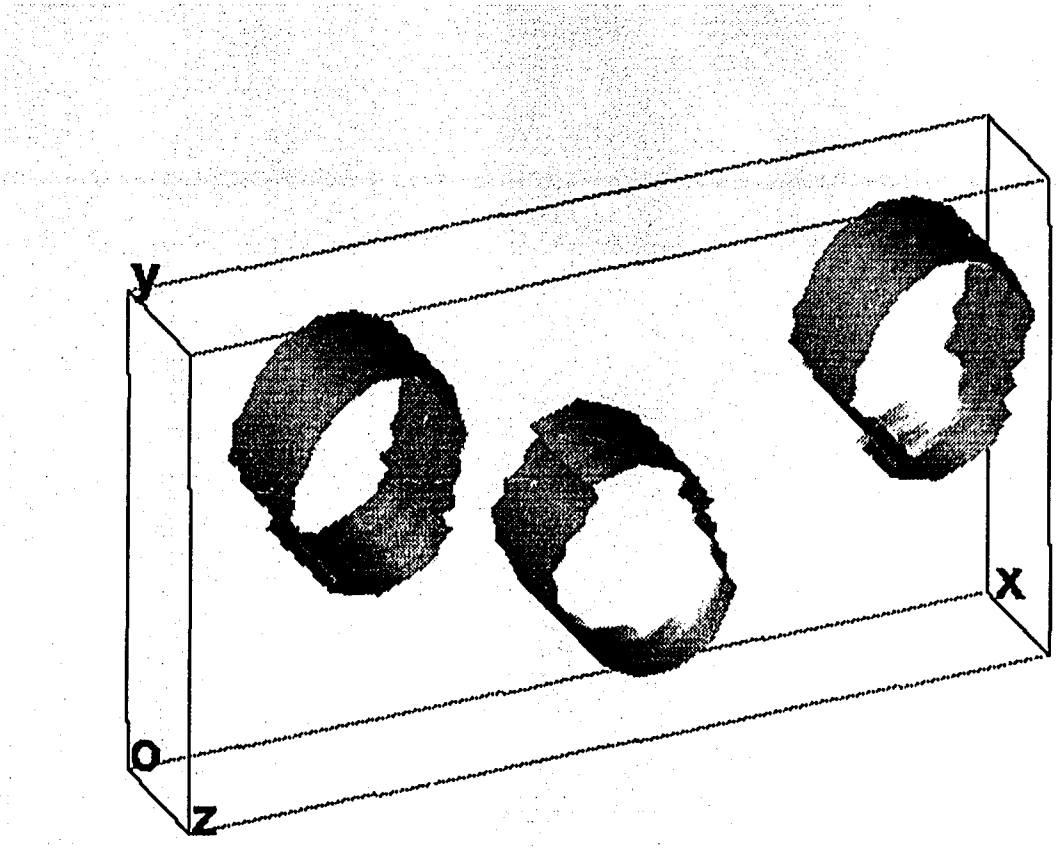


Figure 2.12: Three-dimensional view of an iso-surface of the sum of all three vorticity components $|\omega_1| + |\omega_2| + |\omega_3|$ at $Re = 230$ from a three-dimensional simulation of the reduced system A for wake flow.

## 2.5 The Karman Street as a Solution of Forced Navier-Stokes Equations in Simple Geometry

In this section we introduce an external force in the Navier-Stokes equations and derive a "reduced" system which we refer to our reduced system B. Our approach can be regarded as an extension of the Komogorov flow (Arnol'd and Meshalkin, 1960) defined in a periodic box, which is the solution of the two-dimensional Navier-Stokes equations with a uni-directional, time independent, sinusoidal force $(\nu \sin y, 0)$. It was introduced by Kolmogorov in a seminar to study the phenomenon of transition to turbulence. For large viscosity values, the only stable flow is the parallel shear flow $(\sin y, 0)$ which is referred to as the basic Kolmogorov flow. The stability analysis was carried out by Meshalkin and Sinai (1961) who showed that this stationary flow is unstable when the viscosity reaches a certain critical value. The subsequent sequence of bifurcations as the viscosity decreases has been studied numerically by Nicolaenko and She (1990). In the case of the simulation of a wake flow with periodic condition, it seems also natural to introduce a forcing (see our introduction). The exact expression of the force we choose is given below. The solutions of such a reduced system are then investigated numerically. At low Reynolds numbers, a parallel shear flow is stable, which we refer to as the basic flow in analogy with the Kolmogorov flow. At higher Reynolds number, this basic flow becomes unstable, developing into a staggered vortex street closely resembling the von Karman street experimentally observed or that obtained by direct numerical simulation of the complete system resolving the thin boundary layer around the body.

### 2.5.1 Formulation of the Reduced System with External Forcing

The incompressible Navier-Stokes equations with an external forcing can be written in the following form

$$\frac{\partial \mathbf{v}}{\partial t} = \mathbf{v} \times \omega - \nabla \Pi + \frac{1}{Re} \nabla^2 \mathbf{v} + \mathbf{F} \tag{2.38}$$

$$\nabla \cdot \mathbf{v} = 0 \tag{2.39}$$

where $\omega = \nabla \times \mathbf{v}$ is the vorticity, $\Pi = p + \frac{1}{2}|\mathbf{v}|^2$ the pressure head and $\mathbf{F}$ the external forcing term we introduce to suppress the artificial viscous damping (see the introduction). The Strouhal and Reynolds numbers are defined as $St = fd/U_\infty$ and $Re = U_\infty d/\nu$, where $d$ is the diameter of the cylinder, $U_\infty$ the free stream velocity at infinity, $\nu$ the kinematic viscosity and $f$ the frequency of the oscillations when a temporally periodic solution is obtained.

Here we consider the two-dimensional problem only (although the method could be applied to three dimensional problems as well). The periodic boundary condition is applied in the streamwise ($x_1$) direction

$$\mathbf{v}(x_1 + \frac{2\pi}{\alpha_1}, x_2, t) = \mathbf{v}(x_1, x_2, t) \tag{2.40}$$

where $\alpha$ is the smallest streamwise wavenumber in the computation. The flow reaches the free stream as $x_2 \to \pm\infty$, namely

$$\lim_{x_2 \to \pm\infty} \mathbf{v} = U_\infty \mathbf{e}_1. \tag{2.41}$$

The infinite domain in the $x_2$-direction is transformed into a finite one through a coordinate mapping $x_2 = Y(\eta)$ where

$$x_2 = L \tan \eta \quad (|x_2| < \infty, |\eta| < \pi/2). \tag{2.42}$$

The initial condition is assumed to be a parallel flow superposed to a small disturbance, i.e.

$$\mathbf{v} = U(x_2)\mathbf{e}_1 + \mathbf{u}_0(x_1, x_2) \qquad \text{at} \quad t = 0. \tag{2.43}$$

where the velocity distribution $U(x_2)$ is assumed to be known, as we will discuss in detail later.

The numerical algorithms used here are the same as those used in the previous sections of this chapter which consist of a spectral expansion in Fourier modes for the spatial discretization and a fractional-step method for the advancement in time.

### 2.5.2 The External Forcing Term

Our basic idea is to simulate a wake flow via a reduced system by replacing the object with a forcing term $F$ for which we propose two forms. The first one is

$$\mathbf{F} = < \mathbf{u} \cdot \nabla \mathbf{u} > - \frac{1}{Re} \frac{d^2 U}{dx_2^2} \mathbf{e}_1, \tag{2.44}$$

the other one being the linearized version of the first one:

$$\mathbf{F} = - \frac{1}{Re} \frac{d^2 U}{dx_2^2} \mathbf{e}_1, \tag{2.45}$$

where $U(x_2)$ is a flow velocity profile with a defect which can be obtained, for instance, from the experimental measurement of the mean velocity distribution of the wake behind a cylinder, $\mathbf{u}$ represents the remaining velocity, once $U(x_2)\mathbf{e}_1$ has been substracted, i.e.

$$\mathbf{v} = U \mathbf{e}_1 + \mathbf{u} \tag{2.46}$$

and $< \ >$ denotes the spatial average in the $x_1$-direction

$$< \ > = \frac{1}{L_1} \int_0^{L_1} dx_1 \tag{2.47}$$

in which $L_1$ is the length of the domain in the $x_1$-direction.

After substituting the forcing term $\mathbf{F}$ (2.44) or (2.45) into the incompressible Navier-Stokes equations (2.38) and (2.39), it is straightforward to see that the parallel flow $\mathbf{U}$ is a steady solution of the governing equations of the reduced system (2.38) and (2.39). In analogy with the Kolmogorov flow recalled in the introduction, we refer

to this flow as our "basic" flow. Therefore, the wake flow problem can be approached through a stability analysis of the parallel basic flow. Indeed, following Triantafyllou (1989) who connected the absolute instability of the flow to the existence of the Karman street through a linear invicid theory, we can construct a corresponding viscous stability analysis of the "basic" flow for the forced Navier-Stokes equations (2.38) and (2.39).

We would like to point out that the necessity for introducing the external forcing term in the forms (2.44) or (2.45) can be justified by examining the averaged governing equations. Suppose that (2.46) holds in such a way that

$$< \mathbf{u} >= 0, \tag{2.48}$$

where the brackets denote the spatial average in the streamwise $x_1$ direction. This, of course, is exactly satisfied if U is the spatial mean velocity, which coincides with the temporal mean for a traveling wave. We then substitute this decomposition into the governing equations (2.38) and derive

$$\frac{\partial \mathbf{u}}{\partial t} + U\frac{\partial \mathbf{u}}{\partial x_1} + \frac{dU}{dx_2}u_2\mathbf{e}_2 + \mathbf{u}\cdot\nabla\mathbf{u} = -\nabla p + \frac{1}{Re}\nabla^2\mathbf{u} + \frac{1}{Re}\frac{d^2U}{dx_2^2}\mathbf{e}_1. \tag{2.49}$$

Taking the spatial average $<\ >$ of the previous equation and assuming that the flow is a traveling wave, i.e.

$$\frac{\partial \mathbf{u}}{\partial t} = c\frac{\partial \mathbf{u}}{\partial x_1}$$

where $c$ is the traveling speed, we obtain

$$\mathbf{F} = < \mathbf{u}\cdot\nabla\mathbf{u} > -\frac{1}{Re}\frac{d^2U}{dx_2^2}\mathbf{e}_1 + (U+c)[\mathbf{u}(0,x_2,t) - \mathbf{u}(L_1,x_2,t)] - \nabla < p > . \tag{2.50}$$

The third term in the right hand side of (2.50) is zero due to the streamwise periodic boundary conditions, and the fourth term representing the gradient of the mean pressure can be neglected in an integration domain chosen not too close to the cylinder. We then obtain (2.44).

The forcing term (2.44) contains two terms. The first one, non-linear, represents the Reynolds stress involving the fluctuations (around the "basic" flow). The second one provides a linear negative viscous force compensating the viscous damping. Slightly above the critical Reynolds number value, at which the parallel basic flow loses its stability, the amplitude of the fluctuation can be expected to be small, so that the linearization of (2.44) is reasonable, leading to the linearized external forcing term (2.45).

### 2.5.3 Numerical Results and Discussions

We have performed the numerical integration of the reduced system described above at a Reynolds number value of $Re = 56$, with a streamwise length $L = 4.33d$ (where $d$ is the diameter of the cylinder, as we defined earlier). The parallel basic flow $U$, which we need to input in the forcing term, is taken from Triantafyllou (1986) who curve fitted Kovasnay's (1949) experimental measurement of the temporal averaged velocity profile at a downstream distance $3.5d$ from the cylinder.

First, we have numerically integrated the reduced system without the external forcing term $\mathbf{F}$. As discussed in our introduction, the initial disturbance grows at first and then decays ultimately while the behavior of the real flow is that of a vortex street. The corresponding results are shown in Figure 2.13.

After adding the linear forcing term $\mathbf{F}$ given by (2.45), we observe the growth of the initial disturbance which eventually develops into a von Karman vortex street as shown in Figures 2.14 and 2.15. The corresponding Strouhal number which can be calculated from the obtained time series of Figure 2.14 is $St = 0.16$, close to the experimental value $St = 0.13$. Figure 2.15 displays the iso-vorticity contours which show the alternating vortices characteristic of a von Karman street. A careful examination of Figure 2.14 shows that the asymptotic time mean velocity of the obtained solution deviates from the basic velocity profile $U$ which we have chosen to

be the experimentally obtained temporal mean velocity distribution in a wake flow behind a cylinder. This discrepancy can be seen more clearly in Figure 2.16. This is due to the error made in the linearization (2.45) of the forcing term, as we now show by including the nonlinear term in (2.44). The results obtained by this new computation are plotted in Figure 2.17 and Figure 2.18. They clearly demonstrates that after a short transient the velocity oscillates around the basic velocity profile, namely the mean velocity experimentally measured.

## 2.6 Conclusions

Numerical simulations of wake flows are time and memory consuming because of the thin boundary layer around the surface of the body. In this work, we have replaced the complex no-slip boundary condition on the surface of the cylinder with simple streamwise and spanwise periodic conditions by imposing at each time step the (constant) spatial mean velocity profile. Such assumption is valid if the spatial mean velocity is time independent and therefore can be used for statistically steady flows only. An efficient numerical simulation, namely a spectral method using Fourier modes, could then be derived and the reduced system integrated. Results of various numerical simulations using this method include the occurrence of the primary and secondary instabilities of the flow. Although the technique was implemented on a wake flow behind a cylinder, it should be applicable to flows generated by bodies of any shape, as well as other types of flows. It requires the input of the mean flow velocity profile which, in most cases, is documented in the literature (and can be easily determined either experimentally or numerically) and slowly varies with Reynolds number. A relaxation of this constraint has been achieved by adding a forcing term in the Navier-Stokes equations which overcomes the unrealistic viscous diffusion occurring for a parallel shear flow. An alternative reduced numerical system was then derived, also reproducing successfully the Karman vortex street. Finally, we should

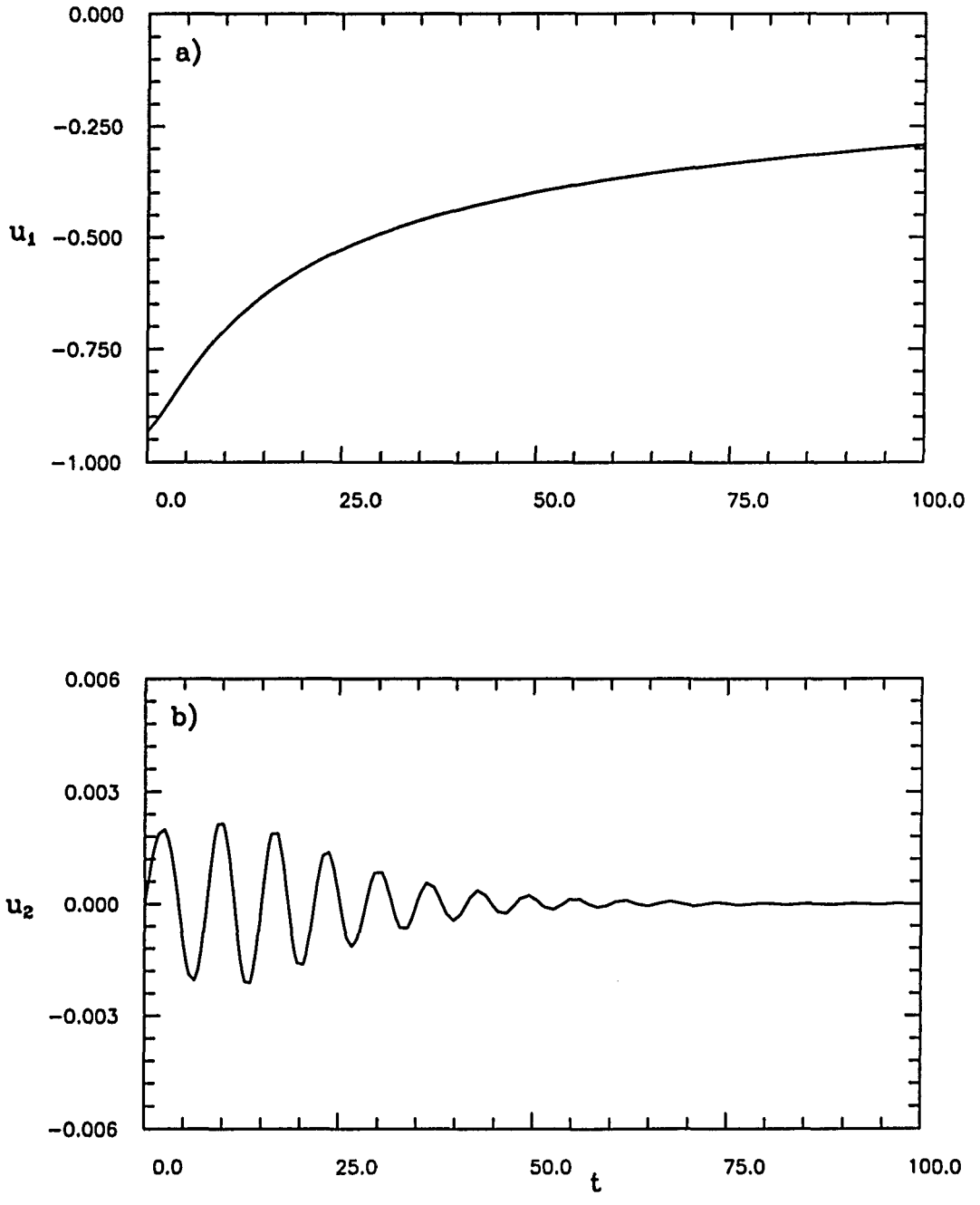


Figure 2.13: Wake flow simulation via the reduced system B. Time series of the velocity at the location $x_1 = 1.35$ on the centerline ($x_2 = 0$) numerically obtained by integrating our reduced system (2.38) and (2.39) at Reynolds number ($Re = 56$, with a zero forcing term, i.e. $\mathbf{F} = 0$.): a) the streamwise velocity component $u_1$, b) the normal velocity component $u_2$.

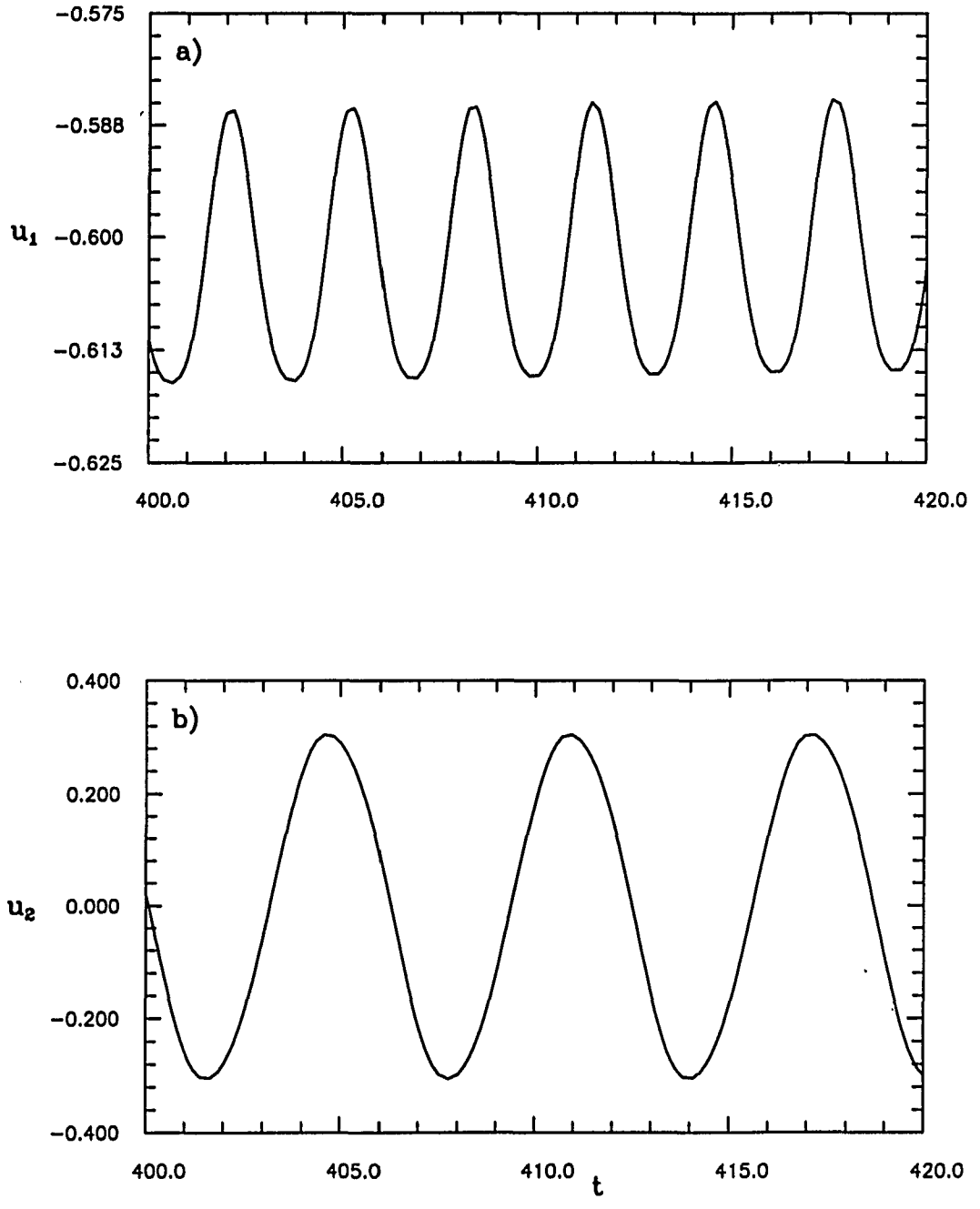


Figure 2.14: Wake flow simulation via the reduced system B. Time series of the velocity at the location $x_1 = 1.35$ on the centerline ($x_2 = 0$) numerically obtained by integrating our reduced system (2.38) and (2.39) at Reynolds number $Re = 56$, with the linear forcing term (2.45): a) the streamwise velocity component $u_1$, b) the normal velocity component $u_2$.

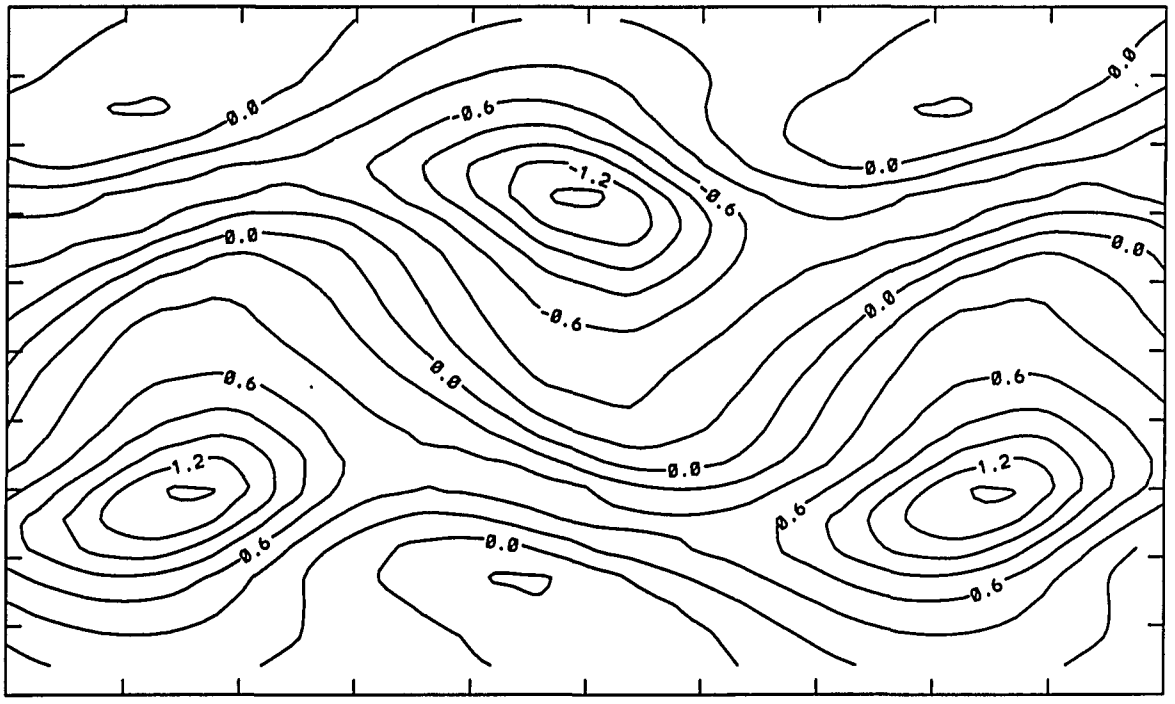


Figure 2.15: Wake flow simulation via the reduced system B. Iso-vorticity contours of the same flow as in Figure 2.14.

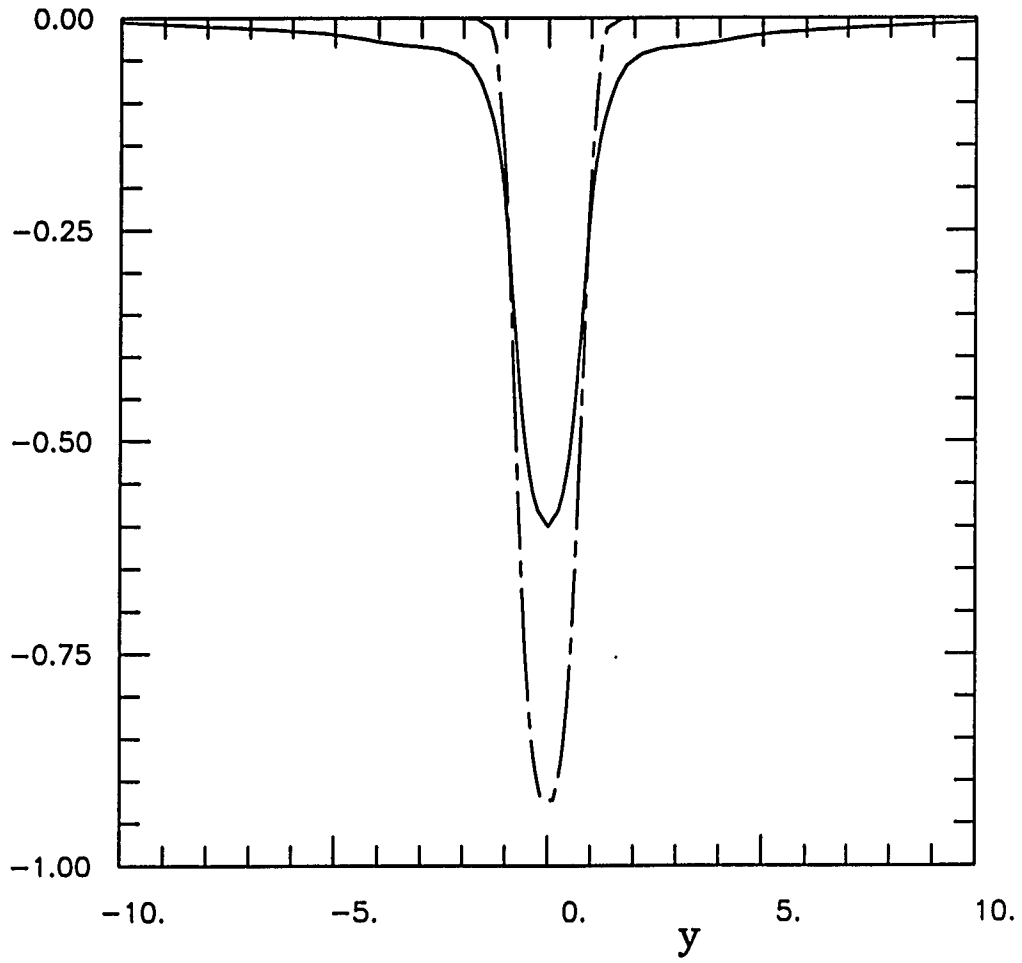


Figure 2.16: Wake flow simulation via the reduced system B. Comparison between the temporal mean velocity profile of the same flow as in Figure 2.14 (solid line) and the basic flow, namely the experimentally obtained (temporal) mean velocity (dashed line).

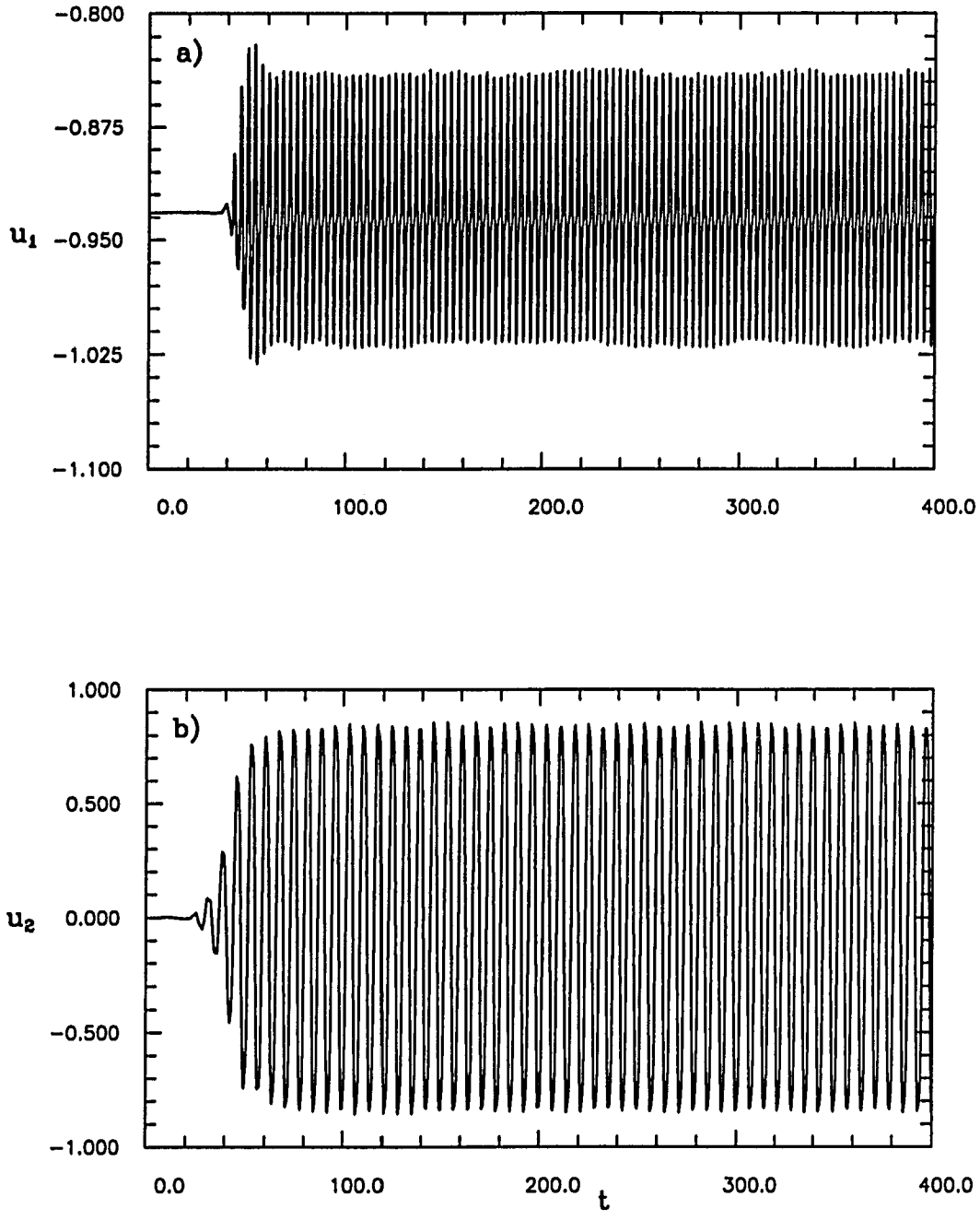


Figure 2.17: Wake flow simulation via the reduced system B. Time series of the velocity at the location $x_1 = 1.35$ on the centerline ($x_2 = 0$) numerically obtained by integrating our reduced system (2.38) and (2.39) at Reynolds number $Re = 56$, with the nonlinear forcing term (2.44): a) the streamwise velocity component $u_1$, b) the normal velocity component $u_2$.

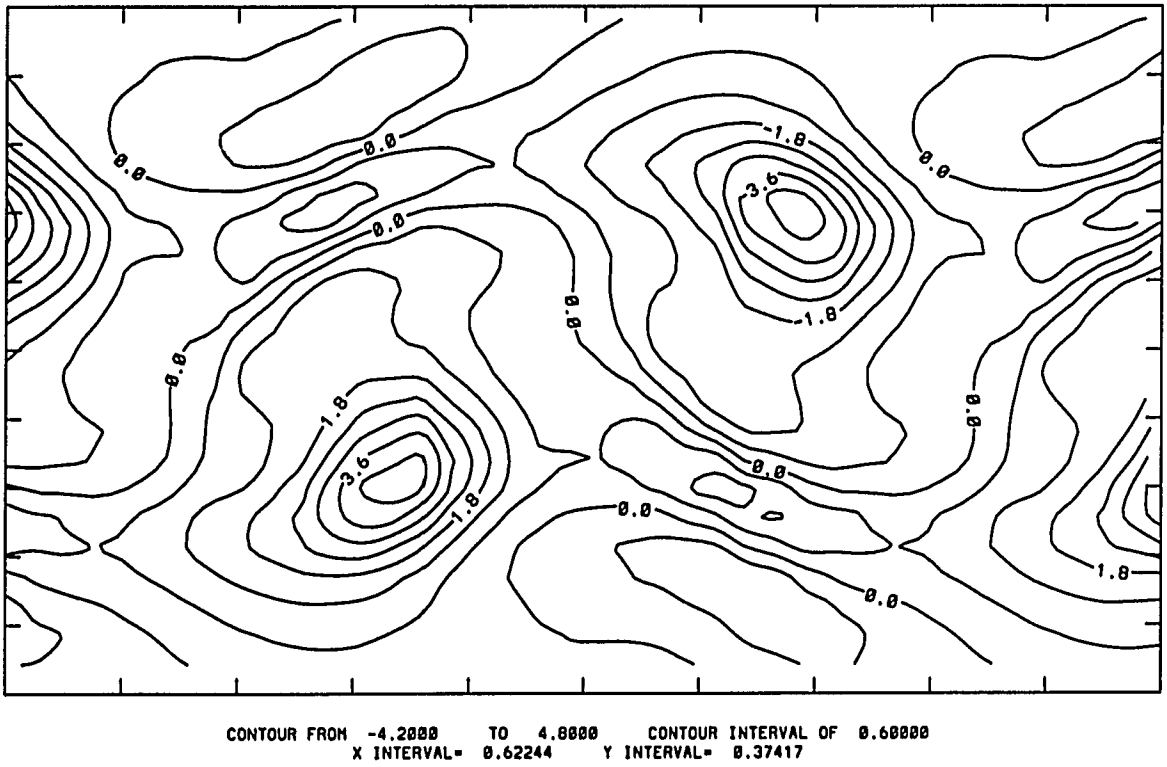


Figure 2.18: Wake flow simulation via the reduced system B. Iso-vorticity contours of the same flow as in Figure 2.17.

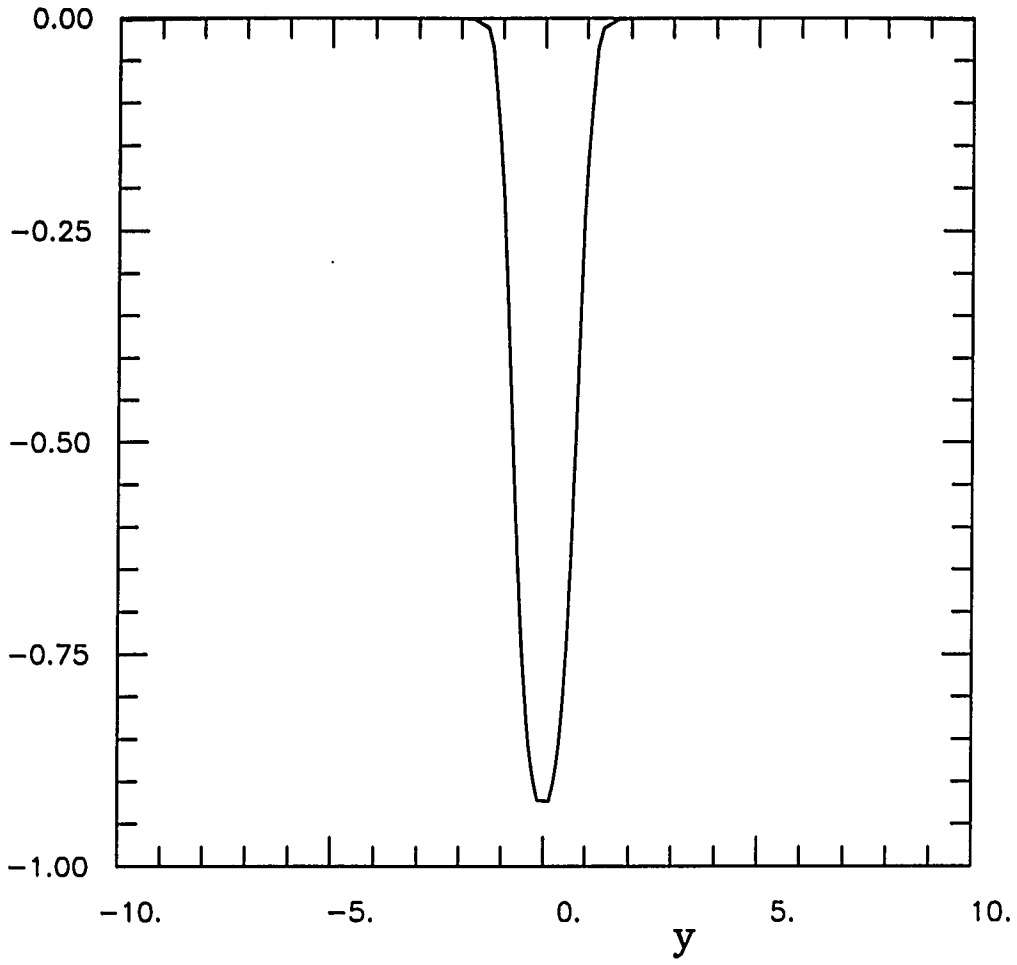


Figure 2.19: Wake flow simulation via the reduced system B. Comparison between the temporal mean velocity profile of the same flow as in Figure 2.17 (solid line) and the basic flow, namely the experimentally obtained (temporal) mean velocity (dashed line), showing the superposition of the two curves.

mention that preliminary results (see Chapter 4) indicate that numerical simulations using reduced systems should be as successful for turbulent wakes as for laminar ones.

# Chapter 3

# Spatio-temporal Analysis of Wake flows

In this chapter, the spatio-temporal structures of laminar and turbulent wake flows are investigated through a biorthogonal decomposition (BOD) analysis, particularly in terms of spatio-temporal symmetries and low-dimensional dynamical system.

The biorthogonal decomposition method will be briefly recalled in Section 3.1. In Section 3.2, the space-time symmetries of the flow behind a cylinder are extracted via the BOD theory. Appearance and breaking of such symmetries will be shown in Section 3.3 and Section 3.4 for a half-cylinder wake flow. Section 3.5 will focus on space-time symmetries of turbulent wake flows. In Section 3.6, a low-dimensional dynamical system is derived for a laminar wake flow past a half-cylinder. Finally, Section 3.7 concludes this chapter.

## 3.1 A Tool for Space-time Analysis: Biorthogonal Decompositions

We now briefly describe the tool we use to analyze the spatio-temporal structure and the symmetries of a wake flow, the biorthogonal decomposition technique first introduced by Aubry et al. (1991).

According to the biorthogonal decomposition theory (originating in linear operator theory), any given space-time function, in our case, the velocity vector $u(x,t)$ where $x$ and $t$ represent the spatial and temporal variables, can be decomposed into spatial orthogonal modes in a Hilbert space $H(X)$ ($x \in X$) and temporal orthogonal modes in a Hilbert space $H(T)$ ($t \in T$) for which there is a one-to-one correspondence between both sets of modes. Such expansions correspond to the spectral decomposition of the operators $\mathbf{U}$ defined as

$$\mathbf{U} : H(X) \rightarrow H(T)$$

such that

$$\forall \phi \in H(X), \ \ (\mathbf{U}\phi)(t) = \int_X u(x,t)\phi(x)d\mu(x) \tag{3.1}$$

where $d\mu(x)$ (resp. $d\tilde{\mu}(t)$) denotes the measure defining the scalar product in $H(X)$ (resp. $H(T)$). The spectral analysis of $\mathbf{U}$ gives a biorthogonal decomposition of $u(x,t)$, which, in case of a compact operator, can be written as

$$u(x,t) = \sum_{n=0}^{N} A_n \phi_n(x)\psi_n(t) \tag{3.2}$$

with

$$A_0 \geq A_1 \geq \ldots \geq A_N > 0,$$

and

$$(\phi_n, \phi_m)_{H(X)} = (\psi_n, \psi_m)_{H(X)} = \delta_{n,m},$$

where the parentheses denote the scalar products in the respective Hilbert spaces. We call the elements of the orthonormal sequence $\phi_n$ in H(X) (spatial modes) "topos" and those of the orthonormal sequence $\psi_n$ in H(T) (temporal modes) "chronos".

The connection between spatial and temporal modes, or generalized dispersion relation, is given by

$$U\phi_n = A_n\psi_n \tag{3.3}$$

A particular example of such a decomposition is the two-dimensional Fourier decomposition for plane waves. Moreover, the spectral decomposition of the operator $\mathbf{U^*U}$ or $\mathbf{UU^*}$, where $\mathbf{U^*}$ is the adjoint operator of $\mathbf{U}$, coincides with the Karhunen-Loéve (KL) expansion if the sampling set needed in the latter consists of consecutive times. The spatio-temporal dynamics can then be studied as an orbit $\xi_t(x)$ defined by

$$\forall x \in X, \;\; \xi_t(x) = u(x,t)$$

in the spatial configuration space

$$\chi(X) = Ker(\mathbf{U})^{\perp}$$

spanned by the $\phi_n$'s or as an orbit $\eta_x(t)$ defined by

$$\forall t \in T, \;\; \eta_x(t) = u(x,t)$$

in the temporal configuration space

$$\chi(T) = Ker(\mathbf{U^*})^{\perp}$$

spanned by the $\psi_n$'s, these two spaces which share the same, *minimal dimension*, being related to each other via the isomorphism $\mathbf{U}$.

In the framework of biorthogonal decompositions, a space-time symmetry naturally appears as a pair of operators $(\tilde{\mathbf{S}}, \mathbf{S})$ (or a group of such operators), $\tilde{\mathbf{S}}$ acting on $H(T)$ and $\mathbf{S}$ on $H(X)$, which interwines the operator $\mathbf{U}$ (3.1), i.e.

$$\tilde{\mathbf{S}}\mathbf{U} = \mathbf{U}\mathbf{S} \tag{3.4}$$

Then each eigenspace in $\chi(X)$ is **S**-invariant and, similarly, each eigenspace in $\chi(T)$ is $\tilde{\mathbf{S}}$-invariant.

## 3.2 Some Space-time Symmetries in Wake Flows

In this section, we analyze the variety of space-time symmetries arising in a certain number of wake flows at various Reynolds numbers. For this purpose, we first need to clearly define a three- dimensional version of the BOD theory, a necessity due to the three-dimensionality of wake flows, particularly at high Reynolds numbers.

A possible three-dimensional version of biorthogonal decompositions is the following. Let us consider a space-time function $\mathbf{u}(\mathbf{x},t)$ defined on $X^3 \times R$, where $X^3$ denotes a three-dimensional spatial domain. We then define the operator

$$\mathbf{U}: \; H(R^3,X^3) \rightarrow H(T)$$

$$\forall \phi \in H(R^3,X^3), \;\; (\mathbf{U}\phi)(t) = \sum_{i=1}^{3} \int u_i(\mathbf{x},t)\phi_i(\mathbf{x})d\mathbf{x}, \tag{3.5}$$

the adjoint operator being

$$\mathbf{U}^*: \; H(T) \rightarrow H(R^3,X^3)$$

such that

$$\forall \psi \in H(T), \;\; (\mathbf{U}^*\psi)_i(\mathbf{x}) = \int \overline{u_i(\mathbf{x},t)}\psi(t)dt. \tag{3.6}$$

The scalar product in $H(R^3,X^3)$ is defined by

$$(\phi,\phi') = \sum_{i=1}^{3} \int \phi_i(\mathbf{x})\overline{\phi_i'(\mathbf{x})}d\mathbf{x}$$

and as usual the scalar product in $H(T)$ is

$$(\psi,\psi') = \int \psi(t)\overline{\psi'(t)}dt$$

where the bar represents the complex conjugate. The biorthogonal decomposition of the function $\mathbf{u}(\mathbf{x},t)$ consists of the spectral decomposition of the operator $\mathbf{U}$, or

equivalently, that of the matrix operator

$$\mathbf{V} = \begin{pmatrix} 0 & \mathbf{U}^* \\ \mathbf{U} & 0 \end{pmatrix} \tag{3.7}$$

defined on $H(X) \oplus H(T)$, the eigenvectors of $\mathbf{V}$ being

$$\begin{pmatrix} \phi \\ \psi \end{pmatrix}. \tag{3.8}$$

If $\mathbf{V}$ is a compact operator, then $\mathbf{u}(\mathbf{x}, t)$ can be expanded as

$$\mathbf{u}(\mathbf{x}, t) = \sum_{n=0}^{N} A_n \phi_n(\mathbf{x}) \psi_n(t) \tag{3.9}$$

where the topos (resp. the chronos) are orthogonal in the sense of the scalar product in $H(R^3, X^3)$ (resp. in $H(T)$).

We can now define the spatial and temporal symmetry operators $\mathbf{S}$ and $\tilde{\mathbf{S}}$ as usual

$$\mathbf{S}: \quad H(R^3, X^3) \to H(R^3, X^3)$$

and

$$\tilde{\mathbf{S}}: \quad H(T) \to H(T).$$

Like in the one-dimensional case, we say that the function $\mathbf{u}(\mathbf{x}, t)$ enjoys a space-time symmetry if there exist symmetry operators $\mathbf{S}$ and $\tilde{\mathbf{S}}$ which, as well as their adjoints, intertwin the operator $\mathbf{U}$:

$$\mathbf{US} = \tilde{\mathbf{S}}\mathbf{U} \tag{3.10}$$

and

$$\mathbf{US}^* = \tilde{\mathbf{S}}^*\mathbf{U}. \tag{3.11}$$

These properties are equivalent to the commutation of the operator $\mathbf{V}$ with the symmetry matrix operator $\mathbf{Q}$

$$\mathbf{Q} = \begin{pmatrix} \mathbf{S} & 0 \\ 0 & \tilde{\mathbf{S}} \end{pmatrix}, \tag{3.12}$$

such that

$$\mathbf{QV} = \mathbf{VQ}. \tag{3.13}$$

As in the one-dimensional case, if $\mathbf{u}(\mathbf{x}, t)$ enjoys a space-time symmetry, then if

$$\begin{pmatrix} \phi \\ \psi \end{pmatrix} \tag{3.14}$$

is an eigenvector of the operator $V$, then

$$\begin{pmatrix} S\phi \\ \tilde{S}\psi \end{pmatrix} \tag{3.15}$$

is also an eigenvector of $\mathbf{V}$ associated with the same eigenvalue.

This implies that each spatial eigenspace in $\chi(X)$ is $\mathbf{S}$-invariant, and each temporal eigenspace in $\chi(T)$ is $\tilde{\mathbf{S}}$-invariant.

Note that $\mathbf{S}$, defined on $H(R^3, X^3)$, can take the general form

$$\phi \rightarrow \left[ \begin{pmatrix} S_{11} & S_{12} & S_{13} \\ S_{21} & S_{22} & S_{23} \\ S_{31} & S_{32} & S_{33} \end{pmatrix} \begin{pmatrix} \phi_1 \\ \phi_2 \\ \phi_3 \end{pmatrix} \right]$$

which will be used later for describing interesting symmetries.

### 3.2.1 Translation Symmetries

Well-known examples of $\mathbf{S}$ and $\tilde{\mathbf{S}}$ are the translation symmetries characterizing traveling waves, which have been described in terms of the biorthogonal decomposition in previous works (Aubry et al., 1992(b)). In wake flows, traveling waves are present at low Reynolds numbers, if we neglect the decay of the wake intensity downstream, which is a reasonable assumption at least locally. Specifically, we need

to consider the translation symmetry in the $x_1$-direction at a fixed cross-stream position $x_2, x_3$. Then the symmetry operators associated with **u** intertwine the operator **U**

$$\mathbf{U}\mathbf{S}_1 = \tilde{\mathbf{S}}_1\mathbf{U} \tag{3.16}$$

where $\mathbf{S}_1$ and $\tilde{\mathbf{S}}_1$ are defined by

$$\mathbf{S}_1\phi(x_1) = \phi(x_1 - x_{10}) \tag{3.17}$$

and

$$\tilde{\mathbf{S}}_1\psi(t) = \psi(t - t_0) \tag{3.18}$$

for all real numbers $x_{10}$ and $t_0$ satisfying the relation $x_{10} + ct_0$=0, where c is the traveling wave speed.

### 3.2.2 Statistical Reflection Symmetry

For wake flows behind a body whose shape is invariant by reflection with respect to the mid-plane $x_2 = 0$, such as a full or half circular cylinder, a more generalized, statistical form of the reflection symmetry exists *at all Reynolds numbers.* Statistical quantities, such as the temporal mean flow and the spatial two-point correlation, are invariant by reflection symmetry. This symmetry can be clearly observed at high Reynolds numbers where the flow is strongly turbulent as well as at small Reynolds numbers, for instance when the flow is steady or consists of a Karman street. In the intermediate range of Reynolds numbers, the practical observation of the symmetry depends on the averaging procedure used to obtain the statistics, as we will discuss later in Section 3.4.

We consider the space of functions of the variable $x_2 \in R$ with values in $R^3$. Let us denote this functional space by $L^2(R, C^3)$, in which we define the following inner product

$$(\phi, \phi')_{x_2} = \sum_{i=1}^{3} \int_R \phi_i(x_2)\overline{\phi_i'(x_2)}dx_2$$

where the bar refers to the complex conjugate. It is well-known that we can construct an isomorphism between $L^2(R, C^3)$ and $C^3 \otimes L^2(R)$ in the following way:

$$\mathbf{e}_1 \otimes \phi \Leftrightarrow \begin{pmatrix} \phi \\ 0 \\ 0 \end{pmatrix} \qquad \mathbf{e}_2 \otimes \phi \Leftrightarrow \begin{pmatrix} 0 \\ \phi \\ 0 \end{pmatrix} \qquad \mathbf{e}_3 \otimes \phi \Leftrightarrow \begin{pmatrix} 0 \\ 0 \\ \phi \end{pmatrix}$$

where

$$\mathbf{e}_1 = \begin{pmatrix} 1 \\ 0 \\ 0 \end{pmatrix} \quad \mathbf{e}_2 = \begin{pmatrix} 0 \\ 1 \\ 0 \end{pmatrix} \quad \mathbf{e}_3 = \begin{pmatrix} 0 \\ 0 \\ 1 \end{pmatrix}$$

define the canonical basis of $C^3$ and $\phi \in L^2(R)$.

The operator

$$\mathbf{G} : C^3 \otimes L^2(R) \rightarrow C^3 \otimes L^2(R)$$

is defined as

$$\forall \phi \in C^3 \otimes L^2(R), \quad \mathbf{G}\phi = \int_R G(x_2, x_2')\phi(x_2')dx_2'$$

in which

$$\mathbf{G} = \mathbf{U}^*\mathbf{U}$$

is the operator whose kernel is the spatial two-point correlation tensor and the reflection operator

$$\mathbf{R} : L^2(R) \rightarrow L^2(R)$$

is such that

$$(\mathbf{R}\phi)(x_2) = \phi(-x_2).$$

We now define what we refer to as the statistical reflection symmetry of the flow.

**Definition 1** *The flow* $\mathbf{u}(x_2, t)$ *is statistically symmetric under reflection if*

$$(\mathbf{K} \otimes \mathbf{R})\mathbf{G} = \mathbf{G}(\mathbf{K} \otimes \mathbf{R}) \tag{3.19}$$

*where*

$$K = \begin{pmatrix} 1 & 0 & 0 \\ 0 & -1 & 0 \\ 0 & 0 & 1 \end{pmatrix}.$$

A problem which is statistically symmetric under reflection enjoys some important properties associated with the operator **G** and **R**.

**Lemma 1** *The following properties hold.*

*(i)* $(\mathbf{K} \otimes \mathbf{R})^2 = \mathbf{1}$ , *where* $\mathbf{1}$ *represents the unit operator.*

*(ii) Let*

$$\mathbf{P}^+ = \frac{\mathbf{1}}{2}(\mathbf{1} + \mathbf{K} \otimes \mathbf{R})$$

*and*

$$\mathbf{P}^- = \frac{\mathbf{1}}{2}(\mathbf{1} - \mathbf{K} \otimes \mathbf{R}) = \mathbf{1} - \mathbf{P}^+$$

$\mathbf{P}^+$ *and* $\mathbf{P}^-$ *are two projectors such that*

*(iii)* $\mathbf{G} = \mathbf{P}^+\mathbf{G}\mathbf{P}^+ + \mathbf{P}^-\mathbf{G}\mathbf{P}^-$ *as* $\mathbf{P}^+\mathbf{G} = \mathbf{G}\mathbf{P}^+$ *and* $\mathbf{P}^-\mathbf{G} = \mathbf{G}\mathbf{P}^-$

*Therefore the space* $C^3 \otimes L^2(R) = \mathcal{H}$ *splits into two orthogonal subspaces, each of them being invariant by* **G**.

*Proof*

(i) Notice that $\mathbf{K}^2 = \mathbf{1}$ and also $\mathbf{R}^2 = \mathbf{1}$, therefore (i) is proved.

(ii) Using (i), (ii) can be proved as follows

$$(\mathbf{P}^+)^2 = \frac{1}{4}(\mathbf{1} + \mathbf{K} \otimes \mathbf{R})(\mathbf{1} + \mathbf{K} \otimes \mathbf{R}) = \frac{1}{2}(\mathbf{1} + \mathbf{K} \otimes \mathbf{R}) = \mathbf{P}^+$$

and

$$(\mathbf{P}^+)^* = \frac{1}{2}(\mathbf{1} + \mathbf{K}^* \otimes \mathbf{R}^*) = \mathbf{P}^+$$

so that $\mathbf{P}^+$ is an orthogonal projection which in turn implies that $\mathbf{P}^- = \mathbf{1} - \mathbf{P}^+$ is an orthogonal projection.

(iii) Since $(\mathbf{K} \otimes \mathbf{R})\mathbf{G} = \mathbf{G}(\mathbf{K} \otimes \mathbf{R})$ it is easy to see that

$$\mathbf{P}^+\mathbf{G} = \mathbf{G}\mathbf{P}^+$$

and

$$\mathbf{P}^-\mathbf{G} = \mathbf{G}\mathbf{P}^-.$$

Therefore, we have

$$\mathbf{P}^+\mathbf{G}\mathbf{P}^- = \mathbf{P}^+\mathbf{G}(1 - \mathbf{P}^+) = \mathbf{G}\mathbf{P}^+(1 - \mathbf{P}^+) = 0. \tag{3.20}$$

In the same way, we have

$$\mathbf{P}^-\mathbf{G}\mathbf{P}^+ = 0. \tag{3.21}$$

We thus obtain

$$\begin{aligned} \mathbf{G} = \; & \mathbf{P}^+\mathbf{G}\mathbf{P}^+ + \mathbf{P}^+\mathbf{G}(1 - \mathbf{P}^+) + (1 - \mathbf{P}^+)\mathbf{G}\mathbf{P}^+ + (1 - \mathbf{P}^+)\mathbf{G}(1 - \mathbf{P}^+) \\ = \; & \mathbf{P}^+\mathbf{G}\mathbf{P}^+ + (1 - \mathbf{P}^+)\mathbf{G}(1 - \mathbf{P}^+) \\ = \; & \mathbf{P}^+\mathbf{G}\mathbf{P}^+ + \mathbf{P}^-\mathbf{G}\mathbf{P}^- \end{aligned} \tag{3.22}$$

and

$$\mathcal{H} = \mathbf{P}^+\mathcal{H} \oplus \mathbf{P}^-\mathcal{H}, \tag{3.23}$$

i.e. $\mathbf{G}$ is the sum of two projections, and $\mathcal{H}$ can be split into two orthogonal subspaces $\mathbf{P}^+\mathcal{H}$ and $\mathbf{P}^-\mathcal{H}$, the former corresponding to the set of vectorial functions whose first and third (resp. second) components are even (resp. odd) functions of $x_2$, also called varicose modes, the latter corresponding to the set of vectorial functions whose first and third (resp. second) components are odd (resp. even) functions of $x_2$, also called sinuous modes.

It is useful to find the relation between the statistical reflection symmetry and a dilation symmetry, since the later plays an important role in turbulent flows, as we will see in Chapter 3. We define a dilation symmetry by the operator $\mathbf{S}_\lambda$

$$\mathbf{S}_\lambda : \quad C^3 \otimes L^2(R) \Rightarrow C^3 \otimes L^2(R)$$

such that

$$\forall \phi \in C^3 \otimes L^2(R), \ \ \mathbf{S}_\lambda \phi(x_2) = \phi(\lambda x_2)$$

**Lemma 2** *If the flow* $\mathbf{u}(x_2, t)$ *is statistically symmetric under reflection, i.e.*

$$(\mathbf{K} \otimes \mathbf{R})\mathbf{G} = \mathbf{G}(\mathbf{K} \otimes \mathbf{R})$$

*and statistically symmetric under dilation, i.e. there exists a real* $\lambda \in R$ *such that*

$$\mathbf{S}_\lambda \mathbf{G} = \mathbf{G}\mathbf{S}_\lambda,$$

*then the operator* $\mathbf{S}_\lambda$ *and* $\mathbf{K} \otimes \mathbf{R}$ *commute, i.e.*

$$(\mathbf{K} \otimes \mathbf{R})\mathbf{S}_\lambda = \mathbf{S}_\lambda(\mathbf{K} \otimes \mathbf{R})$$

*and*

$$\mathbf{S}_\lambda = \mathbf{P}^+\mathbf{S}_\lambda\mathbf{P}^+ + \mathbf{P}^-\mathbf{S}_\lambda\mathbf{P}^-$$

*where* $\mathbf{P}^+$ *and* $\mathbf{P}^-$ *are the projectors defined in Lemma 1.*

*Proof*

Same as for Lemma 1.

Therefore, the dilation symmetry is satisfied inside the subspace $\mathcal{H}^+$ on the one hand and the subspace $\mathcal{H}^-$ on the other hand.

The decomposition of the operator $\mathbf{G}$ and the splitting of the space $\mathcal{H}$ in case of a statistical reflection symmetry lead to properties of the topos of the biorthogonal decomposition of $\mathbf{u}(\mathbf{x}, t)$, which we announce in the following theorem.

**Theorem 1** *If a problem is statistically symmetric under reflection (see Definition 1), there exists a set of topos $\phi_n$ where $n = 1, 2, \ldots$ such that*

$$(\mathbf{K} \otimes \mathbf{R})\phi_n = \pm\phi_n$$

*Proof* If $\phi_n$ is a topo, it is an eigenfunction of G, so that

$$\mathbf{G}\phi_n = A_n^2\phi_n. \tag{3.24}$$

According to Lemma 1, we have

$$\mathbf{G} = \mathbf{G}^+ + \mathbf{G}^-$$

where $\mathbf{G}^+ = \mathbf{P}^+\mathbf{G}\mathbf{P}^+$ and $\mathbf{G}^- = \mathbf{P}^-\mathbf{G}\mathbf{P}^-$. Substituting this sum and the decomposition

$$\phi_n = \phi_n^+ + \phi_n^- \tag{3.25}$$

where

$$\phi_n^+ = P^+\phi_n \tag{3.26}$$

and

$$\phi_n^- = P^-\phi_n \tag{3.27}$$

into (3.24) and using equations (3.20) and (3.21) lead to

$$(G^+ + G^-)(\phi_n^+ + \phi_n^-) = A_n^2(\phi_n^+ + \phi_n^-)$$

$$G^+\phi_n^+ + G^-\phi_n^- = A_n^2\phi_n^+ + A_n^2\phi_n^-.$$

Since

$$\mathcal{H} = \mathcal{H}^+ + \mathcal{H}^-$$

where $\mathcal{H}^+ = \mathbf{P}^+\mathcal{H}$ and $\mathcal{H}^- = \mathbf{P}^-\mathcal{H}$, the eigenvalue problem (3.24) can be split into

$$\mathbf{G}^+\phi^+ = A_n^2\phi^+$$

and

$$\mathbf{G}^{-}\phi^{-} = A_n^2\phi^{-}$$

where $\phi_n^- \in \mathcal{H}^-$ and $\phi_n^+ \in \mathcal{H}^+$, which is equivalent to

$$\mathbf{G}\phi_n^+ = A_n^2\phi_n^+$$

and

$$\mathbf{G}\phi_n^- = A_n^2\phi_n^-,$$

namely $\phi_n^+$ and $\phi_n^-$ are eigenfunctions of $G$, which proves the theorem.

**Remark 1** *The previous theorem implies that each eigenspace of $\chi(X)$ is spanned by eigenvectors which belong either to $\mathcal{H}^+$ or to $\mathcal{H}^-$. If the dimension of a given eigenspace is one, then the eigenvector belongs necessarily either to $\mathcal{H}^+$ or to $\mathcal{H}^-$. However, if the dimension of the eigenspace is larger than one, then any eigenvector may not have this property, being a linear combination of a vector of $\mathcal{H}^+$ and a vector of $\mathcal{H}^-$. This point can be illustrated by the following one-dimensional example.*

*Example* In this example, the (unique) eigenvalue has a degeneracy of order two and even (resp. odd) eigenfunctions are only particular solutions of the eigenvalue/eigenfunction problem. Let

$$G(y, y') = \cos(y - y') \qquad y, y' \in [-\pi, \pi].$$

It is then easy to see that $\mathbf{G}$ satisfies the one-dimensional symmetric condition of Definition 1, the eigenspace has degeneracy of order two, and the eigenfunctions, corresponding to the same eigenvalue, are

$$\phi_1(y) = \sin(y + y_0) \qquad \text{and} \qquad \phi_2(y) = \cos(y + y_0)$$

which are, obviously, either even or odd modes only for the particular value $y_0 = 0$.

### 3.2.3 Instantaneous Reflection Symmetry

A trivial situation in which the statistical reflection symmetry is satisfied is a steady flow which is invariant through reflection at each time. This is indeed the case of wake flows behind cylinders (more generally, wake flows behind bodies whose shape is invariant by reflection symmetry around their mid-plane) which are, at low Reynolds number, steady, two-dimensional and invariant through reflection about their mid-plane ($x_2 = 0$) so that, at fixed $x_1, x_3$ locations, the velocity satisfies

$$u_1(x_2, t) = u_1(-x_2, t)$$

and

$$u_2(x_2, t) = -u_2(-x_2, t)$$

at all times t. The operator $\mathbf{U}$ associated with $u$ satisfies $\mathbf{US} = \mathbf{U}$ where

$$\mathbf{S} = \mathbf{K} \otimes \mathbf{R}.$$

In this case, the biorthogonal decomposition of $\mathbf{u}(\mathbf{x}, t)$ reduces to one term whose chrono is a constant and the topo belongs to $\mathcal{H}^+$.

We will discuss the changes in the flow behavior in physical space due to the breaking of this instantaneous spatial reflection symmetry as Reynolds number increases, observed in various flows such as wake flows.

### 3.2.4 Space-time $Z_2$ Symmetry

As Reynolds number increases, as the flow undergoes its primary instability and becomes a Karman street where upper and lower vortices alternate in the streamwise direction, the previous instantaneous reflection symmetry is broken. It is, however, interesting to note that such spatial reflection symmetry can be recovered after a time shift, leading to the natural introduction of a space-time symmetry. In

this case, the reflection symmetry is still satisfied statistically in the sense of Definition 1. The space-time symmetry can be expressed by the intertwining operator relation $\mathbf{US} = \tilde{\mathbf{S}}\mathbf{U}$ where $\tilde{\mathbf{S}}$ is defined as

$$\tilde{\mathbf{S}} : L^2(R) \to L^2(R)$$
$$(\tilde{\mathbf{S}}\psi)(t) = \psi(t + \frac{T}{2}) \tag{3.28}$$

where $T$ is the period of the vortex shedding.

Applying Theorem 1 to the present situation, an eigenspace of $\chi(X)$ associated with the eigenvalue $A_n$ can always be spanned by a particularly selected set of topos $\phi_n$, where $n = 1, 2, ...$, such that

$$\phi_n = \pm\mathbf{S}\phi_n. \tag{3.29}$$

Recall that this means that either $\phi_{n_1}$ and $\phi_{n_3}$ are odd functions of $x_2$ and $\phi_{n_2}$ is an even function of $x_2$, or $\phi_{n_1}$ and $\phi_{n_3}$ are even functions of $x_2$ and $\phi_{n_2}$ is an odd function of $x_2$.

It is interesting to note that the knowledge of the full spatial symmetry (including the temporal symmetry) allows us to deduce the following symmetry property of the chronos

$$\psi = \pm\tilde{\mathbf{S}}\psi \tag{3.30}$$

where $\psi$ is any chrono. This property is due to the dispersion relation

$$\psi = \frac{1}{A}\mathbf{U}\phi \tag{3.31}$$

as we now show by applying $\tilde{\mathbf{S}}$ to both sides of the previous formula, which leads to

$$\tilde{\mathbf{S}}\psi = \frac{1}{A}\tilde{\mathbf{S}}\mathbf{U}\phi,$$

in which we substitute the intertwining operator relation (3.10) and the spatial reflection symmetry (3.29). We then obtain

$$\tilde{\mathbf{S}}\psi = \pm\frac{1}{A}\mathbf{U}\phi = \pm\psi$$

We should emphasize that the sign in (3.30) related to the evenness or oddness of the chrono is necessarily the same as that of Equation (3.29) determining whether the corresponding topo belongs to $\mathcal{H}^+$ or to $\mathcal{H}^-$. This phenomenon is a consequence of the isomorphism between space and time and the existence of a space-time symmetry. This point confirms that the BOD connected to the concept of space-time symmetry is an extremely powerful tool which permits to deduce spatial information from temporal modes, and vice versa temporal information from spatial modes. For instance, in the case of the spatio-temporal $Z_2$ symmetry described above, we can detect the evenness or oddness of the chronos by checking the symmetry of the corresponding topos.

## 3.3 Appearance of Spatio-temporal Symmetries through the Primary Instability

An example of these space-time symmetries is furnished by a wake flow behind a half-cylinder (see the sketch in Figure 1.1) which we now present, although this equally applies to a wake behind a full cylinder. In the following, the norms defining the Hilbert spaces $H(X)$ and $H(T)$ are simply chosen as the $L^2$-norms. Via a two-dimensional biorthogonal decomposition, we now analyze the flow which was originally computed by Karniadakis and Tomboulides (1992(a)) who numerically integrated the two-dimensional Navier-Stokes equations. At Reynolds number $Re = 100$, a coupling of the eigenvalues can clearly been observed in the spectrum (see Figure 3.1(a)) (except for the first term of the decomposition which corresponds to the temporal mean of the flow) which indicates the presence of a space-time symmetry (3.4). Topos and chronos present a certain coupling (see Figure 3.2 and Figure 3.3) which can be clearly identified as translation symmetries of the type of (3.16), although due to the wake attenuation downstream the amplitude of the topos decays with $x_1$. Another feature of the chronos and topos shows that a non-instantaneous determin-

istic reflection symmetry of the type (3.29) associated with (3.28) is present. The components of the topos are either odd or even as shown in Figures 3.4 and 3.5, while the chronos have the property of being either invariant or opposite under a shift of a half-period (see Figure 3.3) (see our discussions in the previous section).

## 3.4 Breaking of the Previous Space-time Symmetries: A First Step Toward 'Complexity'

It is then fundamental to investigate the breaking of such symmetries as Reynolds number increases and the flow becomes more and more complex, to eventually reach a turbulent state. From this viewpoint, it is interesting to note that if a space-time symmetry represented by the equation (3.10) and (3.11) is satisfied, then the spatial two-point correlation operator $\mathbf{U^*U}$ is invariant under the spatial component of the symmetry S, i.e.

$$SU^*U = U^*US$$

and the temporal two-point correlation operator $\mathbf{UU^*}$ is invariant under the temporal component of the symmetry, $\tilde{\mathbf{S}}$, i.e.

$$\tilde{\mathbf{S}}UU^* = UU^*\tilde{\mathbf{S}}.$$

As the flow becomes more complex, the spatial two-point correlation still satisfies the (spatial) symmetry, namely the flow enjoys a 'statistical symmetry'. However, because $U$ realizes an isomorphism between the spatial space $H(X)$ and the temporal space $H(T)$, there exists a temporal symmetry $\tilde{\mathbf{S}}$ but the latter may be different from those characteristics of a Karman street (see above). For example, the spatial translation symmetry is still present, manifesting itself by the homogeneity property of the flow but the traveling wave disappears, indicating that the temporal symmetry is no longer a translation as in (3.18). Similarly, the flow is statistically invariant under

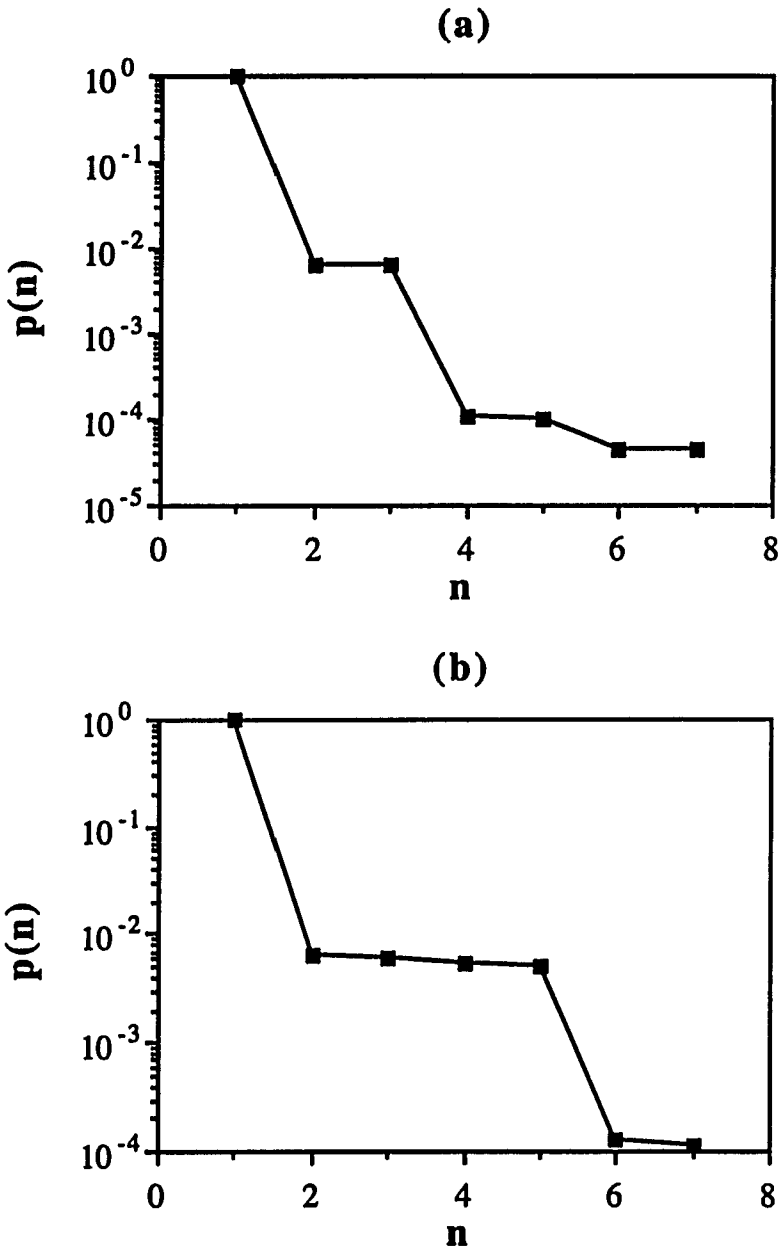


Figure 3.1: BOD analysis of numerical data of a flow past a half cylinder. Normalized energy spectrum $p_n = \lambda_n / \sum_k \lambda_k$ with $\lambda_n = A_n^2$. (a) $Re = 100$; (b) $Re = 200$.

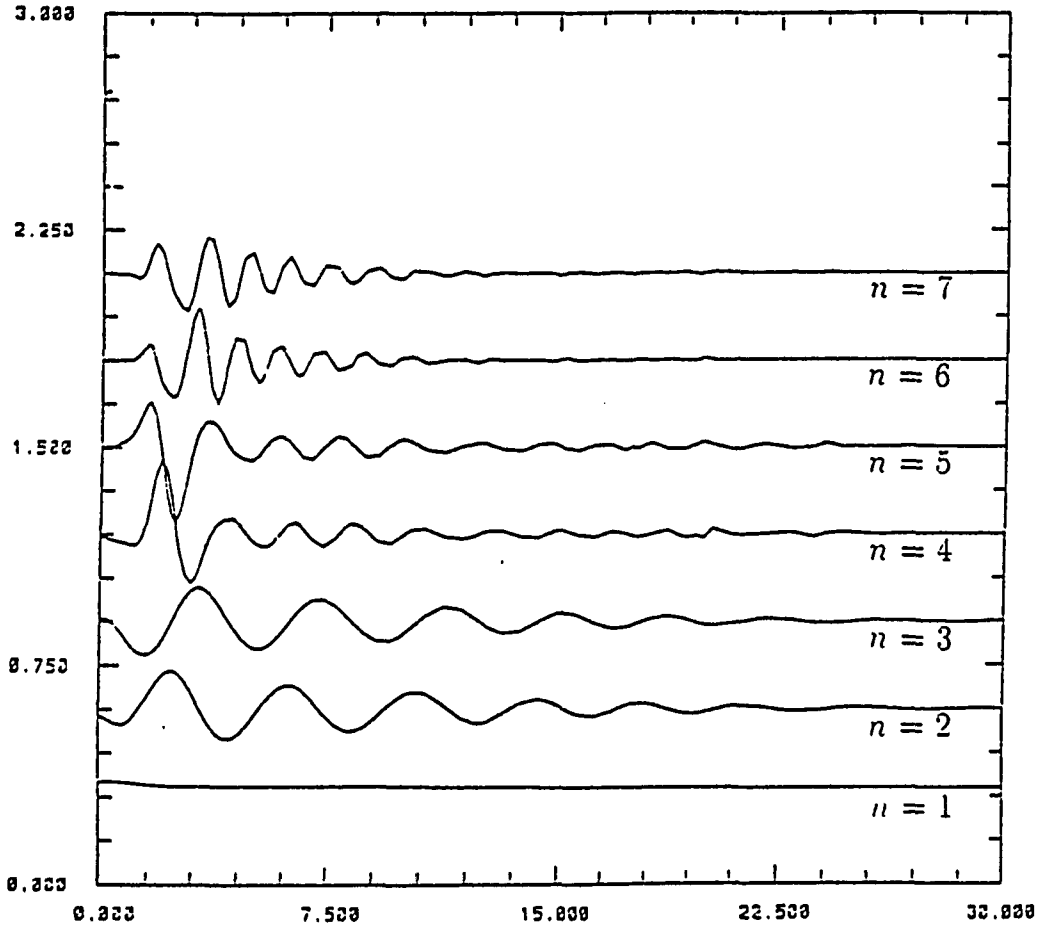


Figure 3.2: BOD analysis of numerical data of a flow past a half cylinder. The $x_1$-component of the topo $\phi_1^{(n)}$ (n appears below the corresponding curve) at $x_2 = 1.0$ as a function of $x_1$, $Re = 100$.

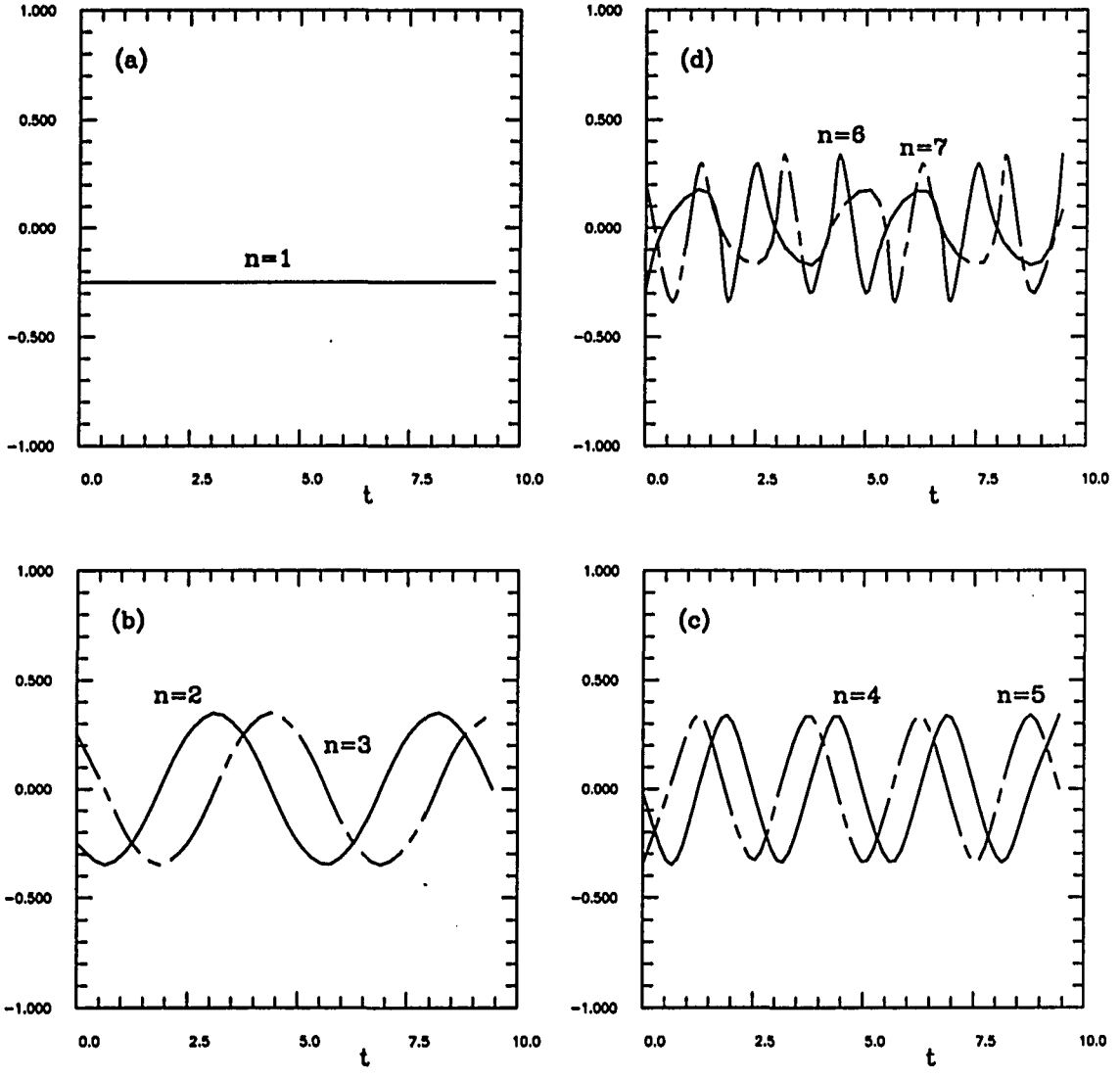


Figure 3.3: BOD analysis of numerical data of a flow past a half cylinder. Chrono $\psi^{(n)}(t)$ at Reynolds number $Re = 100$. (a) $n = 1$; (b) $n = 2, 3$; (c) $n = 4, 5$; (d) $n = 6, 7$.

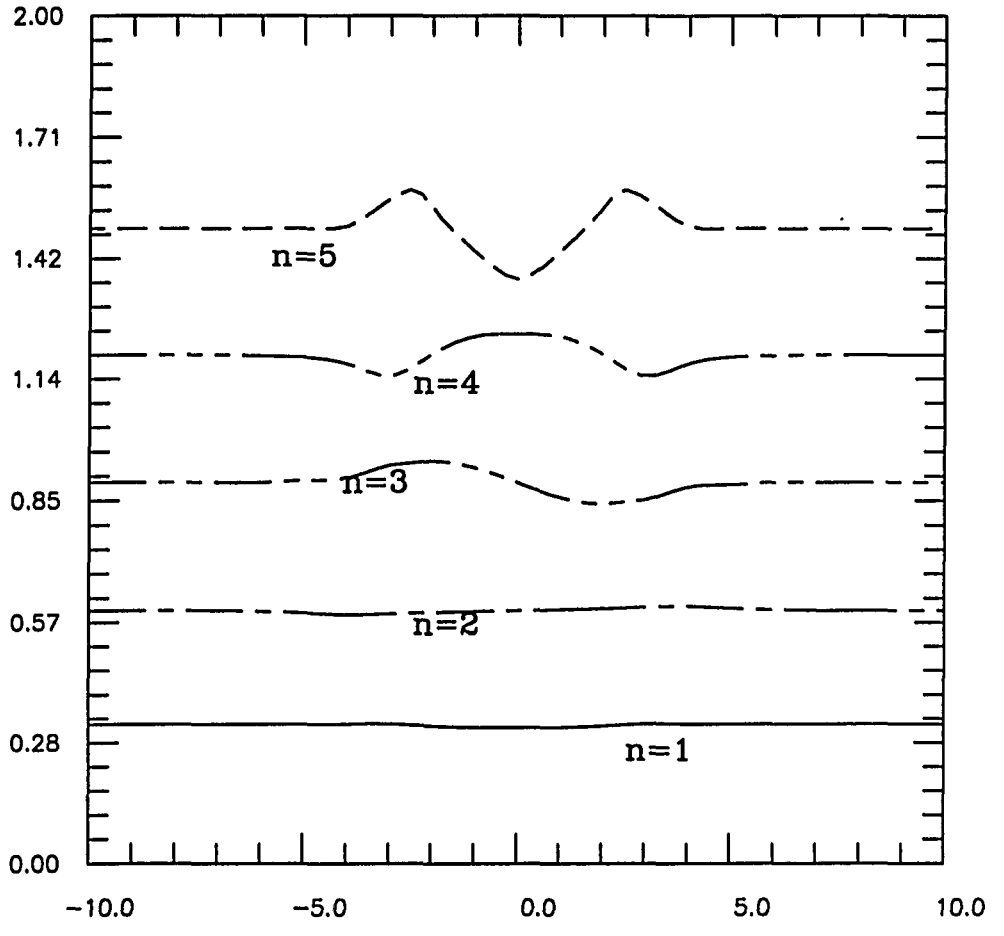


Figure 3.4: BOD analysis of numerical data of a flow past a half cylinder. The $x_1$-component of the topo $\phi_1^{(n)}$ at $x_1 = 7.0$ as a function of normal position $x_2$ at Reynolds number $Re = 100$.

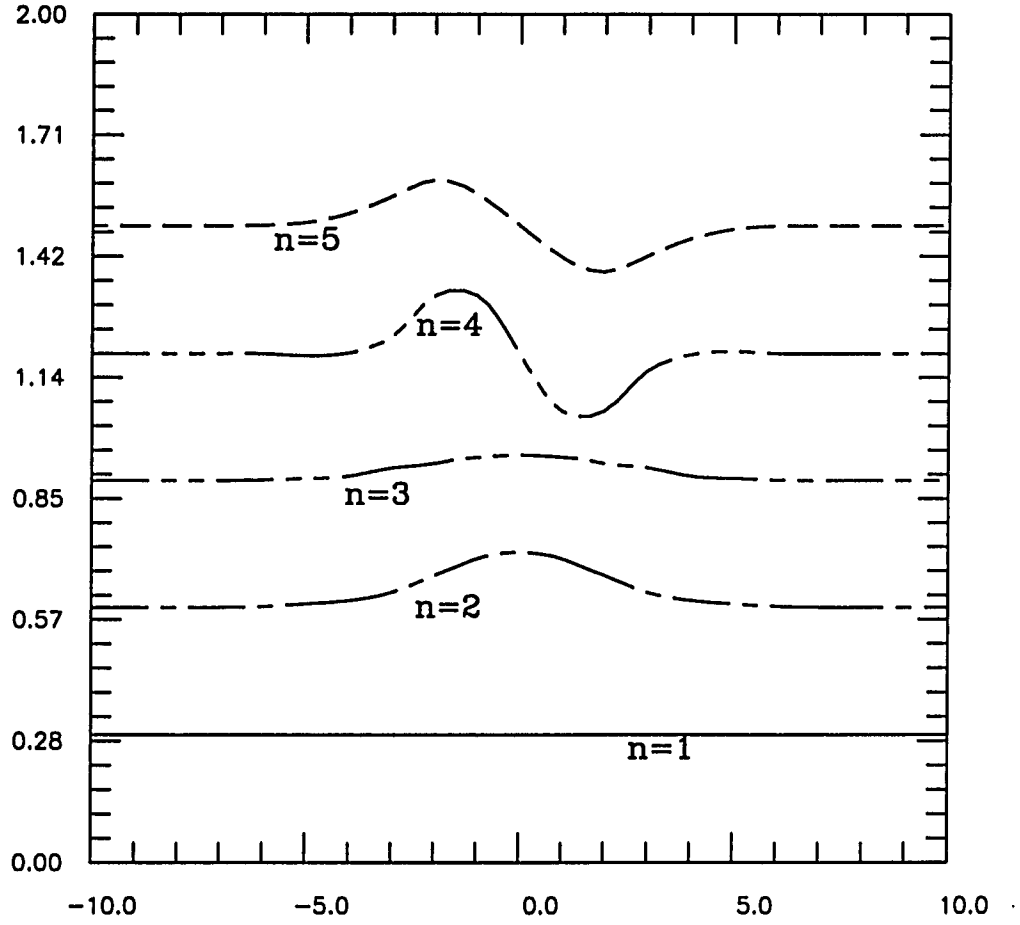


Figure 3.5: BOD analysis of numerical data of a flow past a half cylinder. The $x_2$-component of the topo $\phi_2^{(n)}$ at $x_1 = 7.0$ as a function of normal position $x_2$ at Reynolds number $Re = 100$.

reflection about its mid-plane but again, the corresponding temporal component of the symmetry is no longer a shift by a half-period.

Examples of this symmetry breaking can also be identified in the wake flow behind a half-cylinder at Reynolds number $Re = 200$. Figure 3.1(b) shows the spectrum in which we can notice an eigenvalue coupling, although the latter is not as perfect as for that obtained at $Re = 100$ (actually, modes 2-5 appear to have a fourth order (rather than second order) quasi-degeneracy). This indicates a slight symmetry breaking, which can be more clearly observed from the chronos and topos. Coupled chronos display an amplitude variation added to the translation symmetry as shown in Figure 3.6. Coupled topos show a local violation of the translation symmetry (Figure 3.7), which is most visible between the second and third ones in the first part of the spatial domain (upstream). Another interesting point is the deformation of the topos with respect to Fourier modes which keep the same frequency through the whole domain. Here, the oscillating period doubles at approximately one third of the domain, indicating a vortex merging which also can be observed in Figure 3.8 displaying a velocity component in the space ($x_1$) - time domain. Here, the breaking of the space-time translation symmetry is due to a local dynamical event. Recall, that such merging could be observed neither experimentally (Brown, 1992) nor numerically in three-dimensional calculations (Karniadakis and Tomboulides, 1992(a)). However, it seems to be the solution of the two-dimensional problem as checked by Karniadakis and Tomboulides (1992(a)) who increased the computational resolution. Anyhow, it is an interesting phenomenon from our viewpoint since it offers a scenario for a space-time translation symmetry breaking and thus opens a route to more complex states.

In the temporal domain considered here, i.e. one vortex shedding period, the space-time reflection symmetry is also broken due to the fact that vortex merging occurs either in the upper or lower part of the wake. This can be seen through the

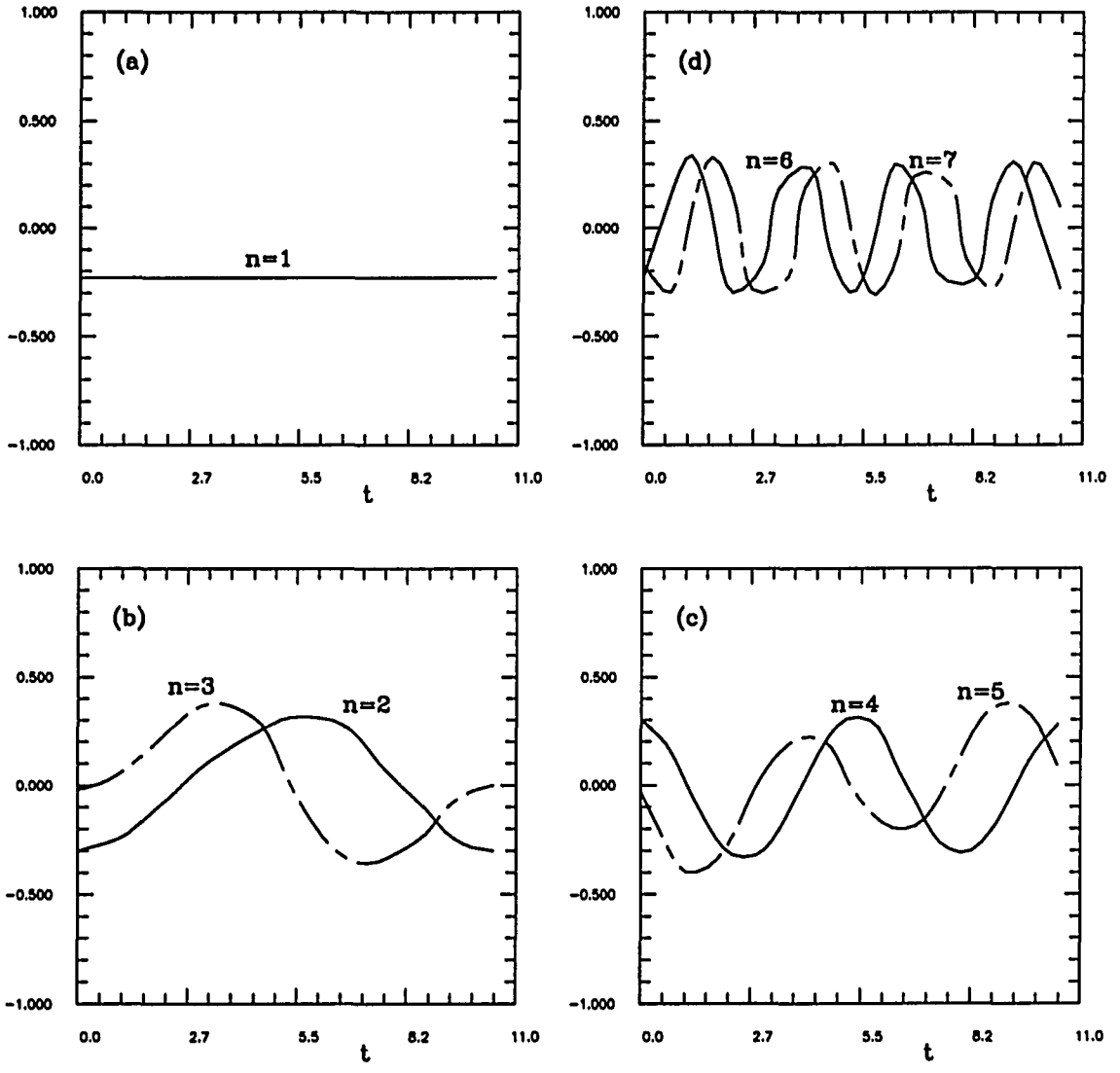


Figure 3.6: BOD analysis of numerical data of a flow past a half cylinder. Chrono $\psi^{(n)}(t)$ at $Re = 200$: (a) $n = 1$; (b) $n = 2, 3$; (c) $n = 4, 5$; (d) $n = 6, 7$.

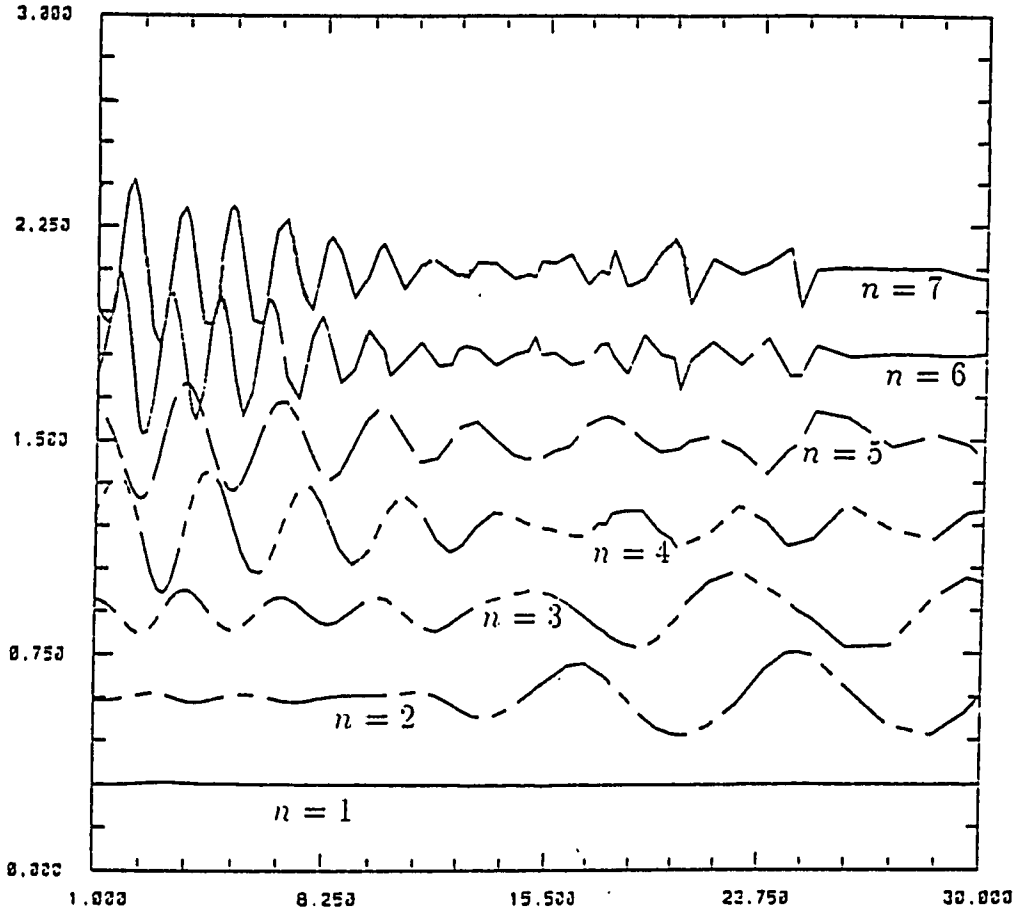


Figure 3.7: BOD analysis of numerical data of a flow past a half cylinder. The $x_1$-component of topo $\phi_1^{(n)}$ at the normal location $x_2 = 1.0$ as a function of streamwise variable $x_1$, Reynolds number is $Re = 200$.

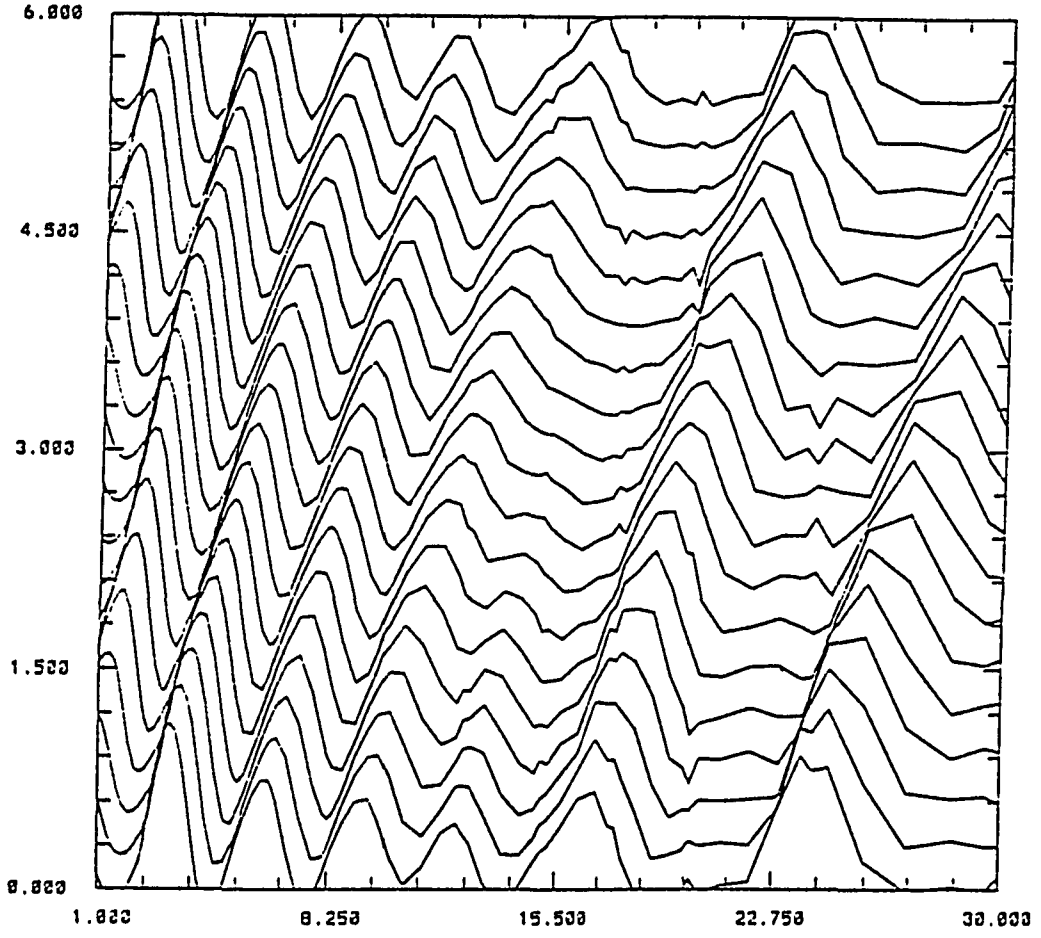


Figure 3.8: BOD analysis of numerical data of a flow past a half cylinder. The $x_1$-component of the velocity as a function of $x_1$ at Reynolds number $Re = 200$. Horizontal axis is $x_1$, different curves represent the velocity at successive times, time increases from bottom to top.

chronos which no longer satisfy the property given by (3.30). It should be however mentioned that the reflection symmetry should still be valid in the statistical sense, namely the spatial two-point correlations, in an appropriate temporal domain $T$, should still be invariant. This is probably true if one considers a much longer time including the vortex merging in both the upper and the lower parts of the wake. In this case, the flow is still periodic but the period $T$ is now much longer and the space-time reflection symmetry should still be valid when the period involved in the temporal part of the symmetry (3.28) is precisely $T$. Note the important role of the reflection symmetry which introduces this additional frequency in the system. Without this constraint, we would only observe a local period doubling.

## 3.5 Space-time Symmetries of Turbulent Wake Flows

According to the previous remarks, turbulent flows which satisfy 'statistical' spatial symmetries should also be invariant under selected deterministic space-time symmetries, as we discussed earlier. Symmetries may then not be as simple as those introduced earlier. In order to analyze these symmetries, a more generalized spatio-temporal theory is needed. In this section, we present the analysis of turbulent space-time symmetries which follows a brief review of the theoretical arguments developed by Aubry et al. (1992(a)) and Cáo and Aubry (1992).

### 3.5.1 Dilation Symmetries of the Navier-Stokes Equations and Biorthogonal Decomposition

In order to generalize the concept of space-time symmetries (3.4) and make it applicable to the turbulent complexity, it is useful to generalize the operator inter-

wining relation

$$\mathbf{US} = \tilde{\mathbf{S}}\mathbf{U}$$

$$\mathbf{US}^* = \tilde{\mathbf{S}}^*\mathbf{U}$$

and introduce the operator relation

$$\mathbf{US} = \gamma\tilde{\mathbf{S}}\mathbf{U}$$

$$\mathbf{US}^* = \gamma^{-1}\tilde{\mathbf{S}}^*\mathbf{U}$$

(where $\gamma$ is a real number, strictly smaller than 1), in which case the corresponding part of the spectrum decreases exponentially fast with $n$, namely

$$A_{n+1} = \gamma A_n$$

and the associated spatial and temporal modes can all be deduced from one by the relation $\phi_{n+1} = S\phi_n$ and $\psi_{n+1} = \tilde{S}\psi_n$. Using such notion together with the space-time invariance

$$\mathbf{x} \rightarrow \lambda\mathbf{x}$$

$$t \rightarrow \lambda^{1-h}t$$

$$\mathbf{u} \rightarrow \lambda^h\mathbf{u}$$

of the Navier-Stokes equations

$$\frac{\partial \mathbf{u}}{\partial t} + (\mathbf{u}\cdot\nabla)\mathbf{u} = -\nabla p + \frac{1}{Re}\nabla^2\mathbf{u}$$

$$\nabla\cdot\mathbf{u} = 0,$$

and assuming that the flow itself is invariant under sush symmetries, namely

$$\tilde{\mathbf{S}}_\lambda\mathbf{U} = \lambda^{-h}\mathbf{U}\mathbf{S}_\lambda, \tag{3.32}$$

we obtain scaling laws for both the spectrum and the basis modes and the spectrum

$$(\mathbf{S}_\lambda\phi)(x) = \phi(\lambda^{-1}x),$$

$$(\tilde{\mathbf{S}}_\lambda \psi)(x) = \psi(\lambda^{-(1-h)} t),$$

$$A_{n+1}^2 = \lambda^{-2h} A_n^2. \tag{3.33}$$

It is interesting to note that (3.32) implies that the spatial correlation operator, $\mathbf{U}^*\mathbf{U}$, and the temporal one, $\mathbf{U}\mathbf{U}^*$ satisfy the relation

$$\mathbf{S}_\lambda^{-1} \mathbf{U}^* \mathbf{U} \mathbf{S}_\lambda = \lambda^{2h} \mathbf{U}^* \mathbf{U} \tag{3.34}$$

and

$$\tilde{\mathbf{S}}_\lambda^{-1} \mathbf{U}^* \mathbf{U} \tilde{\mathbf{S}}_\lambda = \lambda^{2h} \mathbf{U}^* \mathbf{U}, \tag{3.35}$$

so that if the scale transformation is assumed in a statistical sense, namely it is satisfied only by the spatial two-point correlation, i.e. (3.34) is valid, but this is not the case of (3.35), the spectrum law is unchanged and there still exists a temporal symmetry $\tilde{\mathbf{S}}$ such that the commutation relations (3.32) and (3.35) hold if $\tilde{\mathbf{S}}_\lambda$ is replaced by $\tilde{\mathbf{S}}$.

These theoretical findings (see Aubry et al., 1992(b) and Lian and Aubry , 1993 for more details) should have tremendous consequences on our ability to compute turbulent, inhomogeneous flows through simplified equations derived from the Navier-Stokes equations in which the velocity is expanded into such renormalized modes. It should be, however, mentioned that the influence of finite boundary conditions, finite discretizations as well as the fact that either the symmetry center is located at infinity (as probably in wake flows) or its location is unknown may introduce difficulties in an investigation of this kind of symmetries from realistic data. Moreover, such instantaneous data in a three-dimensional spatial domain are not available in turbulence, neither from experiments nor from numerical simulations. The most complete accessible measurements are those of the correlation tensor measured under various assumptions as we describe in the next paragraph and in more detail in Chapter 4.

### 3.5.2 Analysis for Turbulent Wake Flow behind a Circular Cylinder

In order to illustrate the space-time symmetries of turbulent flows analyzed in the previous paragraph, we now investigate a turbulent wake flow behind a circular cylinder at a Reynolds number $Re = 5000$ (this investigation will be described in Chapter 4). To decompose the three-dimensional velocity field, we consider the operator such that

$$(\mathbf{U}\phi)(t) = \int \sum_{i=1}^{3} u_i(\mathbf{x},t)\phi_i(\mathbf{x})d\mathbf{x}$$

so that the kernel of $\mathbf{U}^*\mathbf{U}$ is the two-point correlation

$$\int_T u_i(\mathbf{x},t)u_j(\mathbf{y},t)dt \qquad\qquad (i,j=1,2,3)$$

The nine components of the correlation matrix were measured by Guezennec and Gieseke (1991) (see Section 3.1 for details).

A classical POD technique, decomposing the correlations thus measured, into Fourier modes $\exp(ilx_1), \exp(ikx_3)$ in the streamwise ($x_1$) and spanwise ($x_3$) directions and POD modes in the inhomogeneous direction ($x_2$)

$$\begin{aligned} R_{ij}(x_1-x_1', x_2, x_2', x_3-x_3') &= < u_i(x_1,x_2,x_3,t)u_j(x_1',x_2',x_3',t) > \\ &= \sum_n \sum_{l,k} [A^{(l,k,n)}]^2 \phi_i^{(l,k,n)}(x_2)\phi_j^{(l,k,n)}(x_2') \end{aligned} \qquad (3.36)$$

(where <> denotes the temporal average) was used to determine statistically relevant spatial modes $\phi_i^{(l,k,n)}(x_2)$ and energy spectra

$$\lambda^{(l,k,n)} = [A^{(l,k,n)}]^2.$$

We refer to Section 4.2 for a detailed description of the procedure.

Although too many assumptions were made to enable a complete identification with the deterministic biorthogonal decomposition which requires *simultaneous* measurements at all spatial points, a rough comparison, based on the stationarity

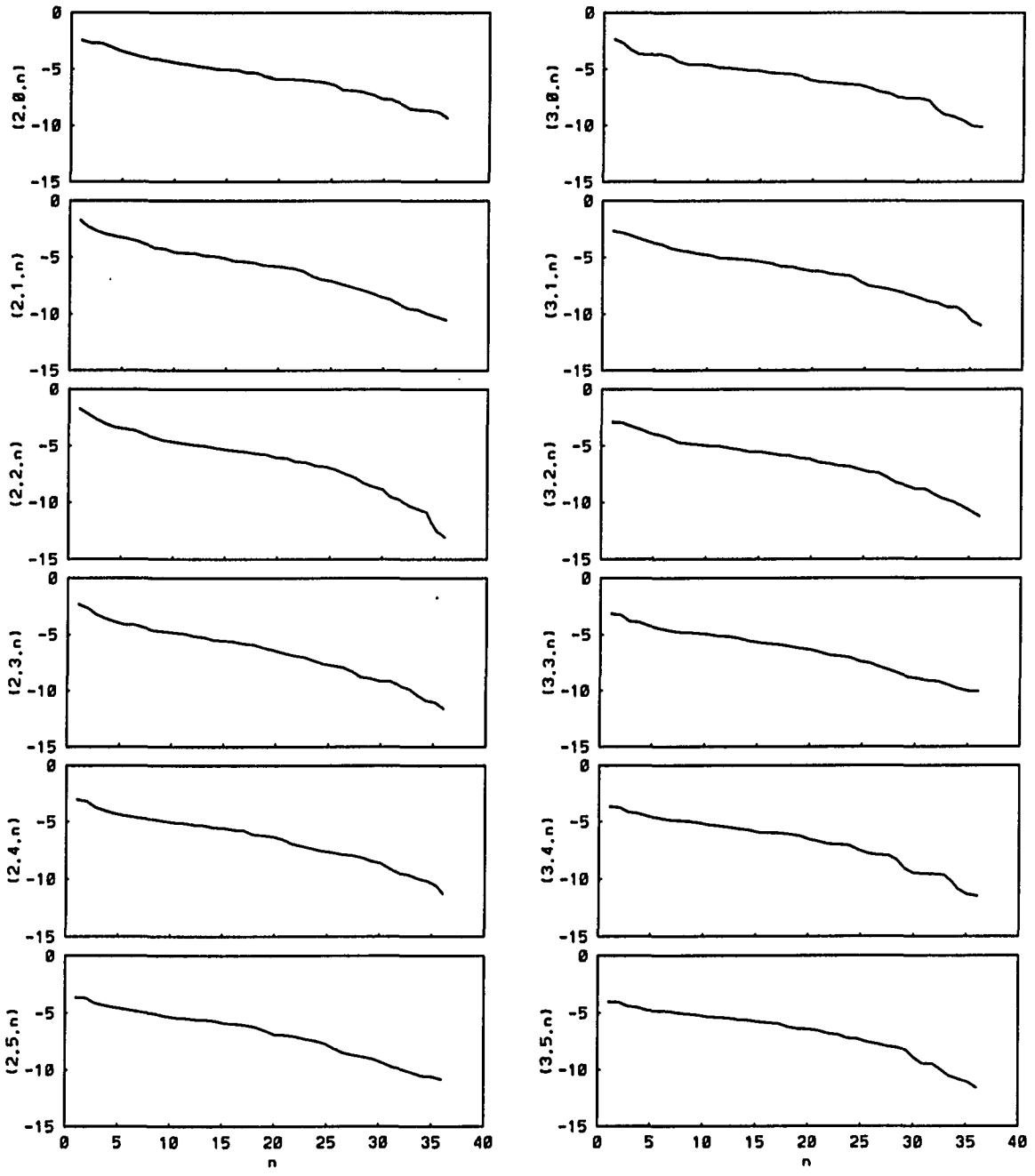


Figure 3.9: POD analysis of the experimental data in a turbulent far wake flow. Energy spectrum $\ln \lambda^{(lkn)}$ as a function of the POD index $n$ at a fixed Fourier wavenumber $(l, k)$.

assumption, seems reasonable. Then, spectra should display an exponential decay, which they do approximately for each pair of Fourier modes (Figure 3.9). As expected, the self-similarity is broken for the very first modes (especially at low Fourier wavenumbers), due to the effect of boundary conditions and at the viscous end of the spectra (especially at high Fourier wavenumbers).

At this point, it is however, difficult to draw any conclusions regarding the three-dimensional structure of the symmetry which needs further investigations relaxing, in particular, the streamwise and spanwise homogeneity assumptions. In order to avoid this difficulty, we now concentrate on the structure of the flow in the inhomogeneous direction. For this purpose, we consider the two-point correlations at $x_1 = x_1'$ and $x_3 = x_3'$, namely $R_{ij}(0, x_2, x_2', 0)$, so that (3.36) becomes

$$R_{ij}(0, x_2, x_2', 0) = \sum_n \lambda^{(n)} \phi_i^{(n)}(x_2) \phi_j^{(n)}(x_2') \tag{3.37}$$

The spectrum, displayed in Figure 3.10 shows a tendency to decay exponentially fast. This tendency, however, is hidden by the presence of other symmetries, which are here the statistical reflection symmetry in the $x_2$ and $x_3$-directions. On the one hand, we have seen that the $x_2$-reflection symmetry splits the space of spatial functions into two orthogonal subspaces, one spanned by eigenvectors in $\mathcal{H}^+$, the other one spanned by eigenvectors in $\mathcal{H}^-$ (see our discussion in Section 3.2), both being invariant under the dilation symmetry. On the other hand, the reflection (statistical) symmetry in the $x_3$-direction makes the two-point correlation necessarily satisfy the following relation

$$R_{ij}(x_1, x_2, x_2', -x_3) = R_{ij}(x_1, x_2, x_2', x_3)\delta_i\delta_j$$

where

$$\delta_i = \begin{cases} -1 & \text{if } i = 3 \\ 1 & \text{if } i = 1, 2. \end{cases}$$

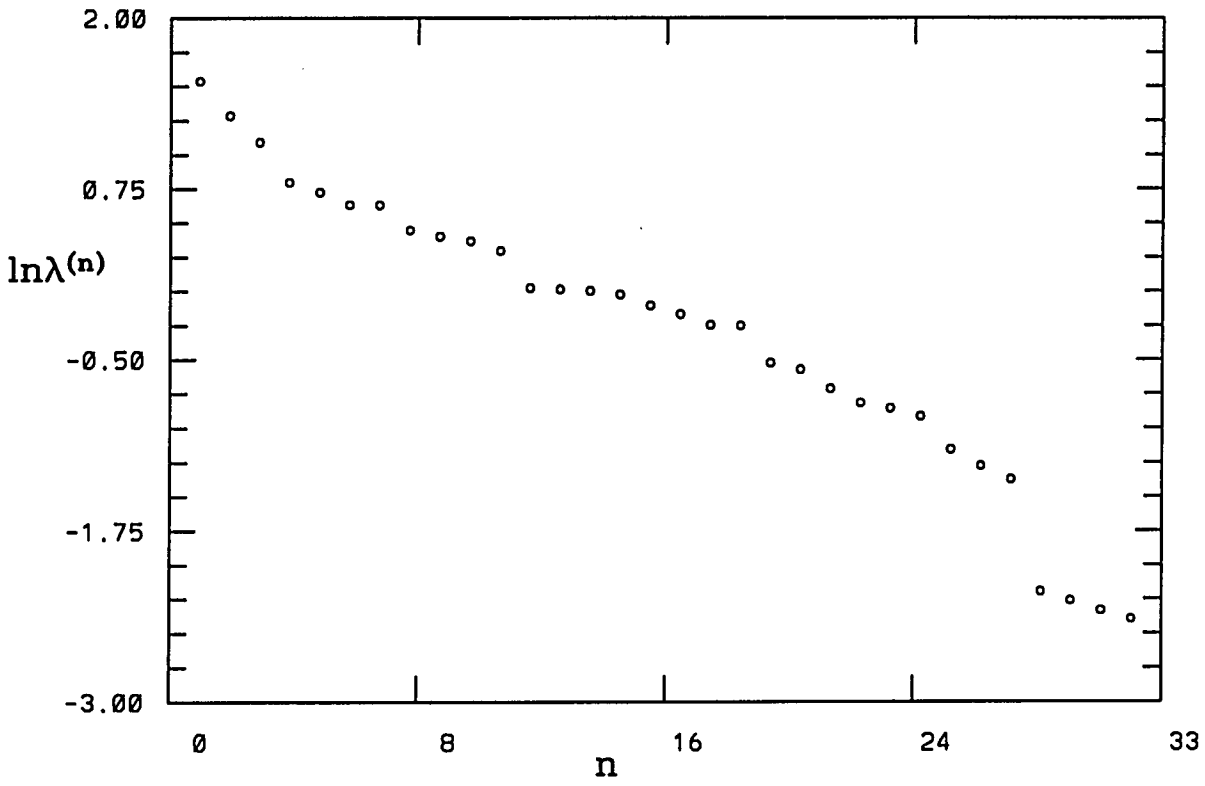


Figure 3.10: POD analysis of the experimental data in a turbulent far wake flow. One-dimensional spectrum $\lambda^{(n)}$ on a logarithmic scale versus the mode index $n$.

In particular, on the $x_2$-axis ($x_1 = x_3 = 0$) (to which we restrict the present analysis), we get a correlation of the form

$$\mathbf{R} = (R_{ij}) = \begin{pmatrix} R_{11} & R_{12} & 0 \\ R_{21} & R_{22} & 0 \\ 0 & 0 & R_{33} \end{pmatrix}.$$

The eigenvalue problem of the biorthogonal decomposition is therefore decoupled into two independent sub-problems, one whose spatial part is governed by

$$\int \begin{pmatrix} R_{11} & R_{12} \\ R_{21} & R_{22} \end{pmatrix} (x_2, x_2') \begin{pmatrix} \phi_1 \\ \phi_2 \end{pmatrix} (x_2') dx_2' = \lambda \begin{pmatrix} \phi_1 \\ \phi_2 \end{pmatrix} (x_2),$$

the other one whose spatial part becomes

$$\int R_{33}(x_2, x_2') \phi_3(x_2') dx_2' = \lambda \phi_3(x_2).$$

Since these two eigenvalue problems are independent, the resulting eigenfunctions $\phi$ have zero third component

$$\phi = \begin{pmatrix} \phi_1 \\ \phi_2 \\ 0 \end{pmatrix}$$

or zero first and second components

$$\phi = \begin{pmatrix} 0 \\ 0 \\ \phi_3 \end{pmatrix}.$$

This additional symmetry has the effect of accumulating the eigenvalues by packets in the spectrum. A simple observation of the form of the modes permits the identification and extraction of subgroups of self-similar modes. Modes inside the same subgroup, denoted as $\phi^{(n_l)}$, $l = 1, 2, ...$, show self-similar features and their corresponding spectra decay exponentially fast, as illustrated in Figure 3.11, 3.12,

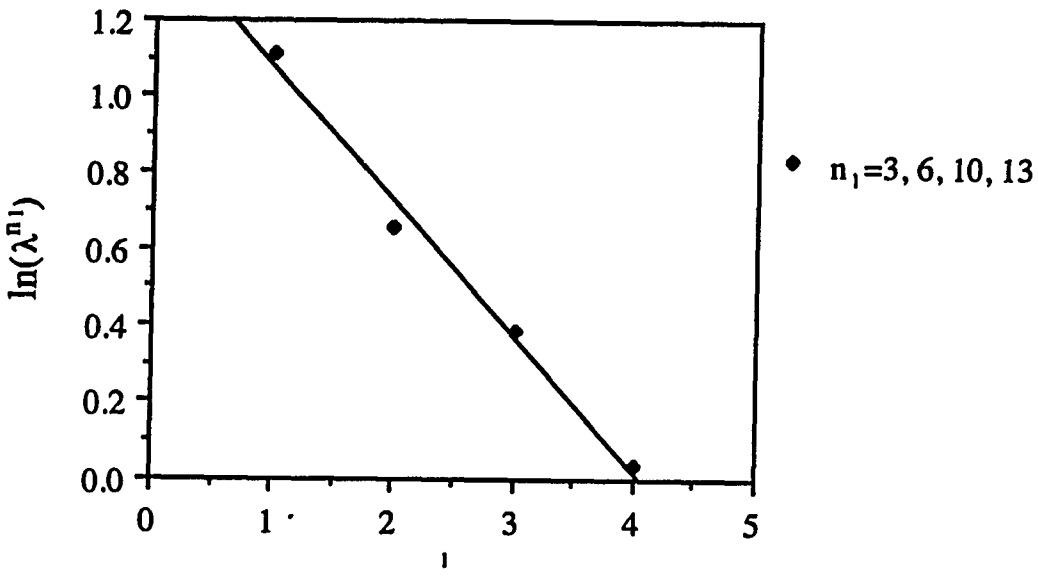


Figure 3.11: POD analysis of the experimental data in a turbulent far wake flow. Spectrum $\lambda^{(n)}$ of a series of self-similar modes ($n_l = 3, 6, 10, 13$).

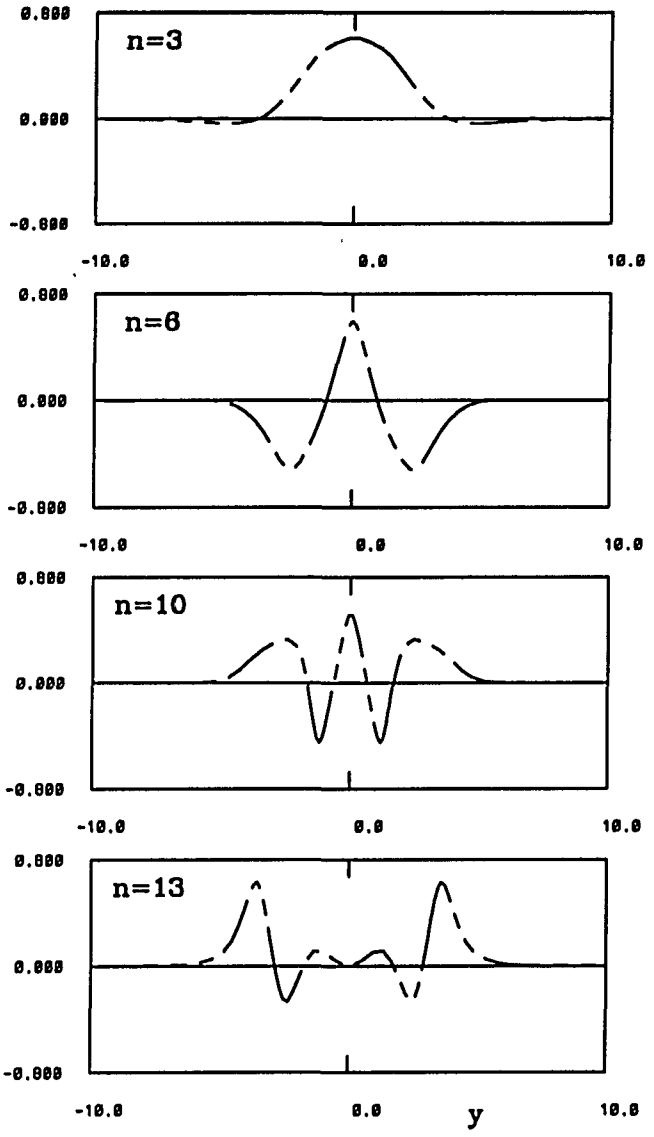


Figure 3.12: POD analysis of the experimental data in a turbulent far wake flow. Series of self-similar modes $\phi_i^{(n_l)}$, $-$ $i = 1$, $-\cdot-$ $i = 2$, $-\cdot\cdot-$ $i = 3$ ($n_l = 3, 6, 10, 13$) whose spectrum is displayed in Figure 3.11.

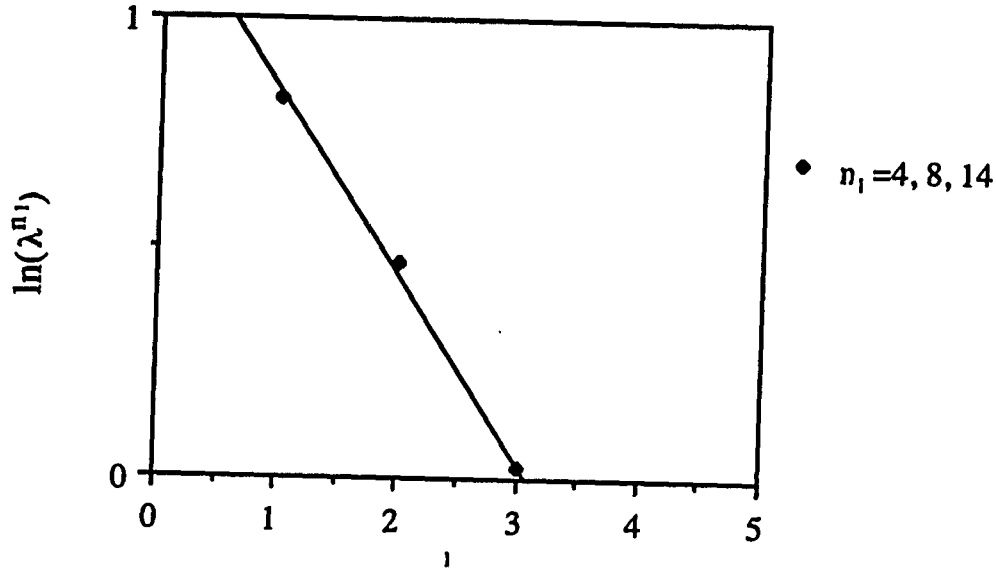


Figure 3.13: POD analysis of the experimental data in a turbulent far wake flow. Spectrum $\lambda^{(n)}$ of a series of self-similar modes ($n_l = 4, 8, 14$).

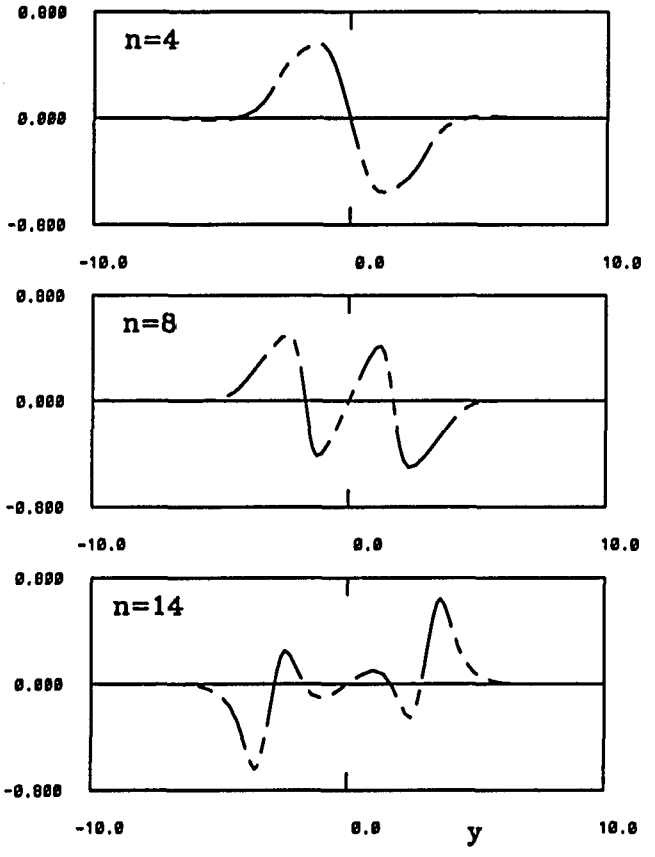


Figure 3.14: POD analysis of the experimental data in a turbulent far wake flow. Series of self-similar modes $\phi_i^{(n_l)}$, $-$ $i = 1$, $- \cdot -$ $i = 2$, $- \cdot \cdot -$ $i = 3$ ($n_l = 4, 8, 14$) whose spectrum is displayed in Figure 3.13.

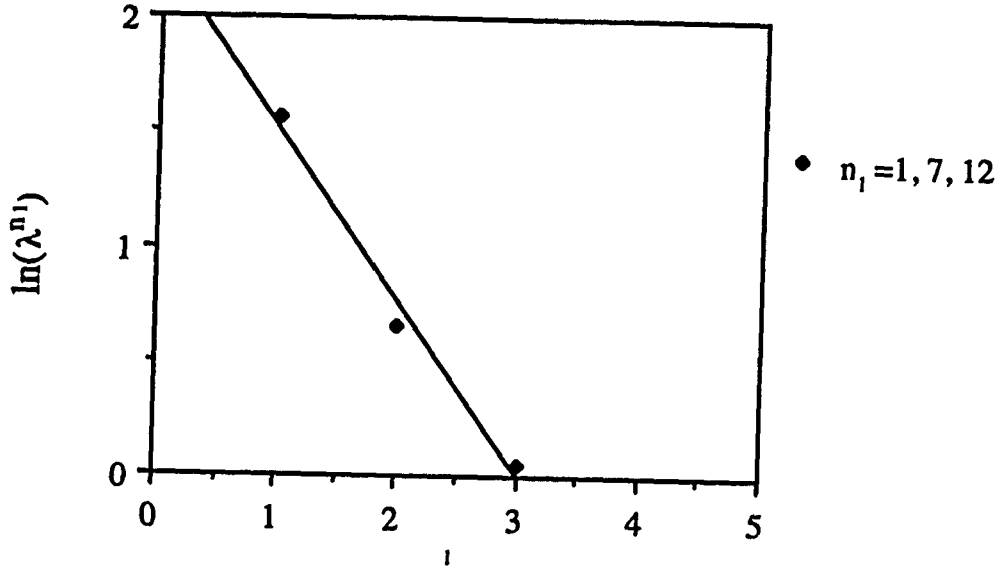


Figure 3.15: POD analysis of the experimental data in a turbulent far wake flow. Spectrum $\lambda^{(n)}$ of a series of self-similar modes ($n_l = 1, 7, 12$).

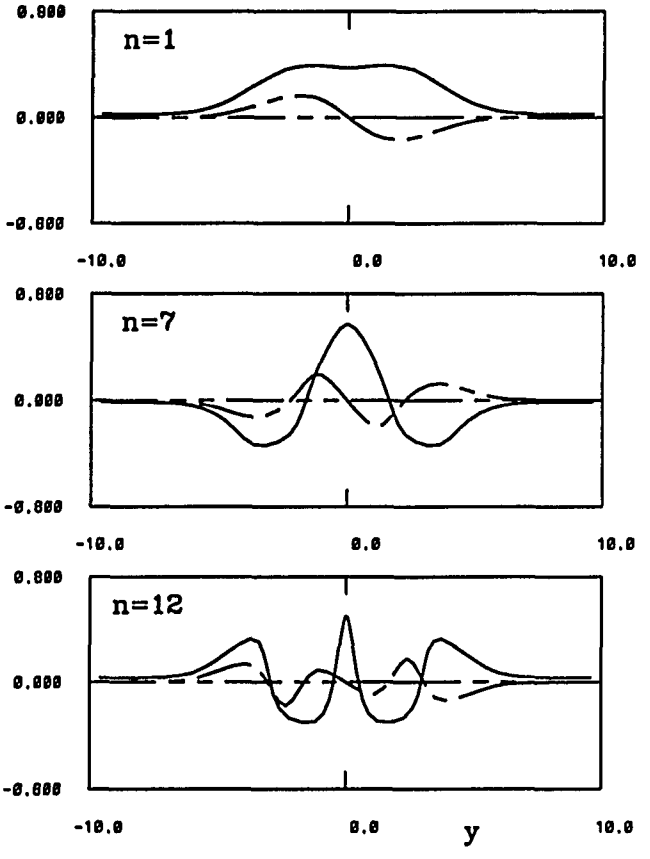


Figure 3.16: POD analysis of the experimental data in a turbulent far wake flow. Series of self-similar modes $\phi_i^{(n_l)}$, $-$ $i = 1$, $-\cdot-$ $i = 2$, $-\cdot\cdot-$ $i = 3$ ($n_l = 1, 7, 12$) whose spectrum is displayed in Figure 3.15.

3.13, 3.14, 3.15 and 3.16. Therefore, all (spatial) modes within a subgroup can be deduced from one by dilation symmetry. (The restriction to a few modes within each group is obviously due to the limited spatial resolution imposed by experimental constraints). We then know that there exists a corresponding temporal symmetry for which, however, we cannot get any insight from the previous experimental data.

## 3.6 A Low Dimensional Dynamical System

The unsteady velocity field, as a spatio-temporal vectorial function, can be reconstructed by the summation of all spatial and temporal BOD modes (topos and chronos), assuming that the latter are known. On the one hand, once the topos (resp. topos) are known, we can determine the chronos (resp. topos) by using the one-to-one (dispersion) relation (3.3). On the other hand, the chronos can be considered as the normalized time coefficients of the decomposition of the operator $\mathbf{U}^*\mathbf{U}$ whose kernel is the spatial two-point correlation, which can be recovered from a Galerkin projection of the Navier-Stokes equations and the appropriate boundary conditions onto the set of topos. The dimension of such dynamical system should obviously include all non-zero terms in (3.36). However, a dynamical system of lower dimension, as the result of a more severe truncation, may also be worth investigating since the POD converges optimally fast in the sense of the $L^2$-norm (kinetic energy) and if the influence of the smaller energy terms onto the resolved scales are represented, namely modeled. Note that the deterministic BOD and its properties in turbulent flows (see Section 3.5) may allow to do this in a rational manner. Then, a low dimensional dynamical system derived through the above procedure is expected to recover the basic dynamics of the original flow system, as it is indeed the case for a turbulent wake flow (see Chapter 4). Furthermore, this strategy, when the obtained results are compared with those of direct numerical simulations, provides a quantitative analysis of the influence of a BOD truncation. In this section we construct a low dimensional dynamical system for

wake flow past a half cylinder which successfully reproduces the flow pattern obtained by direct numerical simulation.

### 3.6.1 The Derivation of Ordinary Differential Equations

The flow past a half cylinder (see the sketch of the flow in Figure 1.1) is governed by the incompressible Navier-Stokes equations

$$\frac{\partial \mathbf{u}}{\partial t} + (\mathbf{u} \cdot \nabla)\mathbf{u} = -\nabla p + \frac{1}{Re}\nabla^2 \mathbf{u} \tag{3.38}$$

$$\nabla \cdot \mathbf{u} = 0 \tag{3.39}$$

and the boundary conditions

$$\mathbf{u} = \mathbf{U}_\infty \qquad \text{on AB, BC and AD} \tag{3.40}$$

$$\frac{\partial \mathbf{u}}{\partial n} = 0 \qquad \text{on DC} \tag{3.41}$$

$$\mathbf{u} = 0 \qquad \text{on the body} \tag{3.42}$$

where the reader should refer to Figure 1.1 for the meaning of the boundaries AB, BC, AD and DC. By substituting (3.9) into (3.38) and (3.39), we get

$$\sum_{i=1}^{N} \frac{d\psi_i}{dt}\phi_i + \sum_{n=1}^{N} \psi_i \psi_n \phi_i \cdot \nabla \phi_n - \frac{1}{Re}\psi_i \nabla^2 \phi_i = -\nabla p \tag{3.43}$$

$$\nabla \cdot \phi_i = 0. \tag{3.44}$$

We then apply a Galerkin projection of the above equations onto the topos and derive the following ordinary differential equations

$$\frac{d\psi_j}{dt} = \sum_{i,n=1}^{N} a_{ijn}\psi_i \psi_n + \frac{1}{Re}\sum_{i}^{N} b_{ij} + c_j \tag{3.45}$$

where

$$a_{ijn} = -\int_\Omega (\phi_i \cdot \nabla \phi_n) \cdot \phi_j d\Omega \left(\frac{A_n A_i}{A_j}\right)^{\frac{1}{2}} \tag{3.46}$$

$$b_{ij} = \int_\Omega (\phi_j) \cdot \nabla^2 \phi_i. \tag{3.47}$$

(3.47) can be further reduced by applying Green's formula

$$b_{ij} = \int_{\partial\Omega} \phi_j \frac{\partial \phi_i}{\partial n} ds - \int_{\Omega} \nabla \phi_j : (\nabla \phi_i)^T d\Omega$$

where $\Omega$ denotes the computational domain and $\partial\Omega$ its boundary. We now consider the first term in the previous formula which is an integral over the boundary of entire computational domain. Due to the boundary conditions (3.41) and (3.42), the part of the integral over DC and the surface of the body is zero, since there we have either $\phi_i = 0$ or $\frac{\partial \phi_i}{\partial n} = 0$. As long as the computational domain is sufficiently large, $\frac{\partial \phi_i}{\partial n} = 0$ on the boundaries AB, BC and CD is a good approximation. Therefore, the first term is zero, and (3.47) reduces to

$$b_{ij} = -\int_{\Omega} \nabla \phi_j : (\nabla \phi_i)^T d\Omega. \tag{3.48}$$

Furthermore, the contribution of the pressure, $c_j$, can be written as

$$c_j = \int_{\Omega} (\phi_j) \cdot \nabla p d\Omega. \tag{3.49}$$

As discussed by Aubry et al.(1988), whether the pressure term needs to be considered or not depends on the computational domain. Indeed, we can rewrite (3.49) in the following form

$$c_j = \int_{\partial\Omega} p \phi_j \cdot \mathbf{n} ds - \int_{\Omega} p \nabla \cdot \phi_j d\Omega$$

in which the second term vanishes due to the incompressibility condition. The first term has a zero contribution if the domain is very large so that the pressure disturbance is zero on the outer boundaries AD, DC, CB and BA, as Deane et al. (1991) considered in a similar system. It should, however, be noted that if the computation domain is not large enough, the contribution of the pressure term can be critical, even if it is small. We will demonstrate numerically below that neglecting such contribution can destabilize the system.

The coefficients $a_{ijn}$ and $b_{ij}$ as well as the forcing term coming from the pressure $c_j(t)$ are computed by a numerical integration based on a spectral element interpolation whose details can be found in Karniadakis and Triantafyllou (1992).

### 3.6.2 Numerical Results

The ordinary differential equations (3.45) previously derived are solved by a sixth order Runge-Kuta method. The coefficients $a_{ijn}$ and $b_{ij}$, and the forcing term from the pressure $c_j(t)$ are computed by implementing the topos extracted from the direct numerical simulation data of the wake flow behind a half cylinder obtained by Karniadakis and Tomboulides (1992(a)) at Reynolds number $Re = 100$. The flow was found to be periodic in time, organized as a Karman vortex street. The data analyzed included ten points uniformly distributed over one temporal period and 6480 spatial points.

Figure 3.17 shows the temporal eigenfunctions, i.e. the chronos, recovered by the low dimensional dynamical system (3.45), in which all the ten BOD modes were retained. Like in the original data, the resulting solution is periodic in time, reproducing a Karman Street. Very good agreement was found between the results of the dynamical system (Figure 3.17) and those computed directly from the BOD of the original data (Figure 3.3). While the non-truncated dynamical system successfully predicts the dynamical behavior of the original flow, we find that any truncated dynamical system fails to do so. This finding reveals that the small energy modes, whose contribution to the spectrum is small (e.g. the tenth mode only contributes $10^{-4}$ to the normalized total energy of fluctuation), play an important dynamical role, as was observed by Aubry et al. (1993) in computed solutions of the Kuramoto-Sivasinsky equation. Although we were not able to reduce the dimension of the dynamical system, this set of ten ordinary differential equations is still much smaller than the original direct numerical simulation of Karniadakis and Tomboulides (1992(a)).

As we mentioned before, the contribution from the pressure term $c_j(t)$ could be very important. Figure 3.18 plots the temporal eigenfunctions, i.e. the chronos, computed by the same dynamical system in which the pressure term $c_j(t)$ is suppressed. We observe that, although the solution still oscillates with approximately

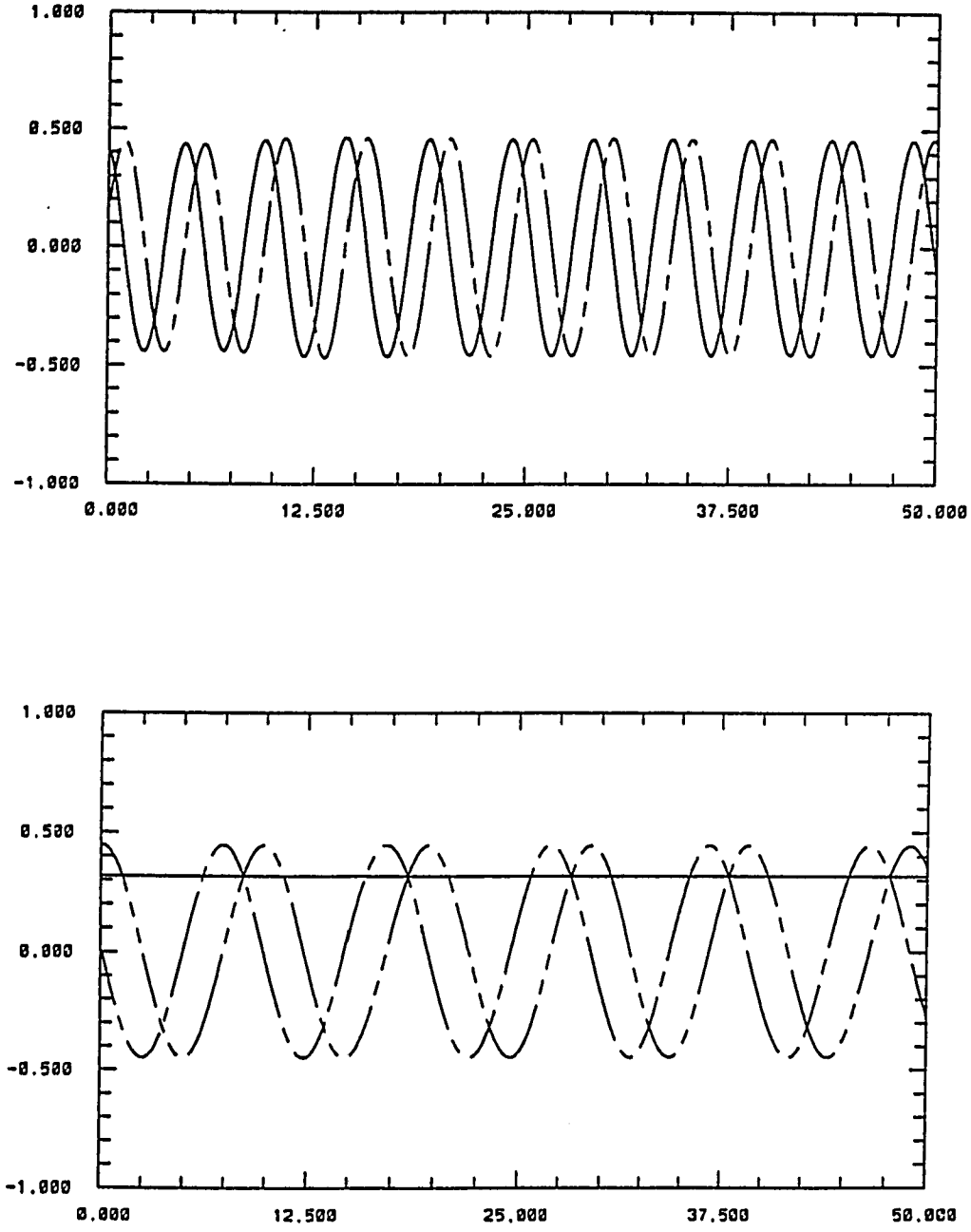


Figure 3.17: Computation of the flow past a half-cylinder. Temporal eigenfunctions $\psi_n(t)$ versus $t$ obtained from the low dimensional dynamical system. Bottom: solid line $n = 1$; $- \cdot - \; n = 2$; $- \cdot\cdot - \; n = 3$. Top: solid line $n = 4$; $- \cdot - \; n = 5$.

the same frequency as before, it decays in the long time behavior. It is interesting to mention that this artifact disappears if we impose $\psi_1(t) = constant$, which amounts to decomposing only the fluctuation (around the temporal mean) and maintaining the mean flow constant in time. This procedure was indeed applied by Deane et al. (1990) for a similar system. We show our stable limit cycle recovered in this manner in Figure 3.19. Physically, the influence of the pressure term $c_j(t)$ through the outer boundaries of a finite computational domain supplies the dynamical system with an external forcing which stabilizes the limit cycle. Without this forcing, the solution escapes slowly from the right orbit as time increases. Meanwhile, imposing $\psi_1(t) = constant$ introduces an external forcing, which counteracts the damping in a similar manner as the action of the pressure from the outer boundary.

## 3.7 Conclusions

The biorthogonal decomposition method was applied for the analysis of laminar wake flows. The symmetries of the Karman street have been studied through the notion of spatio-temporal symmetry. In particular, the non-instantaneous deterministic reflection symmetry provides an interesting example illustrating the power of the isomorphism between space and time intrinsic to the BOD. The breaking of such space-time symmetry occurs as Reynolds number increases, which may give an interesting insight into our understanding of the route to turbulence. There, however, the reflection symmetry is still satisfied in a statistical sense, which gives us some information on the spatial structure of the flow in terms of sinuous and varicose modes.

A hierarchy of modes, based on dilation symmetries, arises naturally in fully developed turbulence, in the inertial range of the spectrum, when the flow is assumed to satisfy, in a statistical or deterministic sense, one of the scaling symmetries of Navier-Stokes equations. The presence of these self-similar modes leads to an

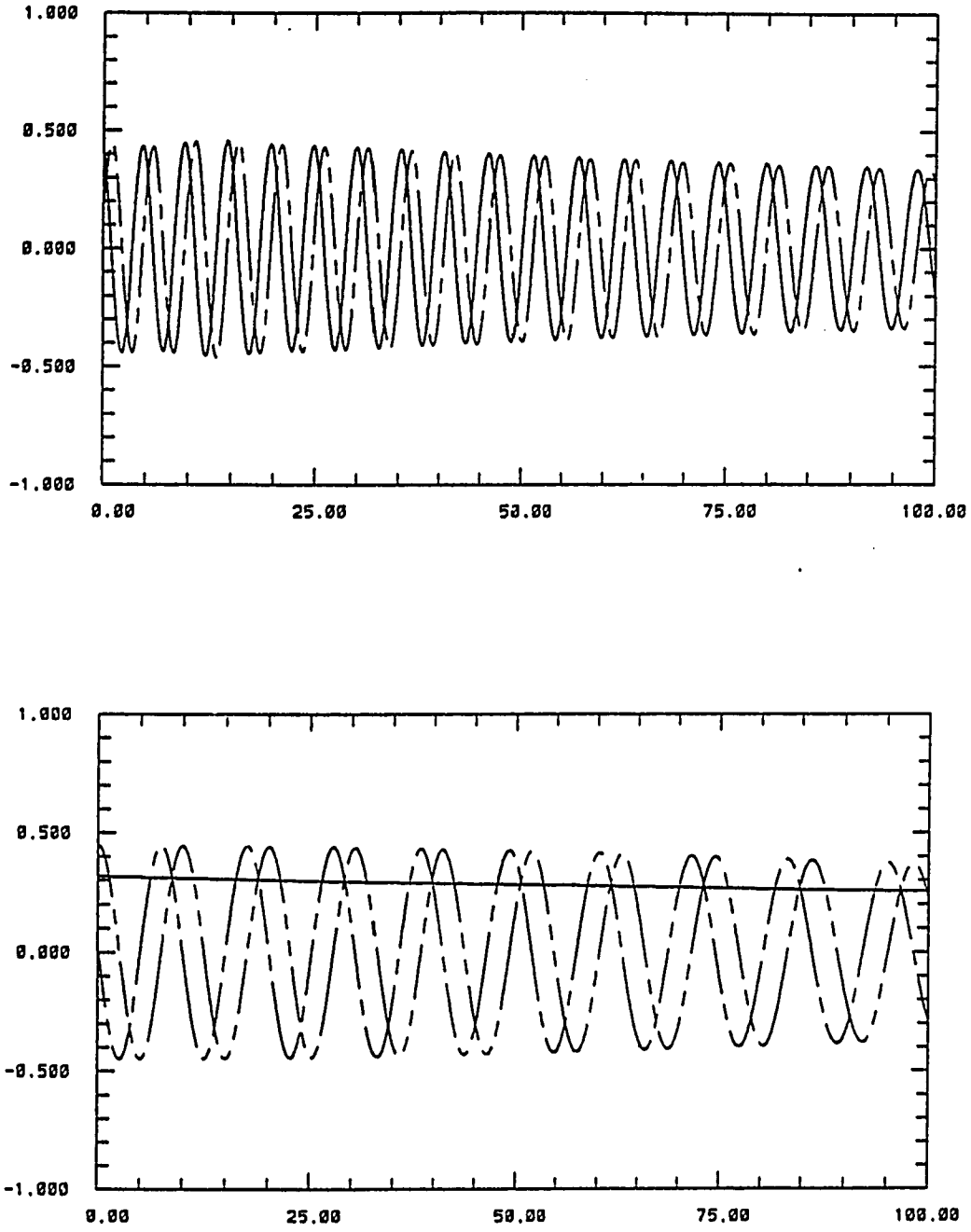


Figure 3.18: Computation of the flow past a half-cylinder. Same as in Figure 3.17, except that the influence of $c_j(t)$ is suppressed.

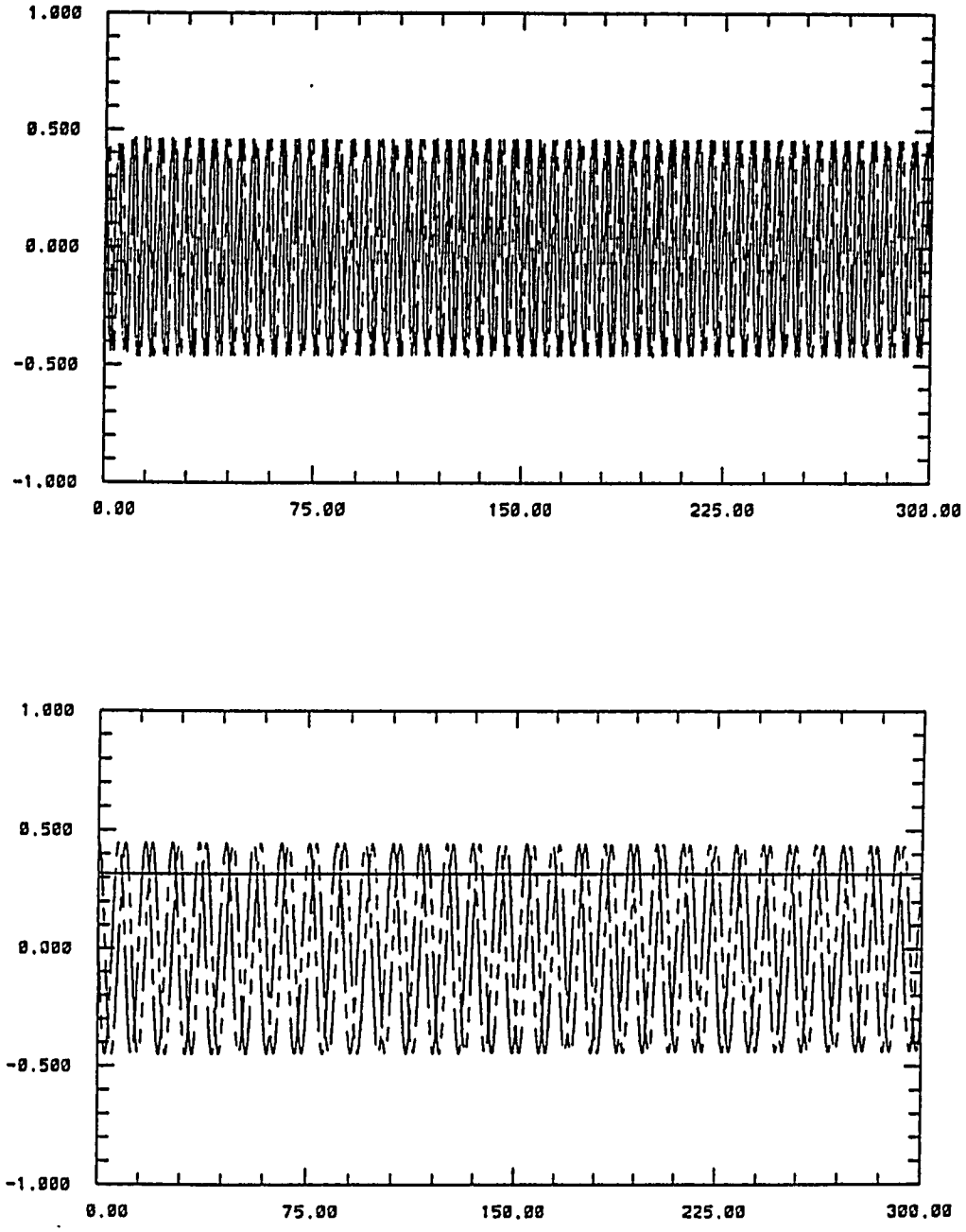


Figure 3.19: Computation of the flow past a half-cylinder. Same as in Figure 3.17, except that a constant first chrono $\psi_1(t) = constant$ is imposed.

exponential decay spectrum law, which indeed seems to emerge from the analysis of experimental data extracted from a turbulent flow behind a cylinder.

A low-dimensional dynamical system was constructed from the Navier-Stokes equations and the BOD expansion extracted from the output of a numerical simulation. On the one hand, the Karman street was successfully reproduced via such system whose dimension is much smaller than that of conventional numerical simulations. On the other hand, the limitation of the method gave us some interesting insight into the physics of the flow and the important dynamical role played by the low energy modes, even of extremely small amplitude.

# Chapter 4

# Turbulent Wake Flow Studied by the Proper Orthogonal Decomposition Method

This chapter is organized as follows. Section 4.1 briefly describes the flow system and the experimental measurement of the correlation matrix. Section 4.2 describes the Proper Orthogonal Decomposition method which we use to analyze the data. The analysis of the energy spectrum and the modes thus obtained in terms of the physical eddies of the flow are presented in Section 4.3. We then use such modes to derive a low dimensional dynamical system and we describe the results in Section 4.4. Finally we draw our conclusions in Section 4.5.

## 4.1 Flow System and Experimental Measurements

We consider the turbulent far-wake behind a circular cylinder of diameter $d$. As previously, $x_1$ denotes the streamwise direction, $x_3$ the spanwise direction and $x_2$ the remaining direction. The computational domain is

$$0 \leq x_1 \leq L_1, \quad -L_2/2 \leq x_2 \leq L_2/2, \quad 0 \leq x_3 \leq L_3.$$

and the axis of the cylinder is located at $x_1 = -X_d$. It is known that in the far-wake it is reasonable to assume that the flow is homogeneous in the streamwise and spanwise directions. Moreover, in this kind of flow, Taylor's hypothesis based on the fact that the mean flow magnitude is much larger than the root mean square of the fluctuation is often used. We, however, keep in mind that it is only exactly satisfied in the case of a traveling wave and, in all other cases (particularly turbulence), it is only a rough approximation.

Measurements have been recorded at a downstream distance of $100d$ behind the cylinder, in a wind tunnel (Guezennec and Gieseke 1991). The Reynolds number, based on the diameter of the cylinder and the free-stream velocity, is Re = 5000. Two probes (one fixed and one moving) scanned a two-dimensional grid consisting of 17 points in the $x_2$-direction and 17 points in the $x_3$-direction. Instantaneous measurements of the three velocity components were recorded simultaneously at two different grid positions. The two-point correlations were then computed, based on the assumption that the flow is statistically stationary.

## 4.2 The Proper Orthogonal Decomposition

According to the Proper Orthogonal Decomposition (POD) theorem of probability theory, the two-point correlation of a random signal can be expanded as a series of deterministic functions. We consider an energy integrable function

$$u_\omega(x) \in L^2(X)$$

where $x \in X$ and $\omega$ a random sampling variable of a statistical set $\Omega$. Then the two-point correlation function

$$R(x,x') =< u_\omega(x)u_\omega(x') >_\omega$$

(where $< >_\omega$ denotes the ensemble average over the statistical variable $\omega$) can be expanded into

$$R(x,x') = \sum_{k=1}^{\infty} \lambda^{(k)}\phi^{(k)}(x)\phi^{(k)*}(x')$$

where superscript $*$ indicates the complex conjugate, and the $\lambda^{(k)}$'s and $\phi^{(k)}(x)$'s are the eigenvalues and eigenfunctions of the integral equation

$$\int_x R(x,x')\phi^{(k)}(x')dx' = \lambda^{(k)}\phi^{(k)}(x).$$

Then the random signal $u_\omega(x)$ can be decomposed into orthogonal deterministic basis functions $\phi^{(k)}(x)$, so called POD modes, and random coefficients $a_\omega^{(k)}$ in the following way

$$u_\omega(x) = \sum_{k=1}^{\infty} a_\omega^{(k)}\phi^{(k)}(x)$$

where $< >_\omega$ denotes the ensemble average over the statistical sampling variable $\omega$. Note that the random coefficients $a_\omega^{(k)}$ are not determined by the decomposition, hence the criticism (as recalled in our introduction) that the POD omits the phase information.

An important property of the POD is that the deterministic mode or "structure" $\phi^{(k)}(x)$ is selected in such a way that the projection of the signal onto the

structure

$$(\phi, u)/(\phi, \phi)^{\frac{1}{2}}$$

is maximized, where the brackets denote the $L^2$-inner product. We reiterate the maximization process so that the expansion converges optimally fast in quadratic mean.

The POD theorem (Loeve 1955) was first stated for a scalar function $u_\omega(x)$, it has been generalized by Lumley (1967) for vectorial functions of multiple variables for its application to the three-dimensional velocity field of turbulent flows. Under the assumption of statistical stationarity, often made in turbulence, the ensemble average can be replaced by a temporal average. Therefore, the correlations are usually experimentally obtained by the simultaneous measurement of the velocity at two points only and the average computed over a time domain containing several integral time scales so that the flow can be assumed to be statistically stationary. Hence, in the case of a turbulent wake flow, the components of the two-point correlation tensor **R** are defined as

$$R_{ij}(x_1 - x_1', x_2, x_2', x_3 - x_3') = \overline{u_i(x_1, x_2, x_3, t) u_j(x_1', x_2', x_3', t)} \tag{4.1}$$

where the overbar denotes the temporal average in the sense previously recalled. In (4.1) $R_{ij}$ depends on $x_1 - x_1'$ and $x_3 - x_3'$ only, as we assume the flow to be homogeneous in these two directions. In this case, the POD modes factorize into Fourier modes in $x_1, x_3$ and eigenfunctions of $x_2$ (Lumley, 1967). Therefore the velocity field can be expanded as

$$\mathbf{u}(x_1, x_2, x_3, t) = \sum_{l,k,n} \sqrt{\lambda^{(lkn)}} a^{(lkn)}(t) \phi^{(lkn)}(x_2) \exp i(l x_1 + k x_3) \tag{4.2}$$

in which $l$ and $k$ are the Fourier wavenumbers in the $x_1$- and $x_3$- directions, $n$ being the POD index. $\lambda^{(lkn)}$ and $\phi^{(lkn)}$ are the eigenvalues and the eigenfunctions of the following equation

$$\int_{-\infty}^{+\infty} \mathbf{\Phi}^{(lk)}(x_2, x_2') \cdot \phi^{(lkn)}(x_2') dx_2' = \lambda^{(lkn)} \phi^{(lkn)}(x_2) \tag{4.3}$$

where $\Phi^{(lk)}(x_2, x_2')$ is the Fourier transform of the correlation tensor $\mathbf{R}$ in the $x_1$- and $x_3$-directions. Due to the argument used for the biorthogonal decomposition (see Section 3.2.2), it is easy to show that the first and third components of the eigenfunction $\phi^{(lkn)}(x_2)$ are even in $x_2$ and the second component odd, or vice versa as a result of the (statistical) reflection symmetry of the flow in the $x_2$-direction.

## 4.3 Energy Spectrum and Large Eddy Structure

By solving numerically the discretized form of the eigenvalue problem (4.3) for each wavenumber pair, we obtain the eigenvalue $\lambda^{(lkn)}$ and the eigenfunctions $\phi^{(lkn)}$. Figure 4.1 shows the convergence of the accumulated energy $e_n$ including all Fourier modes and only the first $n$ POD modes

$$e_n = \sum_{l,k} \sum_{m=1}^{n} \lambda^{(lkm)}.$$

Figure 4.2 plots the convergence of the reconstructed Reynolds stresses as the number of POD modes $n$ increases. We find that the convergence is reasonably good, although much slower than that of the near-wall region of a turbulent boundary layer (Aubry et al. 1988). Quantitatively, the summation over all Fourier modes and fifteen POD modes captures about 90% of the total energy of the flow.

We now concentrate on the large eddy structures revealed by the POD method. Lumley (1967) suggested that the first POD mode should represent the large eddies of the flow. Due to the fact that Fourier modes are not localized in space and therefore cannot represent coherent structures, Payne and Lumley (1967) suggested to look at the first POD mode by summing over all Fourier modes. Since the phase cannot be recovered from the POD only (see our previous remark), this can be achieved only by a phase assumption consisting of setting all the phases to be equal to 1. Since the time dependent coefficients should be uncorrelated, we know that this is wrong for more than one coefficient. In order to avoid this difficulty, we consider

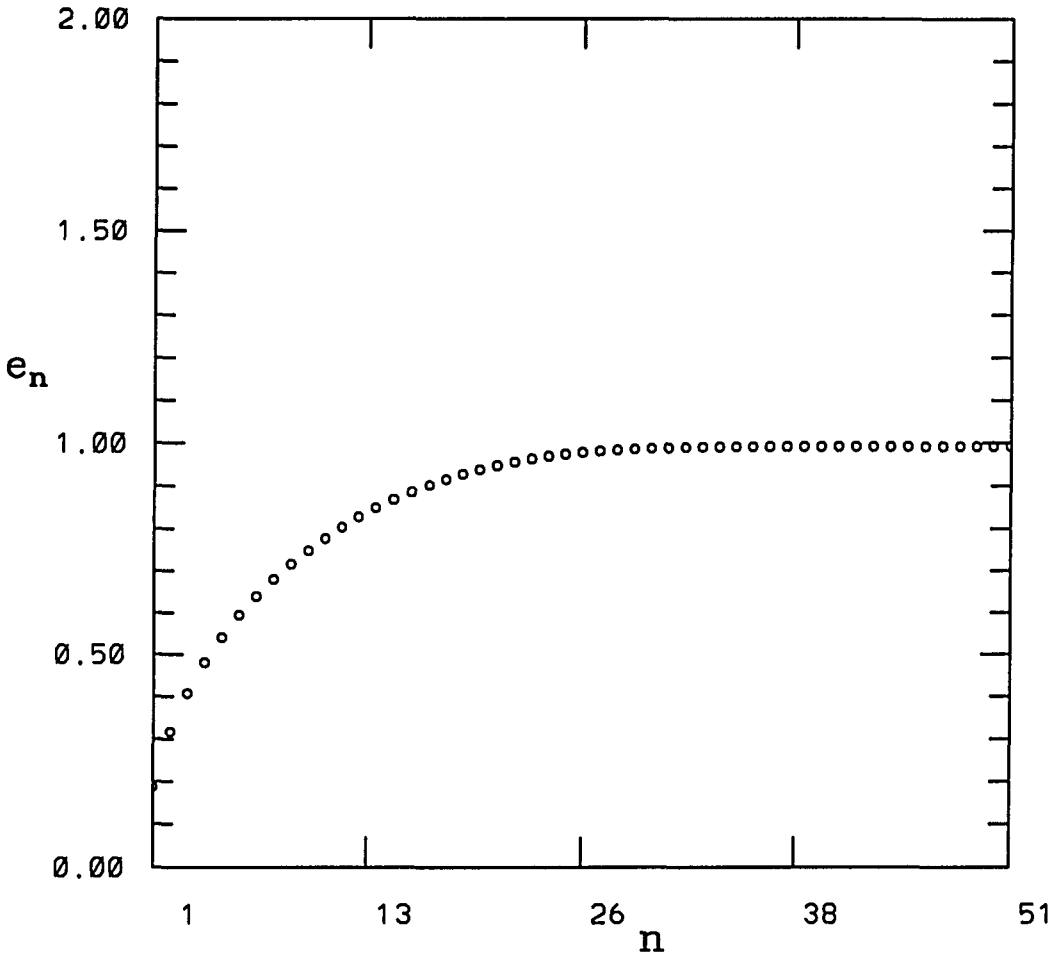


Figure 4.1: POD analysis of experimental data of a far-wake turbulent flow. The cumulated energy percentage $e_n$ as a function of POD index $n$ after summation over all Fourier modes

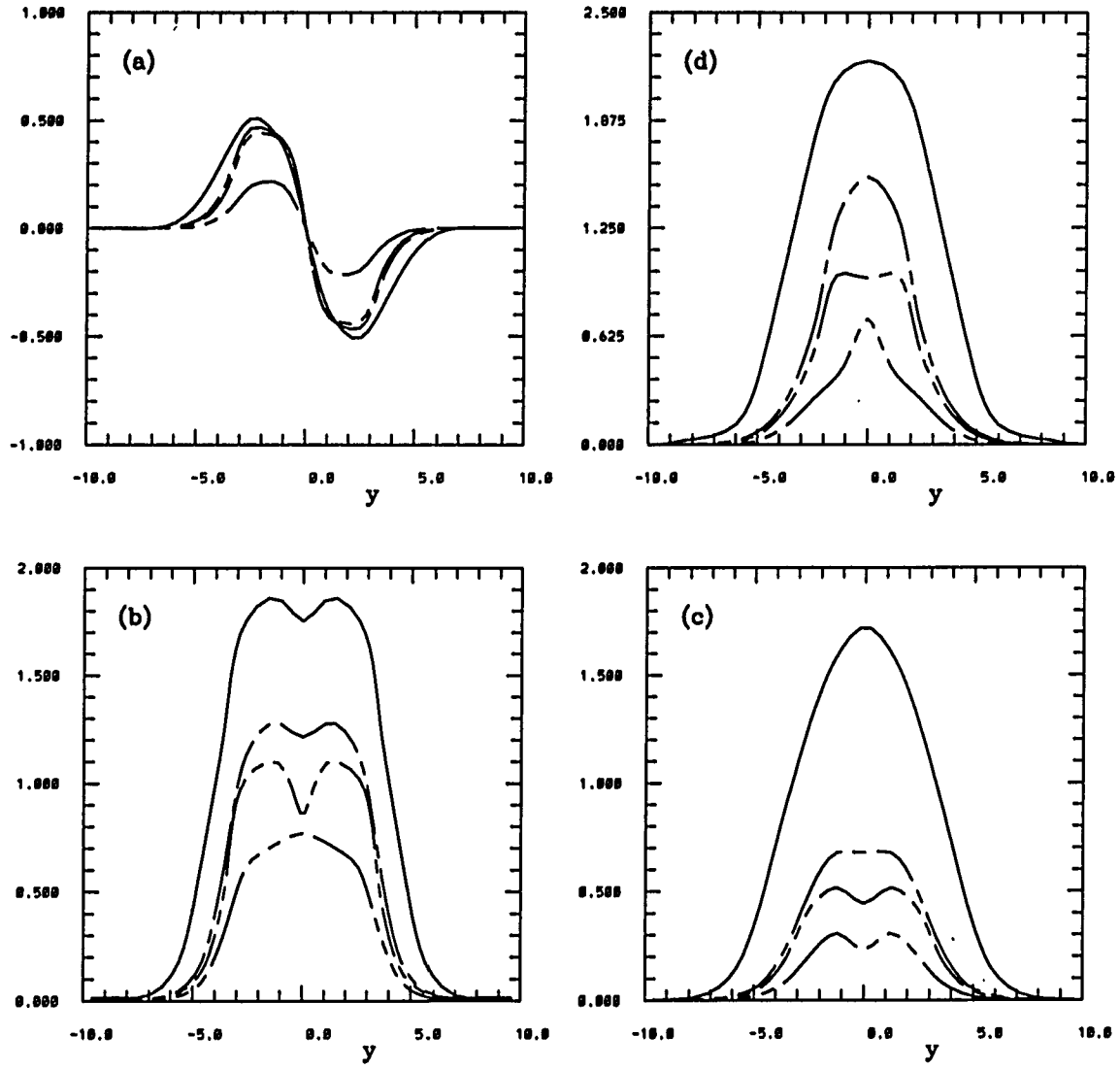


Figure 4.2: POD analysis of experimental data of a far-wake turbulent flow. Reynolds stresses as functions of normal distance $x_2$ (for zero separation) reconstructed from the POD truncated expansion into the first $N$ POD modes (including all Fourier modes). Solid line: with all POD modes; $- \cdot - :\ N = 3$; $- \cdot\cdot - :\ N = 2$; $- \cdot\cdot\cdot - :\ N = 1$. (a) $R_{12}$; (b) $R_{11}$; (c) $R_{22}$ ; (d) $R_{33}$.

a set of four basis eigenfunctions $(l,k,n)$, $(l,-k,n)$, $(-l,-k,n)$, $(-l,-k,n)$ (where $l$ and $k$ are positive) individually. The reconstructed function is necessarily real in physical space and the phases are determined by assuming the reflection symmetry in the $x_3$-direction. Figures 4.3 - 4.6 display certain streamline patterns of modes (1,1,1), (1,1,2), (1,0,1) and (1,0,3).

It is interesting to note that modes (1,1,1) and (1,1,2) represent the typical double-roller structure, as described in our introduction, oriented as follows

$$\begin{cases} u_1 u_2 < 0 & when \quad y > 0 \\ u_1 u_2 > 0 & when \quad y < 0. \end{cases}$$

This orientation is very important since it is responsible for a positive turbulence production which maintains such structures alive.

Grant (1958) suggesting the presence of double-roller structures from the observation of the two-point correlations presented a pair of counter-rotating vortices separated in the $x_3$-direction with their axes in the $(x_1,x_2)$ plane at an angle of $sgn(x_2)\times 45^o$ to the $x_1$-axis. Their plane of fluid circulation is parallel to the $(x_1,x_3)$ plane, preventing any $u_2$ component of the velocity to be alive (see Figure 1.2). Due to the fact that the contribution of such structures to the Reynolds shear stress is zero, they cannot sustain themselves. Consequently, Grant suggested that these double-roller eddies, present in the far-wake, had been initially formed in the neighborhood of the cylinder and should be decaying in time. Obviously, this conclusion needs to be supported by an experimental observation of similar structures in the near- wake of the cylinder, for which, in our knowledge, there is no evidence. Payne and Lumley (1967), analyzing Grant's data, conceptually suggested the presence of a double-roller structure from their POD modes, as we recalled in our introduction. They found that the flow circulations of the rollers are inclined to the $(x_1,x_3)$ plane such that they are approximately normal to the $sgn(x_2)\times 45^o$ direction to the $x_1$-axis. The configuration of such a vortex structure supplies a negative turbulence production to the flow and

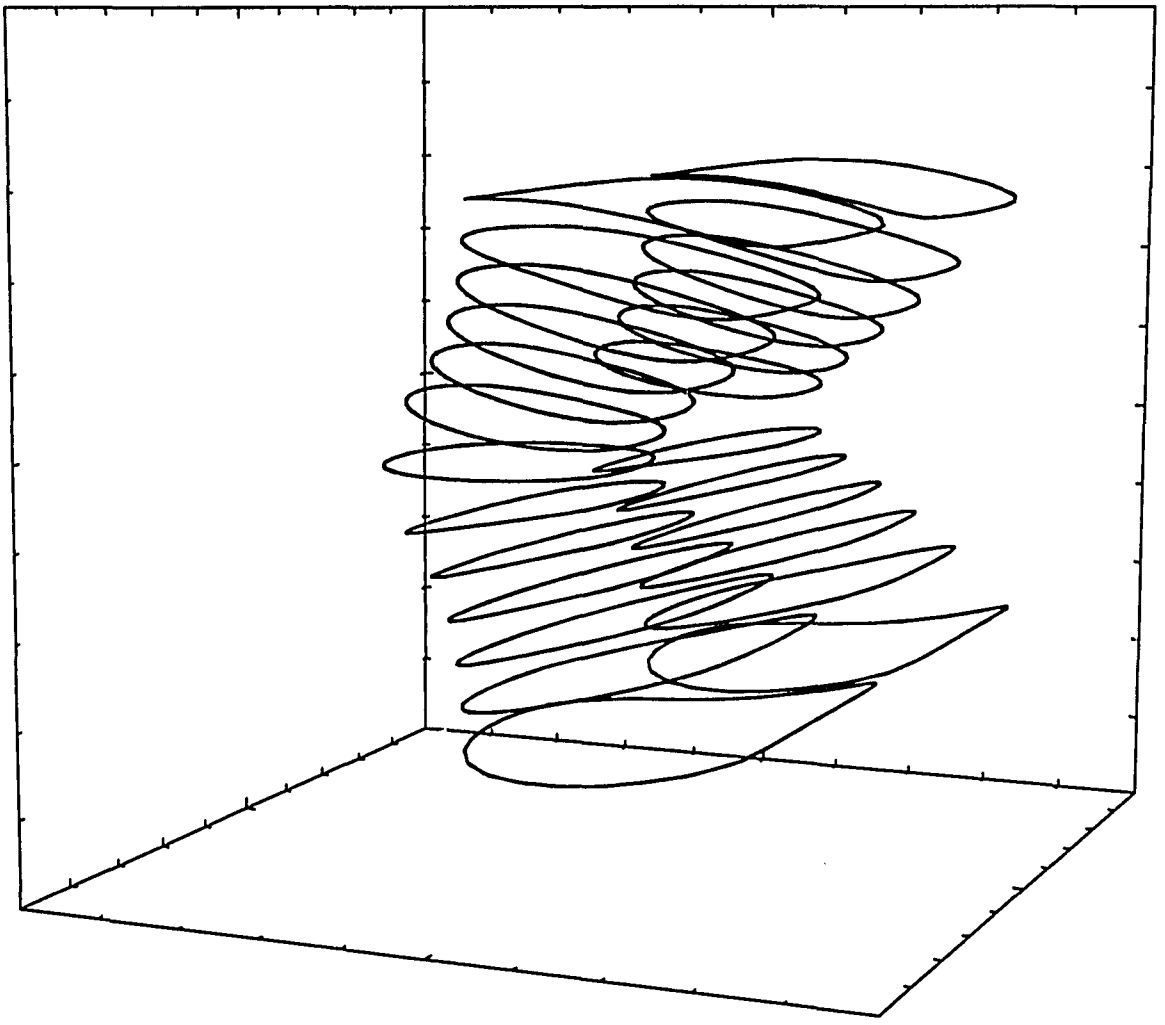

Figure 4.3: POD analysis of experimental data of a far-wake turbulent flow. Streamline pattern of mode (1,1,1).

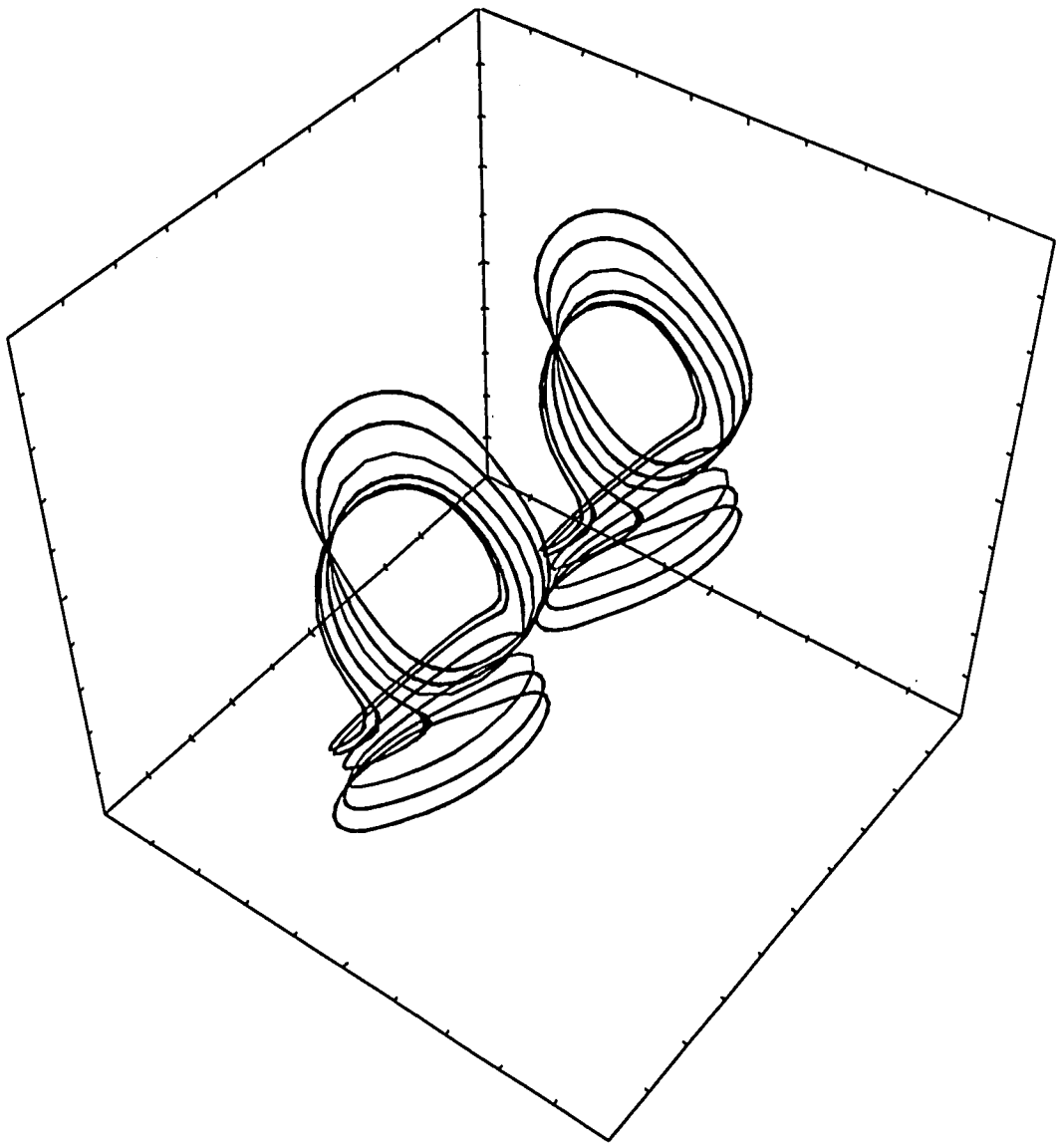

Figure 4.4: POD analysis of experimental data of a far-wake turbulent flow. Streamline pattern of mode (1,1,2).

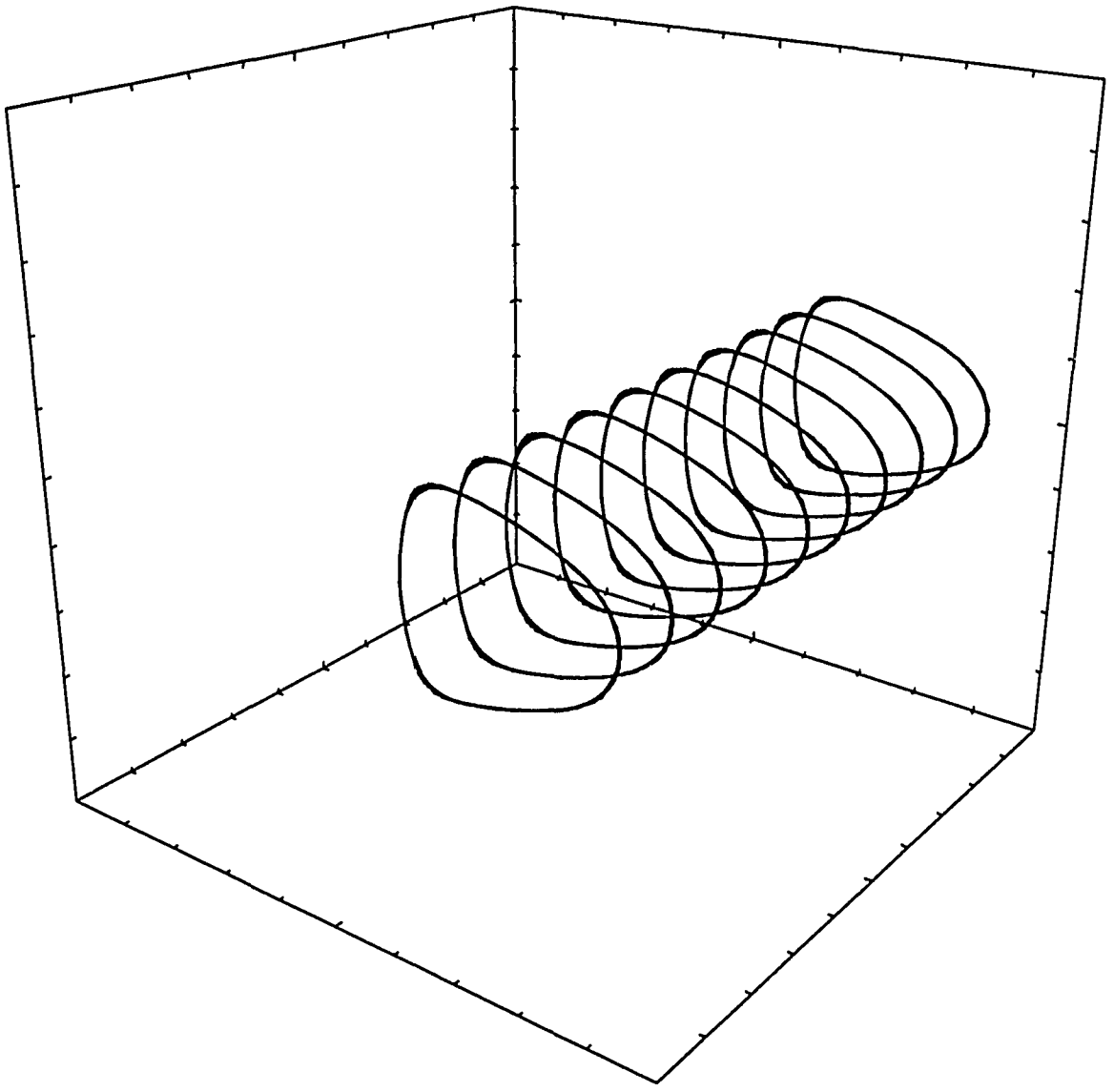

Figure 4.5: POD analysis of experimental data of a far-wake turbulent flow. Streamline pattern of mode (1,0,1).

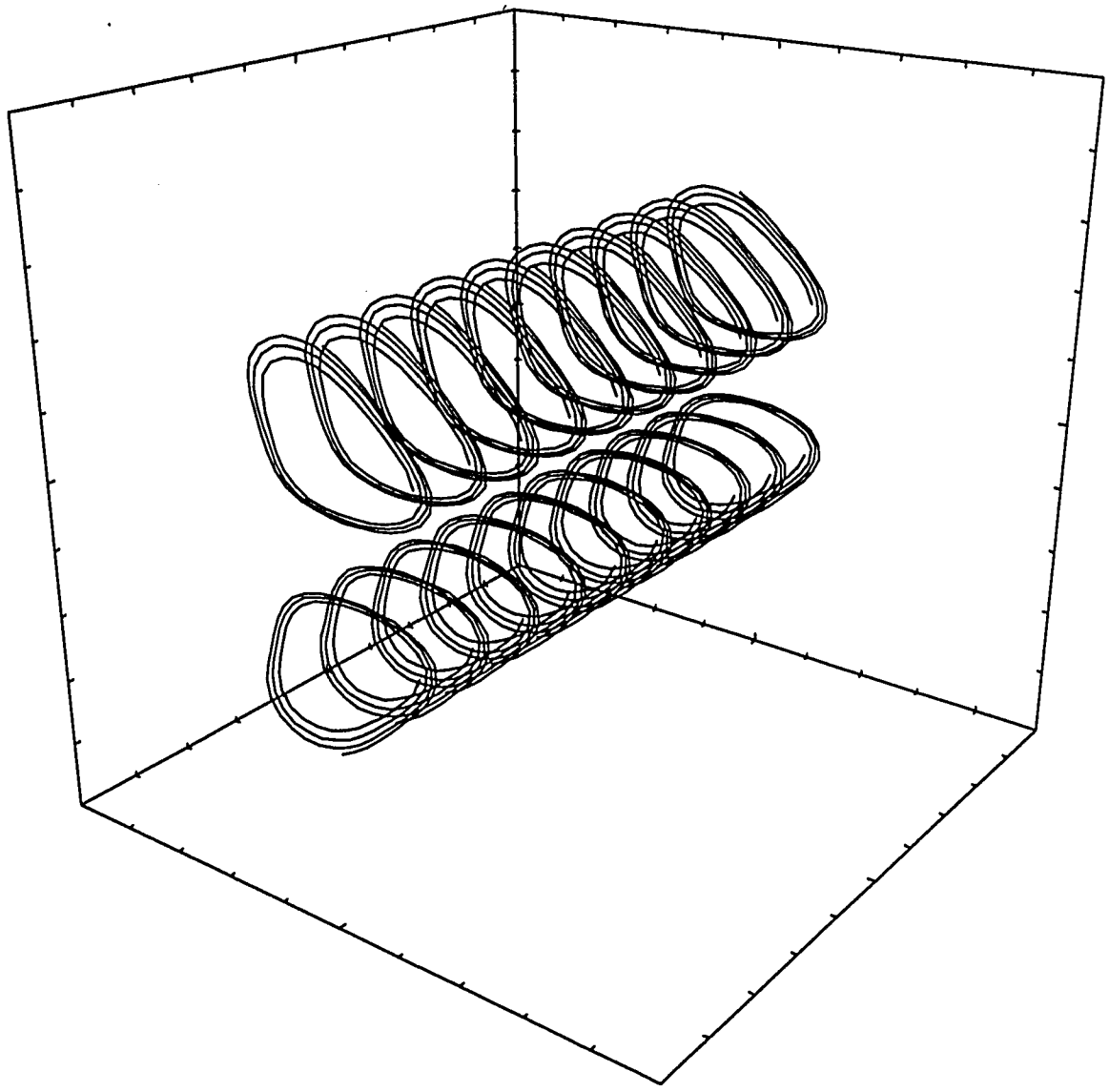

Figure 4.6: POD analysis of experimental data of a far-wake turbulent flow. Streamline pattern of mode (1,0,3).

therefore should decay too.

Based on our findings (Figure 4.3), the double-roller structure has the following properties:

1. It is a pair of counter-rotating vortices displaced in the $x_3$-direction.

2. The axes of the vortices are curved lines normal to the $(x_1, x_3)$ plane at $x_2 = 0$ and oriented approximately at an angle $sgn(x_2) \times 45^o$ to the $x_1$-axis at the outer ends.

3. The fluid circulates in a plane whose normal direction coincides with the roller axes.

Due to the difficulty to perform three-dimensional experiments, it is nowadays impossible to obtain a complete data base adapted to an appropriate identification of coherent structures in turbulent flows. The double-roller structure extracted here through the POD method leads to a reasonable mechanism which maintains turbulence in the flow. However, there is no guarantee that the symmetric structure exists instantaneously in the flow. A more complete set of data would be desirable to extract spatio-temporal patterns in a manner described in Chapter 3. Moreover, comparison with other coherent structure methods may give us insights for a deeper understanding.

Modes (1,0,1) and (1,0,3) correspond to spanwise vortices, referred to as "mixing jets" by Grant (1958). This demonstrates the capability of the POD procedure to capture this large eddy motion of entrainment in wake flows as well. It also shows the advantage of considering different modes individually without taking the average over Fourier modes. Payne and Lumley (1967) could extract the double-roller structure only. This was due to their averaging procedure over Fourier modes used in accordance with their definition of large eddy structures and their phase assumption (see our earlier discussion).

## 4.4 Low-dimensional Dynamical System

In this section, we present a low dimensional dynamical system based on the POD method. The velocity can be decomposed into the mean flow velocity **U** and the fluctuation $u$, and the pressure into the mean flow pressure $P$ and the fluctuation $p$. Substituting this Reynolds decomposition into the Navier-Stokes equations, we can derive governing equations for both the mean quantities and the fluctuations.

### 4.4.1 Mean Velocity Model

Aubry et al. (1988) derived a low dimensional dynamical system from the POD expansion of the velocity fluctuation. The equations thus found are those governing the fluctuation, which interacts with the mean flow. The expression of the latter in terms of the fluctuation was based on a parallel flow approximation. In spite of the similarities between a turbulent far-wake and a turbulent boundary layer, we find that an a priori parallel mean flow assumption is not appropriate for wake flows. Instead, we use the similarity solution in which we neglect streamwise variations of the mean velocity. (It is worth pointing out that such an expression for the mean field cannot be recovered by an a priori parallel flow assumption.)

The far wake flow is extremely elongated in the $x_1$-direction, so that the characteristic length scale in the normal direction is typically much smaller than those in the streamwise and spanwise directions. As a result, the famous boundary layer approximation can be used. This leads to governing equations for the mean flow in the following form (Hinze, 1970)

$$U_\infty \frac{\partial U_1}{\partial x_1} = \frac{\partial}{\partial x_2} \overline{u_1 u_2} \tag{4.4}$$

$$\frac{\partial U_1}{\partial x_1} + \frac{\partial U_2}{\partial x_2} = 0 \tag{4.5}$$

for which a similarity solution exists. The relation between the mean velocity and

the Reynolds shear stress can hereby be written as follows

$$\frac{U_1}{U_\infty} = 1 + \frac{2(x_1 + X_d + a)}{x_2} \frac{\overline{u_1 u_2}}{U_\infty^2} \tag{4.6}$$

$$\frac{U_2}{U_\infty} = -\int_0^{x_2} \frac{1}{x_2} \frac{\overline{u_1 u_2}}{U_\infty^2} dx_2 \tag{4.7}$$

where $\mathbf{U} = (U_1, U_2)$ is the mean velocity, $U_\infty$ the velocity of undisturbed incoming flow, $X_d$ the distance between the cylinder and the downstream location of the experimental measurements (see above), $a$ the distance between the virtual origin of the wake (i.e. the origin of similarity) and the center of the cylinder. The constant $a = 111.1d$ can be determined by substituting the mean velocity $U_1$ and the Reynolds stress $\overline{u_1 u_2}$ experimentally measured in (4.6).

The validity of the previous similarity solution has been experimentally confirmed under the condition that

$$\frac{x_1 + X_d + a}{d} > 90$$

which is satisfied in our case.

After obtaining the expression of the mean flow under a similarity assumption, it is now a reasonable approximation to neglect the streamwise variation of the mean flow in the far-wake so that we can write

$$\frac{U_2}{U_\infty - U_1} \sim \frac{y}{2(x_1 + X_d + a)} \ll 1$$

which indeed means that the velocity component in the $x_2$-direction is negligible. Moreover, the length of the finite dimensional domain considered here in the $x_1$-direction is much smaller than the distance from the virtual origin to the domain i.e.

$$\frac{L_1}{x_1 + X_d + a} \ll 1$$

which indicates that the variation of $U_1$ with $x_1$ can be neglected. Consequently,the mean flow expression now becomes

$$\mathbf{U} = U_1(x_2)\mathbf{e}_1 \tag{4.8}$$

where $U_1(x_2)$ is given by (4.6).

### 4.4.2 Derivation of the Sets of ODEs

The equations governing the fluctuations can be written as follows

$$\dot{u}_i + u_{i,1}U_1 + U_{1,2}u_2\delta_{i,1} + u_{i,j}u_j = -p_{,i} + < u_{i,j}u_j > + \frac{1}{Re}u_{i,jj} \tag{4.9}$$

$$u_{i,i} = 0 \tag{4.10}$$

where $< >$ denotes the spatial average

$$< >= \frac{1}{L_1 L_3}\int_0^{L_1}\int_0^{L_3} dx_1 dx_3$$

and the spatial mean velocity is assumed to be identical to that of (4.8). Let $N_i = 0$ denote (4.9), and $(\cdot,\cdot)$ represent the inner product

$$(\mathbf{f},\mathbf{g}) = \int_0^{L_1}\int_{-\frac{L_2}{2}}^{\frac{L_2}{2}}\int_0^{L_3} f_i g_i dx_1 dx_2 dx_3.$$

We now substitute the POD expansion (4.2) into (4.9), and project the obtained equation onto the modes

$$\phi^{(lkn)}(x_2)\exp i(lx_1 + kx_3)$$

by taking the inner product

$$(\phi^{(lkn)}(x_2)\exp i(lx_1 + kx_3), \mathbf{N}) = \mathbf{0}.$$

We then obtain a set of ordinary differential equations in the form

$$\mathbf{I}\frac{d\mathbf{a}}{dt} = \mathbf{B}\mathbf{a} + NL \tag{4.11}$$

where $\mathbf{I}$ is the identity matrix and $\mathbf{B}$ a constant matrix. $NL$ denotes the non-linear terms and $\mathbf{a}$ represents the unknown coefficients of the POD expansion describing the dynamics of the flow. The linear terms originate in the viscous terms of the Navier-Stokes equations while the non-linear terms are of two types, quadratic and cubic.

The quadratic terms represent the non-linear interactions among fluctuations due to the advection terms of the Navier-Stokes equations. The cubic terms originate in the interaction between the mean and the fluctuating velocities. Appendix A presents the detailed form of the equations (4.11).

Finite dimensional dynamical systems can then be derived by simply truncating the previous infinite set of ODEs. The effects of unsolved modes onto the resolved ones need to be included to account for the energy transfer between the resolved and unresolved modes. Recently, numerous studies including dynamical subgrid scale models in large eddy simulations, approximate inertial manifold techniques and renormalization group methods, have concentrated their effort toward this goal. Here, we simply introduce a primitive and classical eddy viscosity model, similar to Smagorinsky's technique, taking the eddy viscosity coefficient under the form

$$\nu_T = \frac{\alpha}{Re_T} U_\infty d$$

where $\alpha$ is a transport coefficient close to unity and

$$Re_T = \frac{(\sum_{l,k,n} \lambda^{(l,k,n)} (\int_{-L_2}^{L_2} |D\phi^{(l,k,n)}(x_2)|^2 dx_2 + l^2 + k^2) L_1 L_2 L_3)^{1/2}}{\sum_{l,k,n} \lambda^{(l,k,n)}} \qquad (4.12)$$

where the triplets (l,k,n) denote the neglected modes. We do not use an alternative, more accurate method, since a rough model should be adequate for our purpose. Indeed, we do not seek to simulate a turbulent wake flow in complete details but, instead, we are interested in recovering qualitatively right dynamics and statistics from a low-dimensional dynamical system. On the one hand, as we discussed before, the convergence of the POD is relatively slow in the turbulent far-wake so that we know a priori that retaining only a few POD modes (namely one or two) will not permit results quantitatively comparable with the real flow data. On the other hand, the inclusion of an eddy viscosity model is necessary to mimic the energy cascade in our truncated system.

We now discuss some general properties of the set of ODEs (4.11). It has

all invariant subspaces possessed by Aubry at al. (1988)'s system, such as k-even subspace, the pure real subspace and the phase invariance subspace. The wake system, however, satisfies an additional symmetry due to the statistical normal reflection symmetry. As shown earlier, this implies that POD eigenfunctions have either even (in $x_2$) first and third components and an odd second component, or odd first and third components and an even second component. It is then easy to check that the $n$-even subspace is also an invariant subspace of the system of equations (4.11). Aubry et al. proved that their system is globally stable owing to the fact that all cubic coefficients are all negative. The latter argument cannot be used here as we find both negative and positive cubic coefficients. Nevertheless, numerical tests show that the solution is always attracted to a bounded region which is globally stable. This leads us to believe that, in a certain average sense, cubic coefficients are negative in the present system also, consistently with the orientation of our 'main' eddies for which the turbulence energy production is positive (see our earlier discussion).

### 4.4.3 Numerical Results and Discussion

Since we concentrate our effort in understanding the structure of the wake in the inhomogeneous direction and in reproducing the flow with a few POD modes, we keep a reasonable number of Fourier modes and a minimum number of POD modes. Moreover, since the convergence is slower in Fourier modes than in POD modes and the spectrum maxima are not at zero wavenumbers, it would be rather tricky to severely truncate the Fourier expansion, an operation which we choose to avoid. We then study a dynamical system retaining 1 POD mode and $17 \times 17$ Fourier modes. This system has a dimension of 290, after we take into account the symmetries of the coefficients $\mathbf{a}^{(lkn)}$.

We then numerically solve our dynamical system with a Runge-Kutta scheme and numerically check all the invariant subspaces. Numerical tests showed that the

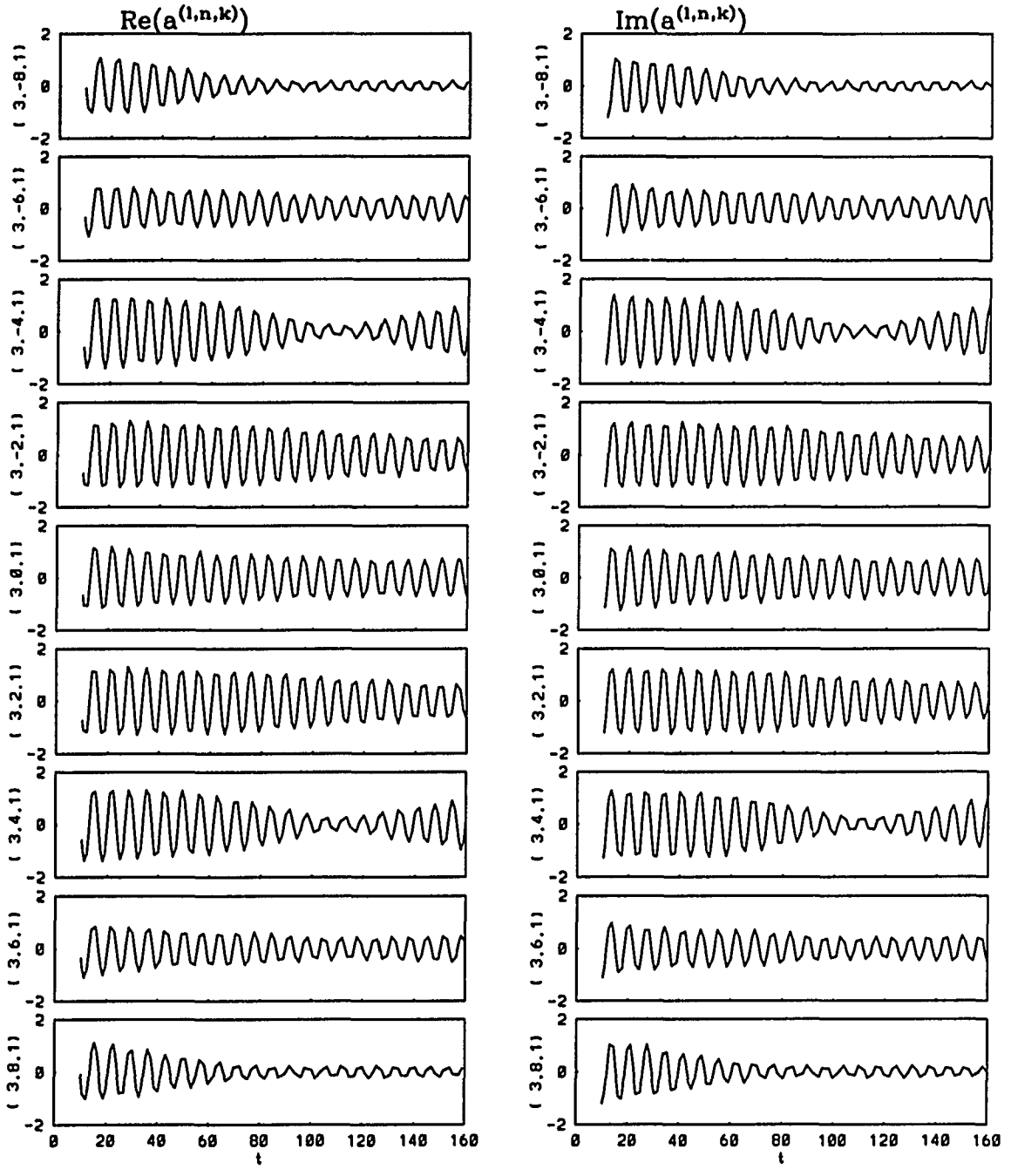


Figure 4.7: Integration of a low dimensional dynamical system simulating a turbulent far-wake. Time series of selected time dependent coefficients $a^{(lkn)}(t)$, with specific values of $(l, k, n)$ appearing on the left-hand side of each curve.

value of the transport coefficient $\alpha$ does not influence the dynamics in a significant way (beyond the steady regime corresponding to large $\alpha$ value). We arbitrarily chose $\alpha = 4$. Figure 4.7 shows the typical time series of the coefficients $a^{(lkn)}$, which are modulated sinusoids. A closer observation of these modes shows that the dynamics consist of traveling waves propagating at a speed approximately equal to the mean velocity. We should, however, refrain from going further into the interpretation of these dynamics exclusively consisting of traveling waves since Taylor's hypothesis has been used for the space-time conversion of the experimental data. Figure 4.8 displays the time history of the norm of vorticity at $x = y = 3.6d$, $z = 0$. In figure 4.9, we present the turbulence statistics, namely the Reynolds stresses, obtained from the truncated low-dimensional dynamical system and those reconstructed from the POD eigenfunctions and eigenvalues directly. Since the first POD mode contains approximately 20% of the energy, we obviously cannot expect our truncated system to quantitatively mimic the whole flow. Nevertheless, Figure 4.9 shows that our low-dimensional dynamical system is capable of recovering the turbulence statistics originally contained in the retained modes. This is probably due to the self-similarity of the accumulated statistics curves (4.2), perhaps originating in the (dilation) symmetry relating the modes: At any level of the truncation, one sees that statistics are well-represented, so that a truncated dynamical system is capable of reproducing a self-sustained miniature flow, however, 'weaker' (in amplitudes, i.e. low statistics) than the real one. Physically, this means that despite the relatively slow convergence of the expansion, the large eddies have the main ingredients of the full flow.

Figure 4.10 illustrates a perspective view of an iso-surface of the norm of the vorticity resulting from the low-dimensional dynamical system, in which we can see the spanwise, normal and streamwise vorticity structures. These structures are traveling downstream under the strong mean flow advection.

Some dynamical properties of the large eddies of a turbulent wake have been

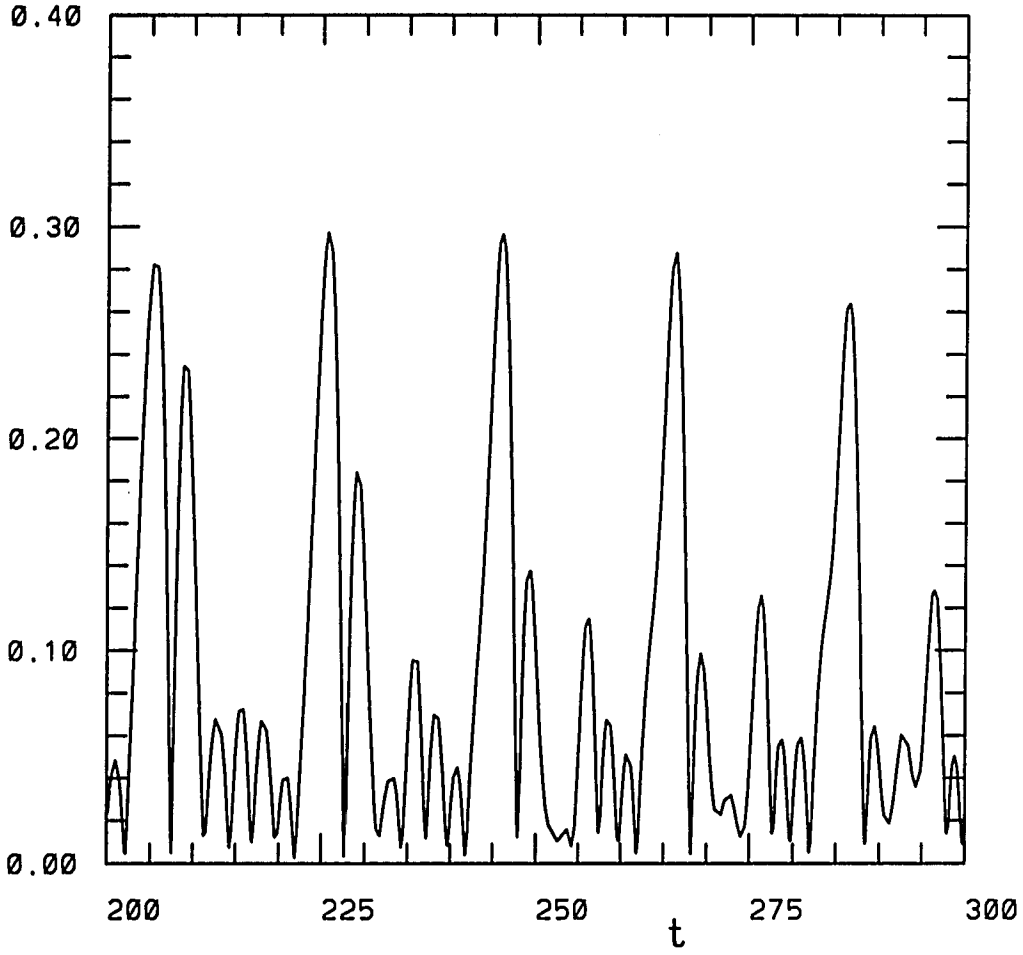


Figure 4.8: Integration of a low dimensional dynamical system simulating a turbulent far-wake. Time series of the norm of the vorticity at the location $x = y = 3.6d$, $z = 0$, where $d$ is the diameter of the cylinder.

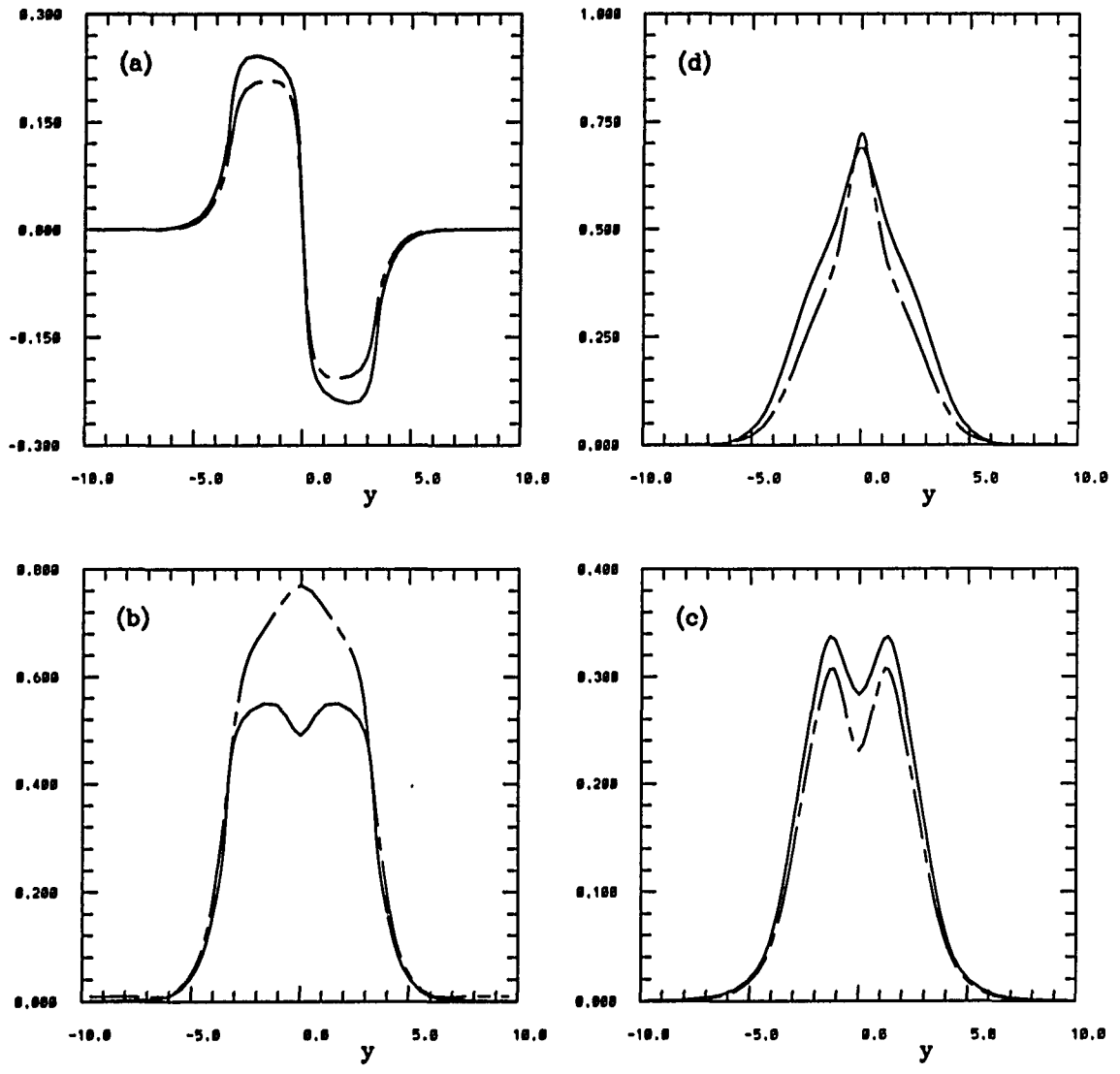


Figure 4.9: Integration of a low dimensional dynamical system simulating a turbulent far-wake. Reynolds stresses as functions of normal distance $x_2$: (a) $R_{12}$; (b) $R_{11}$; (c) $R_{22}$ ; (d) $R_{33}$. The solid line and dash line represent respectively those computed from the low-dimensional dynamical system and those reconstructed directly from the POD eigenfunctions and eigenvalues with the same truncation of modes.

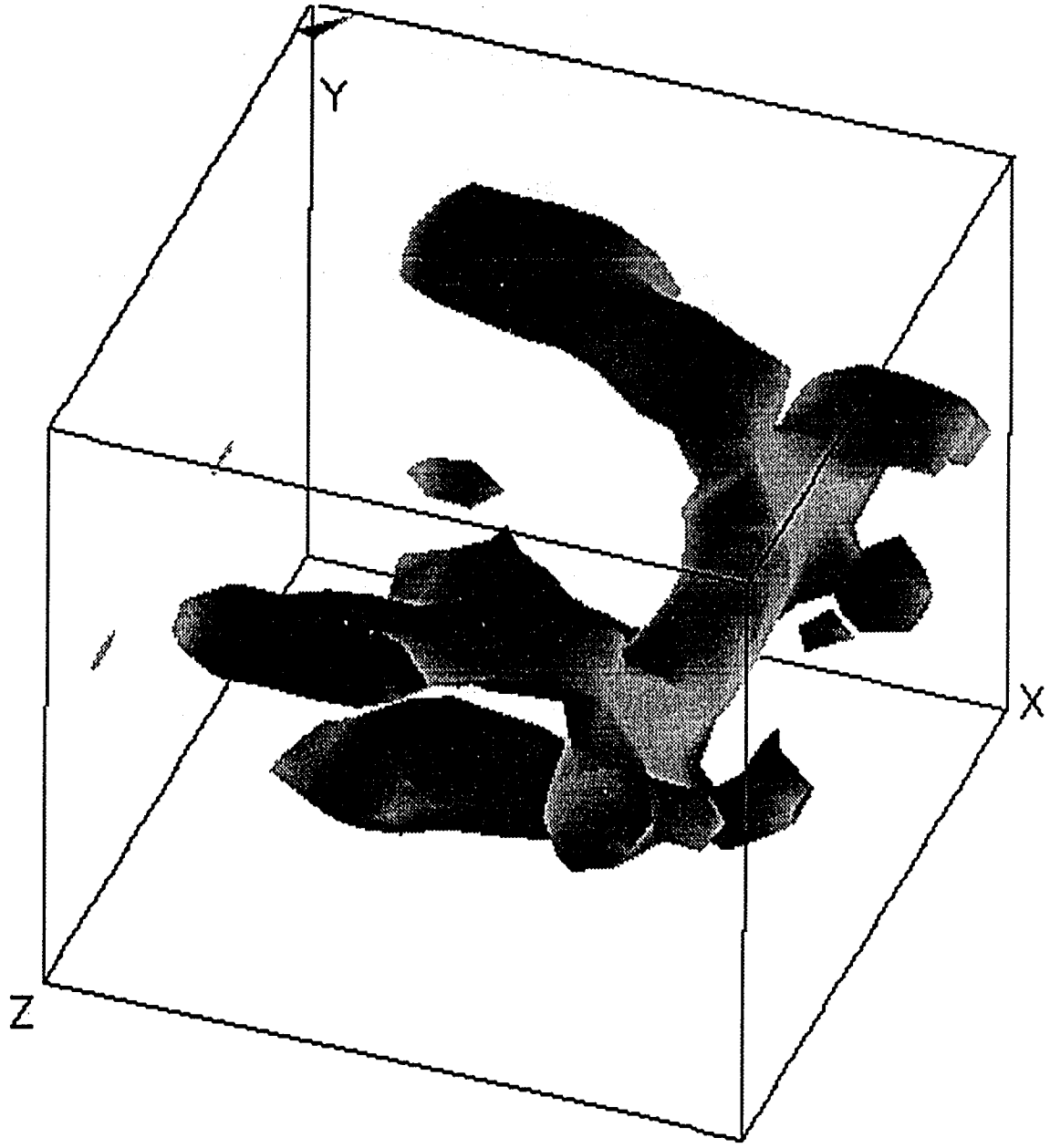


Figure 4.10: Integration of a low dimensional dynamical system simulating a turbulent far-wake. Three-dimensional representation of an iso-surface of the norm of the vorticity.

experimentally observed. For instance, Townsend (1979) found that the spanwise vortices tend to appear in groups, each group containing three to five vortices, their period of appearance within each group being in the range of $8ms$ to $14ms$, or, in non-dimensional variables, 10.1 to 17.7. An observation of Figure 4.8 reveals that the time period of the large eddy structure from our low-dimensional dynamical system is about 20 non-dimensional units, which is in reasonable agreement with Townsend's experimental findings.

## 4.5 Conclusions

The motivation of this work was to study the large eddy structures in a turbulent flow behind a bluff body. The results presented above concern the far wake ($X_d/d = 100$). The application of the POD method has allowed us to extract large eddy structures according to the energy maximization principle. The results show that the large eddies indeed share many characteristics with those visualized in experiments. Particularly, we recover the celebrated double-roller structure which qualitatively resembles that described by other authors. However, the detailed structure differs significantly, which seems to solve the existing paradox that such an eddy should not be able to survive. The orientation of our structure, on the contrary, gives a positive turbulence production, allowing the mean strain to stretch it. Moreover, the decay law of the energy spectrum indicates the presence of a space-time symmetry which should have important consequences for our understanding of the flow structure and our capability of simulating it. This may also be at the origin of the success achieved by a (relatively) low dimensional dynamical system accounting for one POD mode only. Finally, we would like to mention that, compared with other methods used to identify large eddy structures, the POD technique is objective, it is based on solid mathematical and physical grounds and it retains some important symmetries of the original signal.

# Chapter 5

# Summary and Discussion

We have proposed a reduced numerical simulation for laminar wake flows behind circular cylinders, based on the statistical steadiness of the flow (more specifically the spatial mean is time independent) and a Fourier spectral expansion which satisfies all boundary conditions. The central point of this work was to replace the influence of the cylinder by a stationary mean flow driving. Numerical results show that such a system successfully simulates the primary and secondary instabilities of the laminar wake. We should mention that it is reasonable to apply the same method in the direct numerical simulation of turbulent wake flows, for which the statistical steadiness assumption is still justified. In fact, the low dynamical system based on the same assumption and an adapted spectral expansion (Cao and Aubry 1992, see also Chapter 4) successfully reproduced adequate turbulence statistics. Both results are encouraging, indicating that it will be possible to carry out the direct numerical simulation of a turbulent wake flow based on this method while it has not been achieved via other techniques, due to the high computational effort required.

The spatio-temporal analysis of wake flows has been carried out via biorthogonal decomposition methods which define an isomorphism between space and time. We have particularly focussed our attention on space-time symmetry breaking and

generating as Reynolds number increases. A universal feature is that, although a given space-time symmetry breaks, the corresponding (spatial) statistical symmetry, due to the geometry of the flow, remains. For example, the non-instantaneous deterministic reflection symmetry in space obtained after a time shift by a half period in a laminar wake flow provides an example of a well-defined space-time symmetry which we have studied in detail in this thesis. As the Reynolds number increases, this spatio-temporal symmetry breaks due to a change in the temporal component of the symmetry, the spatial one remaining the same. The robustness of the latter is simply due to the fact that it depends strongly on the boundary conditions. This results in a robust (spatial) statistical symmetry, namely the invariance of the two-point correlation tensor by reflection with respect to the wake mid-plane, which persists at all Reynolds numbers, including those at which fully developed turbulence occurs. The result of our analysis shows that the spatial structure of the flow consists of a set of sinuous and varicose modes due to such statistical symmetry. This approach seems promising for a better understanding of the mechanisms governing the routes to turbulence, the spatio-temporal structure of the flow and its bifurcations as Reynolds number increases. The investigation of a turbulent wake flow where the energy spectrum was found to decay exponentially fast suggests the existence of another spatio-temporal symmetry, of the dilation type, which defines a hierarchy among the varicose modes on the one hand and the sinuous modes on the other hand (namely, all varicose (resp. sinuous) modes can be deduced from one mode only by dilation symmetry). Then, we derived a low-dimensional dynamical system for the half cylinder wake flow which reproduces the Karman street and we studied the dynamical importance of small scale structures and that of the pressure term coming from the outer boundaries which were neglected in previous works (e.g. Deane et al., 1991).

The spatial large-scale structures were studied by the proper orthogonal

decomposition method for the turbulent far-wake flow. We were then able to detect large eddies such as the double-roller structure and the spanwise "mixing jet", whose detailed description seems physically reasonable. In particular, the analysis of the structure of the double-roller thus extracted shows that the latter is self-sustained, contrarily to previous claims (Grant, 1958, Payne and Lumley, 1967).

The idea of studying fluid dynamics problems via reduced systems is important and promising for reproducing complex physical phenomena. It is also essential to propose and implement novel theories for understanding the spatio-temporal structure of such phenomena. In this thesis, we have analyzed wake flows in particular, providing in-depth explanations and descriptions of the mechanisms involved. The methods used here, however, can be applied to other fluid flow systems, such as jets or mixing layers, and to other area of physics. Finally, we should mention that, in many cases, the reduced systems lose some information one way or another, compared to the original one. We should thus be careful and restraint ourselves from hasty conclusions regarding these results.

# Appendix A

# Coefficient Matrices $\mathbf{G}_{\pm}$, $\mathbf{G}_{11}$ and $\mathbf{G}_{22}$

The coefficient matrices introduced in (2.24) and (2.25)

$$\mathbf{G}_{\pm} = \{G_{\pm mn}\}$$

$$\mathbf{G}_{11} = \{G_{11mn}\}$$

and

$$\mathbf{G}_{22} = \{G_{22mn}\}$$

can be written as

$$G_{-mn} = \frac{2(1-2n)}{\pi} I_{-}(n,m)$$

$$G_{+mn} = \frac{4n}{\pi} I_{+}(n,m)$$

$$G_{11mn} = -\frac{8n^2}{\pi} I_2(n,m) - \frac{8n}{\pi} I_3(n,m)$$

$$G_{22mn} = -\frac{2(2n-1)^2}{\pi} I_4(n,m) + \frac{4(2n-1)}{\pi} I_5(n,m)$$

where $I_{-}$ and $I_{+}$ are the following integrals

$$I_{-}(n,m) = \frac{1}{4}\int_{-\frac{\pi}{2}}^{\frac{\pi}{2}} \cos^2\eta \cos 2m\eta \cos(2n-1)\eta d\eta$$

$$= \frac{1}{4}\{I_0(m+n) + I_0(n-m) + I_1(1,m+n) + I_1(1,n-m)\}$$

$$I_+(n,m) = \frac{1}{4}\int_{-\frac{\pi}{2}}^{\frac{\pi}{2}} \cos^2\eta \sin 2n\eta \sin(2m-1)\eta d\eta$$
$$= \frac{1}{4}\{-I_0(m+n) + I_0(n-m) - I_1(1,m+n) + I_1(1,n-m)\}$$

All the integrals $I_i$ above can be derived analytically as shown below.

$$I_0(m) = \int_{-\frac{\pi}{2}}^{\frac{\pi}{2}} \cos(2m-1)\eta d\eta$$
$$= \frac{2}{2m-1}(-1)^{m+1}$$

$$I_1(m,n) = \int_{-\frac{\pi}{2}}^{\frac{\pi}{2}} \cos(2n-1)\eta \cos 2m\eta d\eta$$
$$= \frac{1}{2}\{I_0(m+n) + I_0(n-m)\}$$

$$I_2(m,n) = \int_{-\frac{\pi}{2}}^{\frac{\pi}{2}} \cos^4\eta \sin 2m\eta \sin 2n\eta d\eta$$
$$= \frac{\pi}{32}\{6\delta_{m,n+4}\delta_{m,n+1} + 4\delta_{n,m+1} - 4\delta_{m+n,1} + \delta_{m,n+1} + \delta_{n,m+2} - \delta_{m+n,2}\}$$

$$I_3(m,n) = \int_{-\frac{\pi}{2}}^{\frac{\pi}{2}} \cos^3\eta \sin 2n\eta \cos 2m\eta \sin 2n\eta d\eta$$
$$= \frac{\pi}{32}\{2\delta_{m+1,n} - 2\delta_{m,n+1} + \delta_{n,m+2} + \delta_{m+n,2} - \delta_{m,n+2}\}$$

$$I_4(m,n) = \int_{-\frac{\pi}{2}}^{\frac{\pi}{2}} \cos^4\eta \cos(2m-1)\eta \cos(2n-1)d\eta$$
$$= \frac{\pi}{32}\{6\delta_{m,n} + 4\delta_{m,n+1} + 4\delta_{n,m+1} + \delta_{m,n+2} + \delta_{n,m+2}\delta_{m+n,2}\}$$

$$I_5(m,n) = \int_{-\frac{\pi}{2}}^{\frac{\pi}{2}} \cos^3\eta \sin\eta \cos(2n-1)\eta \sin(2m-1)d\eta$$
$$= \frac{\pi}{32}\{2\delta_{m,n+1} - 2\delta_{m+n,2} + \delta_{m,n+2} + \delta_{m+n,3} - \delta_{n,m+2}\}$$

Here, $\delta_{m,n}$ denotes the Kronecker symbol, i.e.

$$\delta_{m,n} = \begin{cases} 1 & \text{if } m = n \\ 0 & \text{if } m \neq m \end{cases}$$

# Appendix B

# The Ordinary Differential Equations of the Dynamical System For Turbulent Wake Flows

The details of the equations (4.11) are given in this Appendix.

$$\frac{da^{(\mathrm{k},n)}}{dt} = \sum_m b_{\mathrm{k}}^{(m,n)} a^{(\mathrm{k},n)} + \sum_{p,q} \sum_{\mathrm{k}'} c_{\mathrm{k},\mathrm{k}'}^{(p,q,n)} a^{(\mathrm{k}',p)} a^{(\mathrm{k}-\mathrm{k}',q)} + \sum_{p,q,r} \sum_{\mathrm{k}'} d_{\mathrm{k},\mathrm{k}'}^{(r,p,q,n)} a^{(\mathrm{k},r)} a^{(\mathrm{k}',p)} a^{(\mathrm{k}',q)}$$

where $b_{\mathrm{k}}^{(m,n)}$, $c_{\mathrm{k},\mathrm{k}'}^{(p,q,n)}$ and $d_{\mathrm{k},\mathrm{k}'}^{(r,p,q,n)}$ are constant coefficients written below.

$$b_{\mathrm{k}}^{(p,q,n)} = [-(ilRe + l^2 + k^2)\delta_{mn} + \int_{-L_2}^{L_2/2} D^2 \phi^{(\mathrm{k},n)} \cdot \phi^{(\mathrm{k},n)^*} dx_2] \frac{1}{Re}$$

$$c_{\mathrm{k},\mathrm{k}'}^{(p,q,n)} = (1 - \delta_{\mathrm{k}0}) \int_{-L_2/2}^{L_2/2} D^2 \phi^{(\mathrm{k}',p)} \cdot \Omega^{(\mathrm{k}-\mathrm{k}')} \phi^{(\mathrm{k}-\mathrm{k}',q)} \cdot \phi^{(\mathrm{k},n)^*} dx_2$$

$$\begin{aligned} d_{\mathrm{k},\mathrm{k}'}^{(r,p,q,n)} = b \int_{-L_2/2}^{L_2/2} \quad & \{-\frac{il}{x_2} \phi^{(\mathrm{k},n)^*} \cdot \phi^{(\mathrm{k},r)} \phi_1^{(\mathrm{k}',p)} \phi_2^{(\mathrm{k}',p)^*} + \\ & \phi_1^{(\mathrm{k},n)^*} \phi_2^{(\mathrm{k},r)} [\frac{1}{x_2^2} \phi_1^{(\mathrm{k}',p)} \phi_2^{(\mathrm{k}',q)^*} - \frac{1}{x_2} (D\phi_1^{(\mathrm{k}',p)} \phi_2^{(\mathrm{k}',q)^*} + \\ & \phi_1^{(\mathrm{k}',p)} D\phi_2^{(\mathrm{k}',q)^*})]\} dx_2 \end{aligned}$$

where $\mathbf{k} = (l, k)$, $D = \frac{d}{dx_2}$, $b = 2(a + X_d)$ is a constant, the star $*$ indicates the complex conjugate, and

$$\Omega_j^{(\mathbf{k})} = \begin{cases} il & \text{if } j = 1 \\ D & \text{if } j = 2 \\ ik & \text{if } j = 3 \end{cases} .$$

# Bibliography


Abernathy, F. H. and Kronauer, R. E. 1962, The formation of vortex streets. *J. Fluid Mech.* **13**, 1.

Arnol'd, V. I. and Meshalkin, L. D. 1960, Seminar A. N. Kolmogorova po izbrannym voprosam analiza (1958-1959) (Seminar led by A. N. Kolmogorov on selected problems of analysis (1958-1959)). *UMN* **15**.

Aubry, N. 1991, On the hidden beauty of the proper orthogonal decomposition. *Theoret. and Comput. Fluid Dyn.* **2**, 339.

Aubry, N. and Cao, N. 1993, Role of the dilation symmetry in turbulence. In Progress in Wavelet Analysis and Applications, eds. Y. Meyer and S. Roques, Editions Frontieres, 43.

Aubry, N., Guyonnet, R. and Lima, R. 1991, Spatio-temporal analysis of complex signals: Theory and applications. *J. Stat. Physics* **64**, 683.

Aubry, N., Guyonnet, R. and Lima, R. 1992(a), Turbulence spectra. *J. Stat. Physics* **67**, 203.

Aubry, N., Guyonnet, R. and Lima, R. 1992(b), Spatio-temporal symmetries and bifurcations via bi-orthogonal decompositions. *Journal of Nonlinear Science* **2**(2), 183.

Aubry, N., Holmes, P., Lumley, J. L. and Stone, E. 1988, The dynamics of coherent structures in the wall region of a turbulent boundary layer. *J. Fluid Mech.* **192**, 115.

Aubry, N. and Lian, W. 1993, Exploiting and detecting space-time symmetries, In "Exploiting symmetries in applied and and numerical analysis", Lectures in Applied Mathematics (AMS), eds. E. Allgower, K. George and R. Miranda (to appear).

Aubry, N., Lian, W. and Titi, E. S. 1993, Preserving Symmetries in the proper orthogonal decomposition, *SIAM J. Sci. Comput.* **14**, 483.

Bakewell, P. and Lumley, J. L. 1967, Viscous sublayer and adjacent wall region in turbulent pipe flow. *Phys. Fluids* **10**, 1880.

Berkooz, G., Holmes, P. and Lumley, J. L. 1993, The proper orthogonal decomposition in the analysis of turbulent flows. Ann. Rev. Fluid Mech. **25**,537.

Bernal, L. P. 1981, The coherent structure of turbulent mixing layers. I.Similarity of the primary vortex structure. II.Secondary streamwise vortex structure. *PhD. thesis*, California Institute of Technology, Pasadena.

Bisset, D. K., Antonia, R. A. and Britz D. 1990, Structure of large-scale vorticity in a turbulent far wake. *J. Fluid Mech.* **218**, 463.

Blackwelder, R. F. and Kaplan, R. E. 1976, On the wall structure of turbulent boundary layer. *J. Fluid Mech.* **76**, 89.

Braza, M., Chassaing, N. N. and Haminh, H. 1986, Numerical study and physical analysis of the pressure and velocity fields in the near wake of a circular cylinder. *J. Fluid Mech.*, **165**, 79.

Breidential, R. 1981, Structure in turbulent mixing layers and wakes using a chemical reaction. *J. Fluid Mech.*, 109, 1.

Brown, G. L. 1992, private communication.

Brown, G. L. and Roshko, A. 1974, On density effects and large structure in turbulent mixing layers. *J. Fluid Mech.* **64**, p. 775.

Cain, A. B. and Ferziger, J. H. 1984, Discrete orthogonal function for non-uniform grids using the fast Fourier transform. *J. Comp. Phys.* **56**, 272.

Campbell, D. and Rose, H. 1983, *Order in Chaos*, North-Holland.

Cantwell, B., Coles, D. 1983, An experimental study of entrainment and transport in the turbulent near wake of a circular cylinder, *J. Fluid Mech.* **136**, 321.

Cao, N. and Aubry, N. 1992, Detection of 'self-similar' structures in turbulence: application to wake flows, in: *Proc. of the IUTAM Symposium: Eddy Structure Identification in Free Turbulent Shear Flows*, Poitiers, France, 12-14 October 1992.

Cao, N. and Aubry, N. 1993, Reduced numerical simulation of wake flow behind a circular cylinder. In *Separated flows*, eds. J.C. Dutton and P. Purtell, FED-Vol. **149** (ASME), 53.

Chen, C-H. P. and Blackwelder, R. F. 1978, Large-scale motion in a turbulent boundary layer: a study using temperature contamination, *J. Fluid Mech.* **89**, 1.

Deane, A., Kevrekidis, I. G., Karniadakis, G. E. and Orszag, S. A. 1991, Low dimensional models for complex geometry flows: application to grooved channels and circular cylinders. *Phys. Fluids A* **3**, 2337.

Eliasen, E., Machenauer, E., and Rasmussen, E. 1970, On a numerical method for integration of the hydrodynamical equations with a spectral representation of the horizontal fields. *Rep. No. 2*, Dep. Meteorol., Copenhagen Univ., Denmark.

Ferré, J. A. and Giralt, F. 1989, Pattern-recognition analysis of the velocity field in plane turbulent wakes. *J. Fluid Mech.* **198**, 27.

Glauser, M., Zheng, X. and George, W. K. 1990, The streamwise evolution of coherent structures in the axisymmetric jet mixing layer. In *The Lumley Symposium: Recent Developments in Turbulence*, Newport News, VA, 11-13, November 1990 (eds. T. Gatski et al.). Springer-Verlag, Berlin.

Gottlieb, D. and Orszag, S. A. 1977, *Numerical Analysis of Spectral Methods: Theory and Applications. CBMS-NSF Reg. Cof. Ser. in Appl. Math.* Vol. **26**. SIAM. Philadelphia, pp. 170.

Grant, H. L. 1958, Large eddies of turbulent motion. *J. Fluid Mech.* **4**, 149.

Gresho, P. M., Chan, R., Upson, C., and Lee, R. 1984, A modified finite element method for solving the time-dependent, incompressible Navier-Stokes equations, Part 2: Applications. *Int. J. Num. Mech. Fluids* **4**, 619.

Guezennec, Y. and Gieseke, T. J. 1991, Multipoint stochastic estimation of the spatio-temporal evolution of the far wake of a circular cylinder. *Bulletin of the American Physical Society* (Program of the forty fourth Annual Meeting of the Division of Fluid Dynamics) **36** (10), 2683.

Guckenheimer, J. 1986, Strange attractors in fluids: another view. *Ann. Rev. Fluid Mech.* **18**, 15.

Hayakawa, M. and Hussain, F. 1989, Three-dimensionality of organized structures in a plane wake. *J. Fluid Mech.* **206**, 375.

Herzog, S. 1986, The large scale structure of in the near-wall region of turbulent pipe flow. Ph.D. thesis, Cornell University.

Hinze, O. J. 1975, *Turbulence*, 2nd Ed., McGraw-Hill,New York.

Karniadakis, G. E., Bullister, E. T. and Patera, A. T. 1985, A spectral element method for solution of two- and three-dimensional time dependent Navier-Stokes equations. In *Proceeding, Europ-US Conference on Finite element Methods for Nonlinear Problems*, Springer-Verlag, Berlin, 803.

Karniadakis, G. E. and Tomboulides, A. G. 1992(a), private communication.

Karniadakis, G. E. and Tomboulides, A. G. 1992(b), private communication.

Karniadakis, G. E. and Triantafyllou, G. S. 1989, Frequency selection and asymptotic states in laminar wakes. *J. Fluid Mech.* **199**, 441.

Karniadakis, G. E. and Triantafyllou, G. S. 1992, Three-dimensional dynamics and transition to turbulence in the wake of bluff objects. *J. Fluid Mech.* **238**, 1.

Keffer, J. F. 1965, The uniform distortion of a turbulent flow. *J. Fluid Mech.* **22**, 136.

Kim, J. and Moin P. 1985, Application of a fractional-ftep method to incompressible Navier-Stokes equations. *J. Comp. Physics* **59**, 308.

Kline, S. J., Reynolds, W. C., Schraub, F. A. and Rundstadler, P. W. 1967, The structure of turbulent boundary layers. *J. Fluid Mech.* **30**, 741.

Kovasznay, L. S. G. 1949, Hot-wire investigation of the wake behind cylinders at low Reynolds numbers. *Proc. R. Soc. A, Lond.*, **198**, 174.

Lian, W. and Aubry, N. 1993, Spatio-temporal structure of compressible turbulence. In *Transitional and turbulent compressible flows.* FED-Vol. **151** (ASME), 129.

Lin, S. J. and Corcos, G. M. 1984, The mixing layer: deterministic models of a turbulent flow. Part 3. The effect of plane strain on the dynamics of streamwise vortices. *J. Fluid Mech.*, **141**, 139.

Loéve, M. 1955, *Probability Theory.* Van Nostrand, New York.

Lorenz, E. N. 1963, Deterministic non-periodic flow. *J. Atmos. Sci.* **20**, 130.

Lumley, J. L., 1965, Atmospheric Turbulence and Radio Wave Propagation. *Proc. Int. Colloq. Moscow.* pp. 166.

Meshalkin, L. D. and Sinai, Ya. G. 1961, *J. Appl. Math.* (PMM). **25**, 1700.

Metcalfe, R. W., Orszag, S. A., Brachet, M. I., Menon, S. and Riley, J. J. 1987, Secondary instability of a temporally growing mixing layer. *J. Fluid Mech.* **184**, 207.

Michalke, A. 1964, On the inviscid instability of the hyperbolic tangent velocity profile. *J. Fluid Mech.* **19**, 543.

Mumford, J. C. 1983, The structure of the large eddies in fully developed turbulent shear flows. Part 2. The plane wake. *J. Fluid Mech.* **137**, 447.

Nicolaenko, B. and She, Z. S. 1990, Symmetry breaking and homoclinic chaos in the Kolmogorov flow. In *Topological Fluid Mechanics*, ed. H. K. Moffatt and A. T. Sinober. Cambridge University Press.

Orszag, S. A. 1969, Numerical methods for the simulation of turbulence. *Physics of Fluids* **12**, 250.

Payne, F. R. and Lumley, J. L. 1967, Large eddy structure of the turbulent wake behind a circular cylinder. *Physics of fluids*, **10**, 194.

Perry, A. E., Chong, M. S., and Lim, T. T. 1982, The vortex shedding process behind two dimensional bluff bodies. *J. Fluid Mech.* **116**, 88.

Rand, D. A. and Young, L. S. (eds) 1981, *Dynamical Systems and turbulence.* Lecture Notes in Mathematics, vol. 898, Springer, Berlin.

Rogallo, R. S. Moin, P. 1984, Numerical simulation for turbulent flows. *Ann. Rev. Fluid Mech.* **16**, 99.

Sanghi, S. and Aubry, N. 1993, Mode interaction models for near wall turbulence. *J. Fluid Mech.* **247**, 455. .

Sirovich, L. 1987, Turbulence and the dynamics of coherent structures. Part I - Part III, *Quarterly of Applied Math.* **XLV** (3), 561.

Slimani, S., Aubry, N., Kolodner, P. and Lima, R. 1992, Biorthogonal decomposition analysis of dispersive chaos in binary fluid convection. *Bifurcation Phenomena and chaos in Thermal Convection*, eds. H.H. Bau, L.Bertram and S.A. Korpela, HTD Vol. **214**, Book No. G00699.

Spalart, P. R., Moser, R. D. and Rogers, M. M. 1991, Spectral Methods for the Navier-Stokes equations with one infinite and two periodic directions. *J. Comput. Phy.* **96**, 297.

Swinney, H. L., and Gollub, J. P. (eds), 1981, *Hydrodynamic Instabilities and the Transitions to Turbulence.* Springer, New York.

Townsend, A. A. 1979, Flow patterns of large eddies in a wake and in a boundary layer. *J. Fluid Mech.* **95**, 515.

Triantafyllou, G. S. and Karniadakis, G. E. 1990, Computational reducibility of unsteady viscous flows. *Phys. Fluids A.* **2**, 653.

Triantafyllou, G. S., Triantafyllou, M. S. and Chryssostomidis, C. 1986, On the formation of vortex streets behind stationary cylinders. *J. Fluid Mech.* **177**, 461.

Williamson, C. H. K. 1988, The existence of two stages in the transition to three-dimensionality of a cylinder wake. *Phys. Fluids* **31**, 3165.